THE UNIVERSITY *of* EDINBURGH

Measurement of Brain Temperature using Magnetic Resonance Spectroscopic Imaging

Jehill Parikh

PhD

The University of Edinburgh

2012

I declare that this thesis has been written by myself, and that the work contained in it is my own. Where work has been published that has been done by other people associated with the research group, acknowledgement is made.

Jehill Parikh
December, 2012

Acknowledgements

I would like to extend my sincere gratitude to Professor Ian Marshall for his supervision, constant encouragement and guidance during these three years and to Dr Michael Thrippleton who has supported me throughout the thesis with many collaborative works, suggestions and proof reading of this thesis. I also thank Dr Bridget Harris, Professor Joanna Wardlaw and Professor Peter Andrews for their valuable insights during these three years.

This PhD study would not have been possible without the funding from SINAPSE Collaboration (www.sinapse.ac.uk), a Pooling Initiative funded by the Scottish Funding Council and the Chief Scientist Office of the Scottish Executive and an Overseas Research Scholarship (University of Edinburgh).

I express my appreciation to all radiographers at BRIC - Elaine, Cathy, Iona, Gayle, Stewart and Jenny for their scanning support and to Mrs Moira Henderson, Irene Craig and Dr Duncan Martin for their unfailing support with the administrative issues.

I am grateful to Prof Andrew Maudsley, University of Miami, for providing his data, automated software MIDAS and accommodating me in his group at University of Miami and the financial support from Edinburgh Neurosciences (via NeuroReasearchers funds) for this visit.

My sincere thanks to my official mentor Dr Carmel Moran for her prompt and proactive advice and unofficial mentors Dr Paul Armitage and Dr Katherine Lymer for their guidance. I would also like to thank Professor Barrie Condon and Dr John Mclean (University of Glasgow) for helpful discussions.

On a personal note I'd like to thank my colleagues David, Andreas, Anna, Xin, Islem, Natalie, Paul and Gavin, for sharing their enthusiasm and helpful discussions and the staff at Brain Research Imaging Centre and Medical Physics for their immense support which has made these three years memorable.

Lastly to my parents, uncle Himanshu and Charmi for their unflagging love and support.

Thank you!

ABSTRACT

The study of brain temperature is important for a number of clinical conditions such as stroke, traumatic brain injury, schizophrenia and birth asphyxia (for neonates). A direct method to estimate brain temperature non-invasively will allow assessment of brain thermoregulation and its variation in clinical conditions.

Magnetic resonance imaging is a powerful technique widely used for diagnosis of a range of neurological conditions. All magnetic resonance procedures involve manipulation of the hydrogen nuclei in the water molecules of the human body. The resonance frequency of the water molecules is temperature dependent, thus MR thermometry is a powerful tool for non-invasive temperature measurement. Using internal reference MR spectroscopic imaging (MRSI), absolute brain temperature maps can be estimated. However a number of temperature independent factors influence MRSI data acquisition, thus a thorough validation is necessary and is the focus of this PhD study.

In this PhD study using phantom (test object) studies it was shown that optimization of the MRSI pulse sequence is necessary to reduce systematic error in temperature maps and extensive in-vitro validation of MRSI temperature mapping was performed. A custom made temperature-controlled phantom was designed for this purpose and is presented in this thesis. MRSI data acquired from healthy (young and elderly) volunteers was employed to assess regional brain temperature variations and repeatability. Finally, the feasibility of employing fast echo planar spectroscopic imaging for volumetric MRSI temperature mapping will be presented in this thesis.

CONTENTS

LIST OF FIGURES

LIST OF TABLES

ABBREVIATIONS

B_o	Main magnetic field
B_1	Secondary magnetic field
Cho	Choline
CHESS	Chemical shift selective excitation
Cre	Creatine
CSF	Cerebral spinal fluid
COV	Coefficient of variation
EPSI	Echo planar spectroscopic imaging
FID	Free induction decay
FOV	Field of View
FT	Fourier Transform
HLSVD	Hankel Lanczos singular value decomposition
IR	Inversion recovery
jMRUI	Java based magnetic resonance user interface
NAA	N-actely aspartate
MIDAS	Metabolite imaging and data analysis system
MRI	Magnetic resonance imaging
MRS	Magnetic resonance spectroscopy
NMR	Nuclear magnetic resonance
PRESS	Point resolved echo selective spectroscopy
RF	Radio frequency
ROI	Region of interest
SNR	Signal to noise ratio
STEAM	Stimulated echo acquisition mode
SVS	Single voxel spectroscopy
TE	Echo time
TI	Inversion time
TR	Repetition time
T_1	Spin-lattice relaxation time
T_2	Spin-Spin relaxation time
VOI	Volume of Interest

1 Introduction

1.1 Background

Temperature is an important physiological parameter to maintain homeostasis. Basic physiological processes such as diffusion, osmosis and enzymatic reactions are temperature dependent. The body temperature is maintained at 37^0C. This regulation is controlled by the hypothalamus of the brain, by controlling the blood flow to the core and extremities of the body. This process in which superficial tissue, skin and body hair play an important role is well understood.

In contrast to other tissues, neurons are metabolically more active and produce more heat in their normal functioning. The regulation of the brain temperature is achieved by the flow of relatively cold blood to the skull (1). In a condition such as stroke, the blood flow to brain tissue is hampered thus one can expect a higher temperature as reported by Karaszewski et al. (2). It is argued that brain temperature is related to neural activity and cerebral blood flow and directly affects the functioning of the brain cells, permeability of the brain blood barrier (BBB), and brain water and ion content (3). These factors are important for the normal physiological functioning of the brain, thus the study of brain temperature regulation in normal physiological conditions and its variation in neurological disorders such as stroke (4), traumatic brain injury (5), neonatal asphyxia (6), Parkinson's disease (7) and schizophrenia (8) is of increasing interest.

Measurement of brain temperature using thermometers requires surgical intervention and is thus limited to neurosurgical patients. In routine clinic, aural and sublingual temperatures are generally measured as a qualitative indicator of brain temperature. In clinical research, models based on the Pennes bio heat equation (9), have been employed to study regional brain temperature gradients and brain temperature variations during functional activity of the brain (10-12). These studies suggest the existence of regional

brain temperature gradients of ~1^{0}C between deeper and superficial brain structures and brain temperature variations of up to ±0.3^{0}C depending on the functional activity of the brain. These observations however lack thorough experimental verification.

In addition to the need to explore the basic process of brain temperature regulation, the advantage of neural protection offered by reducing brain temperature is of clinical interest for stroke and traumatic brain injured patients (13). Brain cooling is also reported to improve outcome in neonates with birth asphyxia (6). However important questions concerning the duration of brain cooling, modalities to be employed for cooling the brain and cooling temperature are unanswered.

Thus a validated non-invasive method which allows in-vivo (human) brain temperature measurements will not only be useful in the study of brain thermoregulation but will allow more effective development of brain cooling therapy for stroke and traumatic brain injured patients.

Techniques such as near infrared spectroscopy have been explored to measure superficial brain temperature. However, the temperature sensitivity of various magnetic resonance (MR) imaging parameters along with wide availability of MR scanners and ability to acquire MR data from both deeper and superficial brain regions make MR thermometry a promising candidate for measuring brain temperature. Using the MR phase mapping technique, temperature changes following a reference scan can be monitored, while internal reference MR spectroscopy (MRS) can be employed to measure absolute temperature (14). Additionally, using MR imaging regional cerebral blood flow and oxygenation (15) can be measured, thus MR thermometry not only provides non-invasive means to study brain thermoregulation but may also permit us to study the relation of brain temperature to a number of other physiological parameters.

1.2 Aims

The main aim of this work was to evaluate the use of MR spectroscopic imaging (MRSI) to provide absolute brain temperature maps. This includes extensive in-vitro validation of the technique, optimization of the data acquisition protocols and in-vivo application of the method to identify regional brain temperature variations in healthy volunteers.

1.3 Outline of chapters

In this thesis a number of aspects relating to acquisition and processing of MR spectroscopy imaging (MRSI) data for estimation of temperature maps will be discussed. Thus it is essential for the reader to have a basic understanding of these principles. These principles are widely described in the literature thus a brief overview of MRI, MRS and related data processing will be presented in chapter 2. In this chapter the temperature sensitivity of the various MR imaging parameters and the two main approaches used to estimate temperature using MR imaging will be also presented. It will be shown that absolute temperature can be estimated using internal reference MRS by computing the frequency difference between the temperature sensitive water peak and a temperature in-sensitive metabolite peak used as an internal reference. In this theoretical chapter a summary of the current studies which have employed internal reference MRS to measure absolute brain temperature will be provided.

In the next two experimental chapters (chapter 3 and 4) extensive in-vitro validation of MRSI temperature mapping using phantom studies will be presented. A systematic error in MRSI based absolute temperature maps identified using a room temperature phantom (test object) will be presented in chapter 3 and changes to the acquisition protocol necessary to reduce this systematic error will be discussed. In chapter 4 construction of a two chamber phantom with independent temperature control designed to validate MRSI based temperature mapping will be presented. This phantom will be employed to determine the minimum temperature difference that can be

estimated using a single MRSI scan and in studies to obtain a new set of calibration constants and to assess the effect of varying concentration of the metabolite internal reference on the precision and repeatability of the technique.

In Chapter 5 MRSI data acquired from healthy young and elderly volunteers will be employed to obtain brain temperature maps and an attempt to identify regional brain temperature gradients will be made. Practical measures for in-vivo acquisitions and repeatability will also be discussed in this chapter.

In chapter 6 a feasibility study to employ high resolution echo planar spectroscopic imaging (EPSI) acquisitions with automated MRSI data processing for obtaining brain temperature maps from multiple brain slices will be presented. It will be discussed whether in-vivo MRS temperature estimates need to be corrected for the tissue specific frequency differences between metabolite internal reference and water peaks.

Finally, in chapter 7, the main conclusions drawn from this research and suggestions for future work will be presented.

2 Temperature measurement using MRI

2.1 Introduction

The phenomenon of nuclear magnetic resonance (NMR) has been widely explored since its early discovery in the 1950's by Bloch (16) and Purcell (17). NMR has been applied in varied forms; NMR spectroscopy is routinely employed in chemistry to study molecular composition of solutions. When applied in-vivo for human use NMR spectroscopy is generally referred to as Magnetic Resonance Spectroscopy or MRS. Magnetic Resonance Imaging (MRI) is a variant of NMR used for studying structure and physiology of the human body.

MRI/S can also be used to measure in-vivo temperature non-invasively. The aim of this chapter is to describe the current state of Magnetic Resonance (MR) thermometry. Various technical aspects of MR physics that influence absolute brain temperature measurement will be discussed throughout this thesis. Thus a very basic overview of MRI and MRS is presented in sections 2.2 and 2.3 respectively and appropriate references provided to allow the reader to obtain a complete overview of the topics. In section 2.4 temperature sensitivity of several MR parameters is discussed and current studies which report absolute brain temperature estimates using MRS have been summarised. Section 2.5 describes the MRS acquisition protocol and data processing employed in this study to obtain absolute temperature maps using MRS.

2.2 Physical basis of MRI and MRS

The human body consists of around 70% water (18). A water molecule consists of two hydrogen atoms and an oxygen atom. Because of this abundance, the majority of the NMR techniques applied in-vivo are based on the magnetic properties of hydrogen (^{1}H). The nucleus of the ^{1}H atom consists of one proton. The positively charged proton combined with the inherent spin of the nucleus acts as magnetic dipole producing a nuclear magnetic dipole moment ($\bar{u}$). The interaction of the nuclear magnetic dipole with an external magnetic field can be described by either classical or quantum physics theories (19). According to the quantum physics model, the spin of an arbitrary nucleus is the vector sum of the nucleon spins and the total spin quantum number (I) can only take integer or half integer values (1/2, 1, 3/2, 2 and so on). ^{1}H nucleus contains only one proton and thus has a total spin quantum number I=1/2, as a result when placed in an external magnetic field the proton can only align itself in either of the 2 directions, in the same direction as the external magnetic field (i.e. parallel (up) or *m=1/2*) or against the field (i.e. anti-parallel (down) or *m=-1/2*). The energy difference between the two states given by equation 2.1:

$$\Delta E = -\gamma(h/2\pi)B_o \qquad (2.1)$$

Where h is the Planks constant and B_o strength of the external magnetic field, γ is the gyromagnetic ratio.

In a sample consisting of millions of ^{1}H nuclei such as the human body, a proportion of ^{1}H nuclei align parallel to the B_o and another anti parallel to the B_o according to the Boltzmann law as shown in Figure 2.1. The difference between the two population states is called the 'net magnetization' (M) of the sample given by ratio equation 2.2. The exact value of the M will depend on the number of protons or the proton density of the sample.

$$M \approx \gamma\hbar B_o / 2\pi\kappa T \qquad (2.2)$$

Where κ is the Boltzmann constant and T is the temperature in Kelvin.

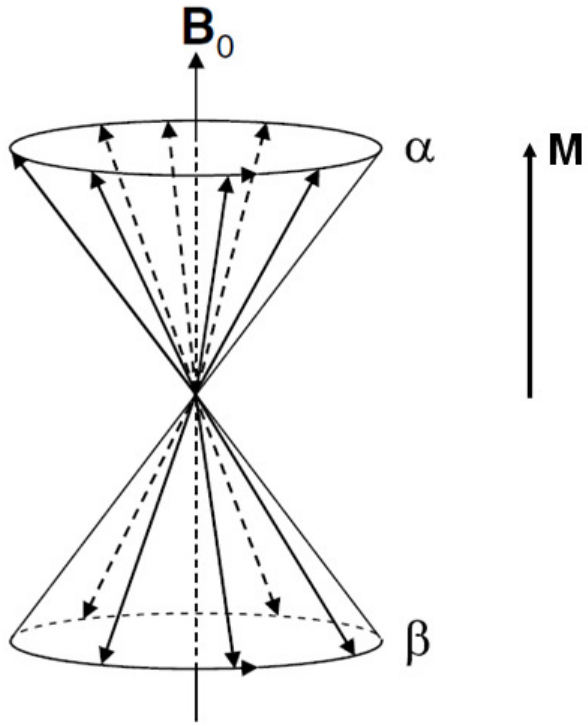

Figure 2.1 Diagram illustrating the fractional majority of the spins in a sample, which align in parallel to direction of the applied external field B_o which results in generation of net magnetisation (M).

The static magnetic field has a second effect on the protons, it generates a torque on the protons causing them to rotate or precess about B_o. The frequency at which the protons precess is known as the Larmor frequency (ω) and is proportional to the strength of the applied magnetic field (B_o) as by shown equation 2.3 and the energy difference (ΔE) between the two energy states α and β.

$$\omega = \Delta E / h = \gamma B_o \qquad (2.3)$$

Thus transition between the ground state α and excited energy state β is possible by irradiation of the system with a quantum energy (ΔE) or frequency (ω).

Although the individual protons are not stationary, without any further changes in the applied magnetic field a state of equilibrium is established. The protons precess out of phase and thus the net transverse component (M_T) of M is zero while the longitudinal component (M_L) is maximal as shown in Figure 2.1. As a result in addition to a static main magnetic field (B_o), a secondary magnetic field (B_1) is momentarily applied in MRI/S experiments to perturb the M. RF pulses are used to generate the transverse secondary field B_1. The frequency of the RF pulse applied is equal to the Larmor frequency. The amplitude of RF pulse determines the strength of B_1 and the number of spins that transition between α and β states. If the B_1 (i.e. the RF pulse) is such that it flips the longitudinal magnetisation (M_L) by 90^0, the RF pulse is known as a 90^0 pulse; 90^0 is the flip angle (θ). Once the RF pulse is switched off, a sinusoidally decaying signal is detected as the spins return to their equilibrium state. This signal is known as the free induction decay or FID.

The return of the nuclear magnetic spins to the equilibrium position is achieved using two mechanisms. Consider a scenario when a 90^0 RF pulse is applied and then switched off, the net magnetization M will be rotated by 90^0, thus M_L is zero and M_T is maximum. The protons or the spins continue to precess and interact with one another causing tiny changes in the magnetic field around each proton. This causes them to precess at a slightly different frequency and is responsible for the loss of the phase coherence in the sample and leads to a rapid loss in the M_T. This known as spin-spin relaxation, the time constant of this decay is known as spin-spin relaxation time (T_2). In practice the spins are also dephased by inhomogeneities of the external magnetic field B_o across the sample. Thus the effective spin-spin relaxation is described using T_2^* to add the effect of the B_o inhomogeneity. It should be noted that T_2^* is always shorter than T_2.

The spins give up their energy to surrounding tissues, while returning to equilibrium. This is achieved in exponential manner as M_L increases from

zero to its equilibrium with decay constant T_1, The decay constant T_1 is also known as the Spin-Lattice relaxation time. Once the spins have return to the equilibrium value, no more spin-spin relaxation can take place as M_L is maximum and M_T is zero, thus T_1 is always greater than or equal to T_2. The T_1 and T_2 relaxations are different for different tissues, and thus are the primary sources of contrasts in an image obtained using MRI as shown in Figure 2.2. In addition to the relaxation times the strength of the NMR signal (or the FID amplitude) is directly proportional to the net magnetisation M and as a result proton density of the sample.

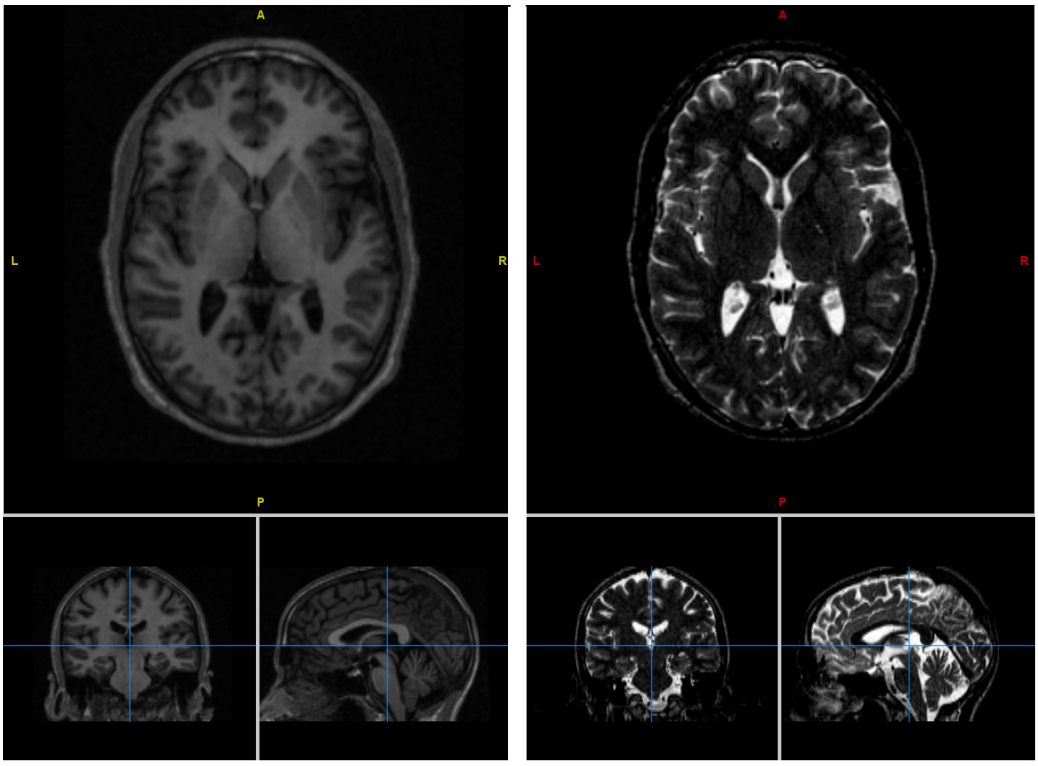

Figure 2.2 T_1 (left) and T_2 (right) weighted images of the brain acquired from a healthy volunteer.

T_2^* decay begins immediately after the end of the 90^0 RF pulse and the spins lose their phase coherence and produce a FID as shown in Figure 2.3. It is possible to separate the effects of B_o inhomogeneity and T_2 by applying a 180^0 RF after a time $TE/2$ as illustrated in Figure 2.3, this 180^0 RF pulse temporarily re-phases the spins an after additional time $TE/2$ and produces an echo with maximum at time TE after the end of the 90^o RF pulse as shown

in Figure 2.3. This application of the RF pulses in a predetermined manner to manipulate spins is know as a pulse sequence. The pulse sequence discussed here is known as a spin echo pulse sequence and it consists of one 90^0 RF pulse called the excitation pulse followed by a 180^0 refocusing RF pulse. The time *TE* after which an echo is detected is known as 'Echo time'. The variants of the spin echo sequence are used widely in MRS for localisation and will be discussed in section 2.3. It can also be used to measure T_2 relaxation of the metabolites, to simplify the appearance of the MRS signal or spectrum. Thus the spin-echo pulse sequence is one of the elementary pulse sequences. The manipulation of the spins after application of the RF pulses can be effectively described using the Bloch equations. A complete overview of these techniques is beyond this scope this work but can be obtained from text by Bernstein et al. (20).

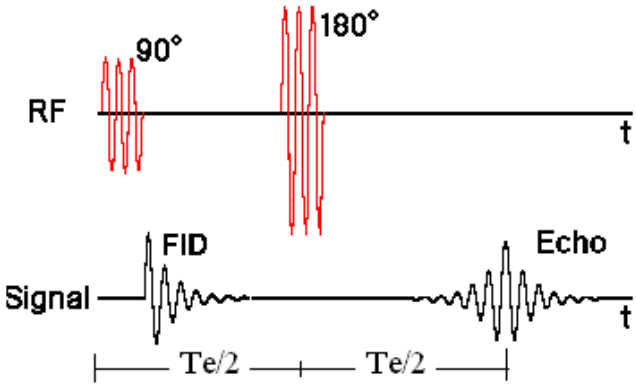

Figure 2.3 Schematic of a spin echo pulse sequence highlighting the generation of an echo with maximum amplitude at the echo time (*TE*) after application of 90^o and 180^0 RF pulses.

So far the basis of NMR has been discussed. In MRI/S experiments the sample (or the subject) is placed in a whole body magnet operating at constant field strength. As a result all the protons precess at the same frequency and if excited using a RF pulse they will all contribute to the signal and no localisation is achieved. Thus to isolate the signal from different regions of the sample, magnetic field gradients are employed. A modern MRI scanner is equipped with three orthogonal gradients to allow localisation in any direction.

The combination of the main magnetic field and the gradient produces a linear variation of the B_o across the sample, thus the Larmor frequency varies across the sample according to the strength of the gradients. Thus an RF pulse with predetermined frequency and bandwidth can be employed to excite (or select) a volume of interest (VOI). This process is known as selective excitation as a slice is selected. After slice selection, frequency encoding and phase encodings are applied to produce raw MRI data in 'k-space'. The echoes acquired using frequency encoding and phase encoding are then reconstructed by applying row and column-wise Fourier transforms to produce MRI images as shown in Figure 2.2. A comprehensive understanding of these three fundamentals to localise the MRI signal from different regions using gradients can be obtained from reference texts (18;19).

2.3 MR Spectroscopy

Using MRS, the metabolic environment of the human body can be studied. A number of isotopes (such as ^{31}P, ^{13}C, ^{15}N, ^{19}F) are commonly investigated using MRS. However ^{1}H MRS can be performed on a clinical scanner without any additional instrumentation and is the most readily available MRS technique on a clinical scanner.

The Fourier transform of a typical MRS signal i.e. FID is shown in Figure 2.4. This frequency domain representation is known as a MRS spectrum. As seen in Figure 2.4 the number of signals or peaks corresponding to the same nuclei but in slightly different chemical environments are identified at different locations on the frequency axis. The amplitude or the intensity of the peaks is directly proportional to the number of the respective nuclei with the same chemical environment in the sample. The appearance of the peaks depend on a number factors, however nuclei with same chemical environment always appear at the same frequency position (on a ppm scale) and separation between the peaks is primarily dependent on the chemical shift phenomenon as discussed in section 2.3.1. Thus by acquiring MRS spectra using a MRI

scanner, the chemical environment of the human body can be probed non-invasively.

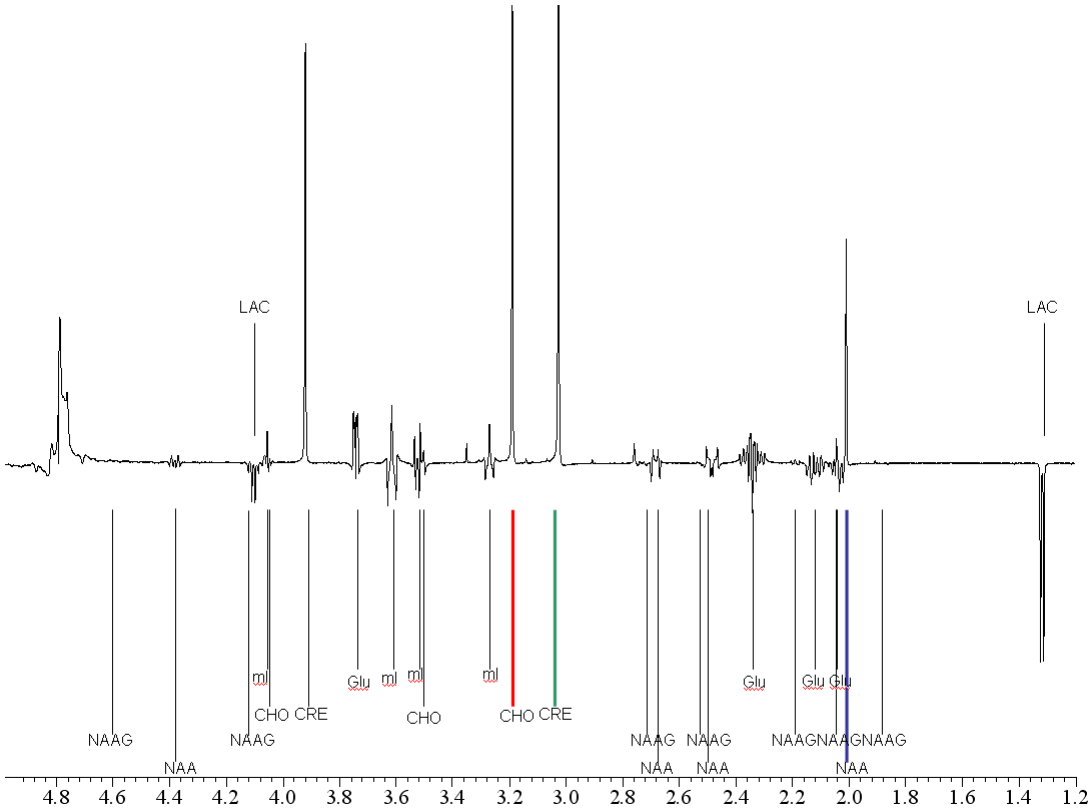

Figure 2.4 ^{1}H MRS water suppressed spectrum, plotted on a ppm scale, acquired using a 15T NMR spectrometer and echo time (TE) of 145ms from a solution containing brain metabolites (Courtesy of Dr Michael Thrippleton); The lines indicate the different metabolite peaks as identified from the literature (see section 2.3.2 for more information). A number of peaks appear in form of multiplets or are inverted due to the phenomenon called spin-spin (or J) coupling as discussed in section 2.3.1.

2.3.1 Chemical shift

In section 2.2 it was discussed that the Larmor frequency or the resonance frequency depends on the strength of the external magnetic field (B_o). However when a molecule is placed in B_o, the electrons orbiting around the nucleus produce a tiny magnetic field which opposes B_o. This is known as the shielding effect and the amount of screening is determined by the screening constant σ. This electronic shielding changes the effective magnetic field (B_{eff}) experienced by the nucleus as defined by equation 2.3 and thus changes its Larmor frequency as shown in equation 2.4.

$$B_{eff} = B_o(1-\sigma) \qquad (2.3)$$

The amount of shielding (σ) depends on the chemical environment of the nuclei, for example in a water molecule the electronegative oxygen atom reduces the charge density around the ^{1}H, as a result of which the ^{1}H atom experiences less shielding, thus it resonates at a higher frequency than in its unbound state. In contrast, ^{1}H in a methyl group, experiences relatively more shielding, as a result reduces the B_{eff} and its resonance frequency. Thus different nuclei resonate at different frequencies depending on their chemical environment.

$$\omega = \gamma B_o(1-\sigma) \qquad (2.4)$$

The shielding effects are expressed in parts per million, by computing chemical shift (δ) of the nuclei relative to a reference compound as defined by equation 2.5. Tetramethylsilane (TMS) is used as the reference compound used in ^{1}H MRS and this relative definition of δ makes it independent of the strength of the external magnetic field (B_o) thus the position of the peaks for certain nuclei will always appear at the same position in the frequency spectrum (in a ppm scale) as shown in Figure 2.4. It should be noted that the use of higher field strength increases the absolute frequency separation between the peaks and provides better spectral resolution.

$$\delta = 10^6 * (\omega - \omega_{ref}) / \omega_{ref} \qquad (2.5)$$

A number of peaks appear in form of multiplets (as shown in Figure 2.4). This is due to spin-spin coupling, due to which the local field experienced by a magnetic spin is influenced by the alignment of neighbouring spins, in addition to the electronic screening. This phenomenon is best described by two simple examples as follows. First consider a water molecule; due to the symmetrical arrangement of the water molecule the magnetic spins (i.e. the protons) have equal influence on each other. Thus the net change in the frequency of the protons due to electronic shielding and spin-spin coupling is

the same. As a result the spins (or the protons) resonate at the same frequency and no splitting is observed. However this is not true for other cases; for example in a ^{1}H-^{13}C bond (in a ^{13}C enriched glucose molecule), ^{1}H and ^{13}C have different magnetic moments and thus have different magnetic influence on each other. This results in ^{1}H and ^{13}C spins having slightly different resonance frequencies and leads to peak splitting. The peak splitting pattern (i.e. doublet, triplet or multiplet) is determined by the arrangement of the magnetic spins in the molecule and is quantified using coupling constant, J (usually in Hz). Thus spin-spin coupling is also known as J-coupling. Spin-Spin coupling makes the appearance of the peak sensitive to the echo time (*TE*) employed. For example the doublet from lactate, which appears at 1.3ppm is inverted at *TE*=145ms as shown in Figure 2.4. For temperature estimation using MRS only singlet (i.e. single peak) resonances are employed. These peaks are not affected by spin-spin (or J) coupling, thus an interested reader is referred to the text by de Graaf (19) for further details on spin-spin coupling and its applications.

2.3.2 Metabolites of interest

A number of metabolites as shown in Figure 2.4 can be studied using MRS and a vast amount of literature exists. A detailed overview of the metabolites and their uses can be found in texts by Govindaraju et al. (21) and de Graaf (19). The following paragraphs aim to provide a brief overview of the three routinely investigated metabolites, which are of significant interest to the work presented in this thesis.

2.3.2.1 N-Acetyl Aspartate (NAA)

One of the most prominent peak in a water suppressed MRS spectrum from a healthy brain is from protons in the methyl group of NAA at 2.01ppm, (highlighted in blue in Figure 2.4). Inaddition to the singlet at 2.01 ppm, multiplets from CH_2 and CH groups of NAA are observed at 2.49, 2.64 and 4.38 ppm. NAA is argued to be an indicator of neuronal density and has been widely investigated using ^{1}H MRS. A decrease in NAA levels has been

reported in stroke (22), tumours (23) and multiple sclerosis (24). Care should be taken while interpreting low NAA levels, as NAA distribution varies across the brain tissues and is higher in grey matter (8-11mM) compared to white matter (6-9mM) in a healthy brain (19).

2.3.2.2 Choline (Cho)

The trimethylamine group of Cho produces a prominent signal at 3.185 ppm (highlighted in orange in Figure 2.4). In addition to this singlet, multiplets from the CH_2 groups of choline are present at 3.50 and 4.05 ppm respectively. Choline is suggested to be associated with membrane integrity and an indicator of myelination (21). Phosphorylcholine and glyerophosphorylcholine are the two compounds which contribute to the choline peak at 3.185 ppm in a typical brain (^{1}H) MRS spectrum. In healthy adult brain choline content varies between 4.5-10.5mM and is depend on the (19).

2.3.2.3 Creatine (Cre) and phosphocreatine

The methyl protons of the creatine and phosphocreatine (combined as total i.e. t-cre) produce a dominant peak at 3.01 ppm highlighted in green in Figure 2.4. In addition a multiplet from the CH_2 group of creatine can be observed at 3.91 ppm. Creatine is believed to be an indicator of metabolism (19) and a reduction in creatine level was reported in stroke (22). The normal physiological concentration of Cre varies between 0.5-2.5mM (19).

2.3.3 Technicalities

This section will provide an overview of the technical aspects of performing MRS on a clinical scanner.

2.3.3.1 Localization

It is extremely important to localize the MRS signal, to study the chemical composition of the different organs or different structures of an organ. In the early days surface coils were used to localise the spectra, however the main

drawback of this technique for brain MRS was the problems associated with the large lipid signal from the scalp. Thus since the advent of the gradients, a series of RF pulses combined with slice selection gradients are employed for localization of MRS signals. However, unlike MRI, the MRS signal is acquired without any gradient during the readout period to preserve the chemical shift information, thus frequency encoding is not applied for MRS localisation. For a single voxel MRS (SVS), only one FID is acquired at a time using either of the two localisation techniques, i.e. Point RESolved Spectroscopy (or PRESS) as shown in Figure 2.5 or STimulated Echo Acquisition Mode (STEAM) as shown in Figure 2.6.

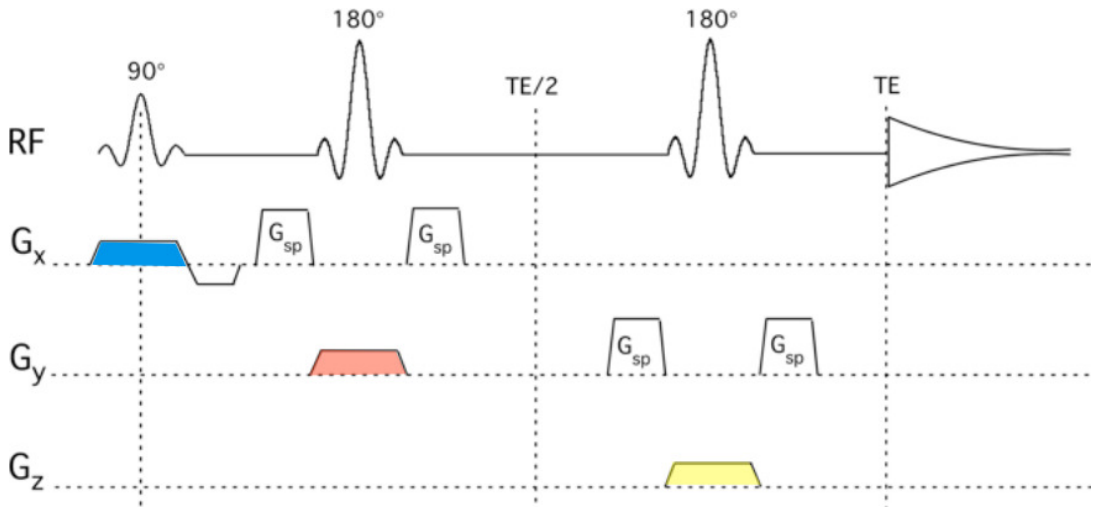

Figure 2.5 The PRESS sequence with its one selective 90° pulse and two 180° refocusing pulses applied with slice selective gradients on each of three axes used to define the VOI by the intersection of the three slices as shown in Figure 2.7.

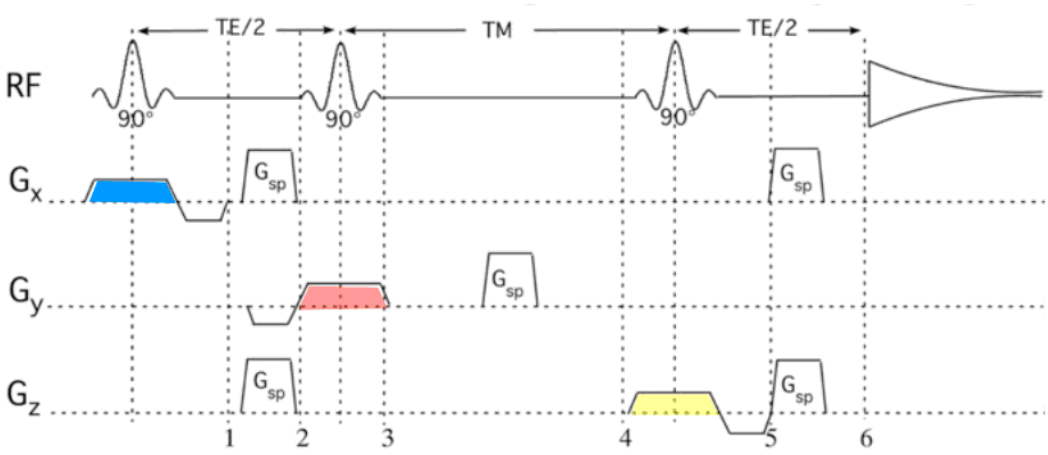

Figure 2.6 The STEAM sequence with its three selective 90°pulses and slice selective gradients on each of three axes used to define the VOI by the intersection of the three slices as shown in Figure 2.7.

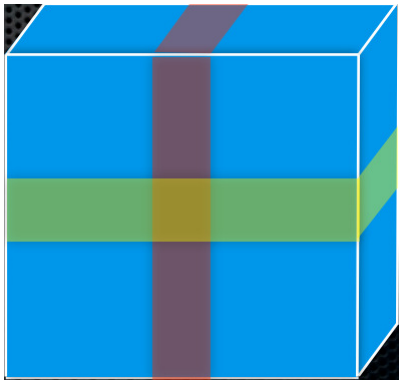

Figure 2.7 The VOI intersections of the three frequency selective RF pulses which results in localisation of the MRS signal using PRESS or STEAM.

The PRESS sequence originally described by Bottomley, (25) consists of a 90^0 pulse followed by two 180^0 refocusing pulses as shown in Figure 2.5. As the RF pulses are applied along with a gradient, the RF pulses are slice selective pulses. The 90^0 RF pulse excites (or selects) the spins along a slice in the YZ plane as the slice selective gradient is applied along the X direction. The 180^o refocusing pulses applied with slice selective gradients along Y and Z directions will refocus the spins from XZ and XY planes respectively. Thus the final FID or the echo results from the VOI produced by the intersection of the three slices as shown in Figure 2.7 and is detected after echo time *TE*. The strengths of the individual gradients and the bandwidth of the RF pulses

determine the size of the VOI, while the frequency of the RF pulses determines the location of VOI. Similarly STEAM uses 90^0 RF pulses along with orthogonal slice selective gradients to produce a stimulated echo from VOI defined by the three interactions of the three slice select gradients (26). The PRESS and STEAM both have their own advantages and a detailed discussion can be found in the texts by McRobbie et al. (18) and de Graaf (19). Briefly, STEAM is better suited when smaller *TE* needs to be used. However, PRESS is less sensitive to motion and has higher SNR as compared to STEAM.

A series of spectra can be acquired by repeating PRESS or STEAM with different gradient strengths using MR Spectroscopic Imaging (MRSI). For this purpose, the VOI is excited using PRESS or STEAM and then phase encoding gradients are applied in Y and Z directions just after the application of the last selective pulse. The strength of the phase encoding gradients is changed in every subsection repetition. The data are collected frame by frame and each frame represents a point in the raw data space or the k-space. The 2D-Fourier transform can then be employed to produce a series of FIDs in the image space. As phase encoding gradients are used to localise the signal phase of the FID varies across the VOI and phase correction is thus applied to remove this phase variation as discussed in section 2.5.2.

2.3.3.2 Voxel Bleeding

The localisation using RF pulses rarely produces a sharp square slice profile. As a result the voxel will not be a perfect cube for single voxel MRS (27). In addition to imperfect slice profiles the signal for a particular voxel in MRSI is contaminated from the signal from adjacent voxels. This phenomenon is known as voxel bleeding and is characterised by the point spread function, which has maximum at the centre and side bands spreading outwards as shown in Figure 2.8. The effect of the voxel bleeding can be reduced by using a low pass filter (or Apodization) on the raw data before application of Fourier transforms as shown in Figure 2.8.

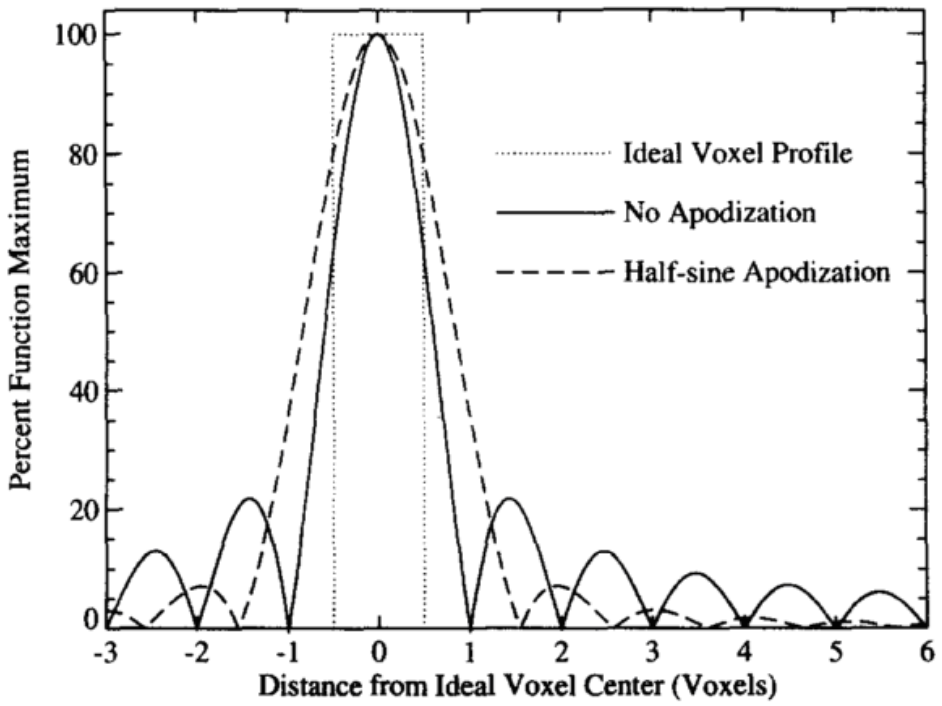

Figure 2.8 Results of Moonen et al. (27), showing the effect of voxel bleeding by using the point spread function concept; it can be seen that side lobes of the point spread function reduce when Apodization is applied.

2.3.3.3 Chemical shift mis-registration

The use of gradients for localisation poses a limitation for localisation. The strength of the gradients determines the size of the VOI, while the location of VOI is determined by the frequency of the RF pulses. However, as a result of the chemical shift (δ) effect discussed in section 2.3.1 the resonance frequency for different metabolites at the same position are different. As a result when the same RF pulse is used for localisation, the actual VOI is displaced for different metabolites based on their δ as shown by equation 2.6, which shows the amount of displacement (Δx) between the two metabolites with chemical shift difference (Δω) in the a particular direction (x), obtained using a gradient strength G_x. This is known as chemical shift-misregistration. For SVS the entire cuboid is displaced, while for MRSI there is VOI mis-registration for the three slice select directions, though the spatial encoding is not affected in the imaging plane due to double phase encoding (27).

$$\Delta x = \Delta\omega/\gamma G_x \qquad (2.6)$$

2.3.3.4 Shimming

An important pre-requisite to obtain good MRS data is to have excellent magnetic field homogeneity over the sample while acquiring MRS data (28). If B_o homogeneity is not maintained then the FID decays faster due to shorter T2*, as a result producing broader linewidths of the metabolite peaks and a low resolution spectrum as shown in Figure 2.9 B_o homogeneity is also important for effective the water suppression in MRSI as discussed in the following section.

The process of optimizing the magnetic field homogeneity is called shimming. For this reason a modern clinical scanner contains a set of shim coils. Generally automatic shim is performed in the preparatory period before signal acquisition using PRESS or STEAM based localisation. Automatic shimming routines generally use field map acquisition to compute the B_o field then the current in the shim coils is adjusted to maximise the homogeneity (of B_o) on an iterative basis. A complete overview of shimming can be obtained from the text by Koch et al. (29).

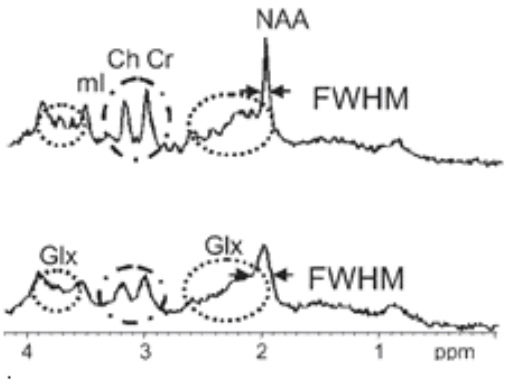

Figure 2.9 Results of Kries (28) demonstrating the importance of employing a shimming routine to optimize the B_o homogeneity across the sample to acquire MRS spectra with good spectral resolution. The top spectrum was acquired with excellent B_o homogeneity while the bottom spectrum was acquired with non-uniform B_o.

2.3.3.5 Water suppression

Water is the most abundant compound in the human body, the concentration of the metabolites at physiological levels is ~10000 times lower than that of the water. As a result a large signal is observed from water at 4.7 ppm in a typical MRS spectrum as shown in Figure 2.10. Water suppression techniques were introduced to avoid the problem of limited digital resolution for analogue to digital converters (ADC) of signals with a large dynamic range. This problem doesn't exist today and modern day ADCs have sufficiently large range to allow metabolite detection from the same spectrum which contains a large water signal. The large water peak can be used for spectrum phasing, B_o estimation and estimation of sensitivities for multi-coil elements (30). The main problem that limits the use of non water suppressed MRS is the presence of side bands and large baseline distortions (31). These artifacts affect temperature estimation and it is necessary to suppress the water signal to obtain uniform temperature maps (see Chapter 3).

A number of water suppression techniques are available and a elaborate review is provided by Zheng et al. (32). While performing in-vivo MRS using clinical scanners water suppression (WS) by frequency selective CHESS pulses (33) is widely used. The basic use of CHESS pulses in MRS was described by Haase et al. (33). The CHESS pulses consist of frequency selective RF pulses on resonance with the water frequency. This selective RF pulse will only excite the water spins, after which a crusher gradient is applied to dephase the signal from water spins.

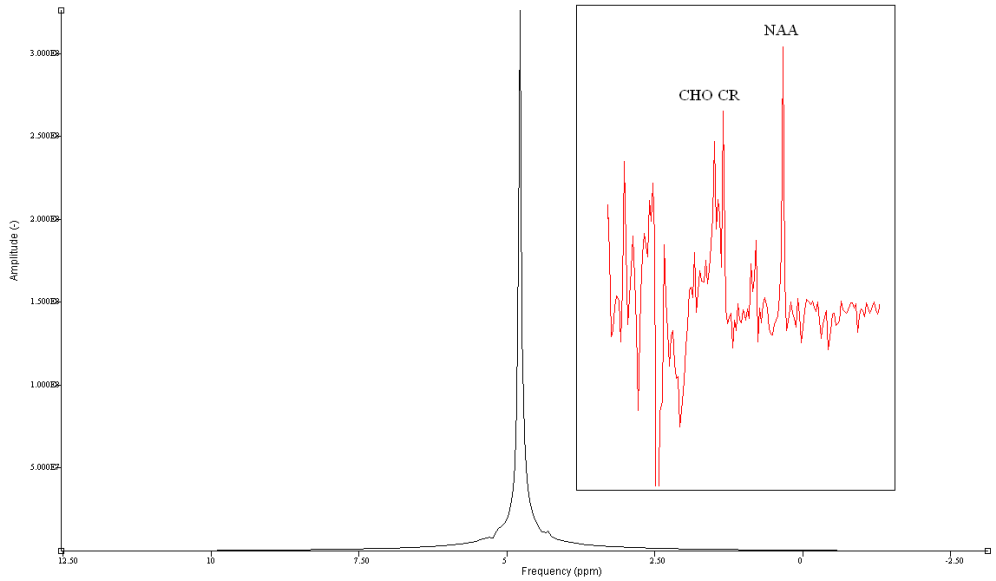

Figure 2.10 Typical non water suppressed spectrum, acquired using a room temperature phantom containing brain metabolites (NAA, Cho, Cr) at physiological concentration. Insert shows the spectrum obtained after removal of the water peak using software filters (e.g. HLSVD) The metabolite peaks are distorted compared to the water suppressed spectrum shown in Figure 2.11.

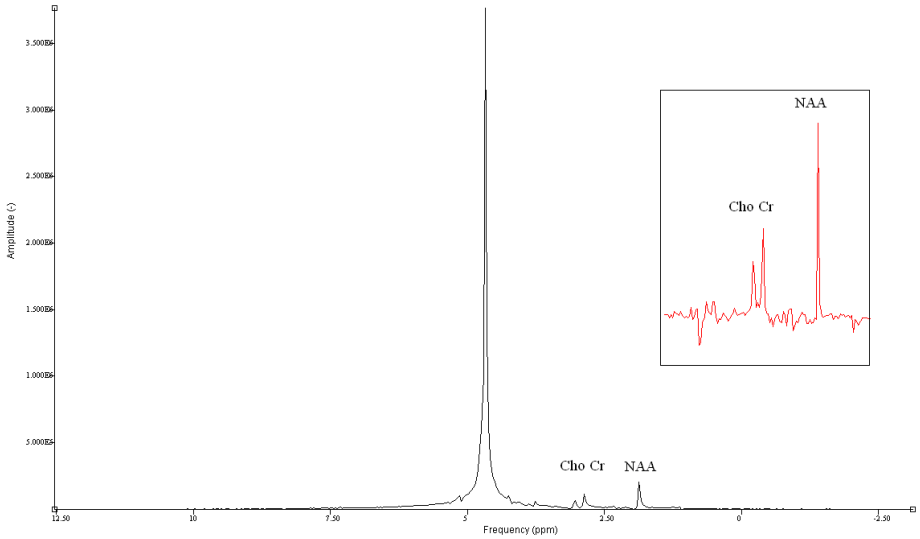

Figure 2.11 Typical water suppressed spectrum (suppression factor ~90), acquired using a room temperature phantom containing brain metabolites (NAA, Cho, Cr) at physiological concentration. Insert shows the spectrum obtained after removal of the residual water peak using software filters (e.g. HLSVD). The metabolite peaks could be easily identified at this level of water suppression.

The CHESS pulses are applied prior to the localisation using PRESS or STEAM. To avoid recovery of the water signal by T_1 relaxation, the delay between CHESS and localisation (τ) should be minimal. Commonly a number (2-4) of CHESS pulses are used to achieve strong water suppression. A WS spectrum using 3 CHESS pulses (bandwidth=75Hz, τ=48ms, WS factor ~90) is shown in Figure 2.11. In contrast to the non WS spectra shown in Figure 2.10, metabolite peaks (NAA, Cr, Cho) can be easily identified using WS.

It is crucial that CHESS pulses are applied on-resonance with the water frequency; off-resonance CHESS pulses may produce spectra with distorted shape of the water peak (34). Off-resonance CHESS pulses also produces an increase in the amplitude of the residual water peak as shown in Figure 2.12. B_o variations encountered over larger VOIs (e.g. in MRSI) may produce inefficient water suppression and thus it is important to use efficient shimming algorithms to maximize B_o homogeneity across the FOV (27).

A uniform T_1 cannot be guaranteed across a large FOV as encountered in MRSI experiments, thus it is important to apply optimized water suppression using CHESS to avoid signal recovery through T_1 effects. A simple approach has been proposed by Ogg et al. (35), they suggest varying the flip angle of the RF pulses use for CHESS, to make it insensitive to T_1 and B_1 variation on a case by case basis. The method is known as WET (water suppression enhanced through T_1 effects). WET is also reported to produce uniform water suppression off resonance when compared with 1-CHESS and 3-CHESS pulses based water suppression as shown in Figure 2.12

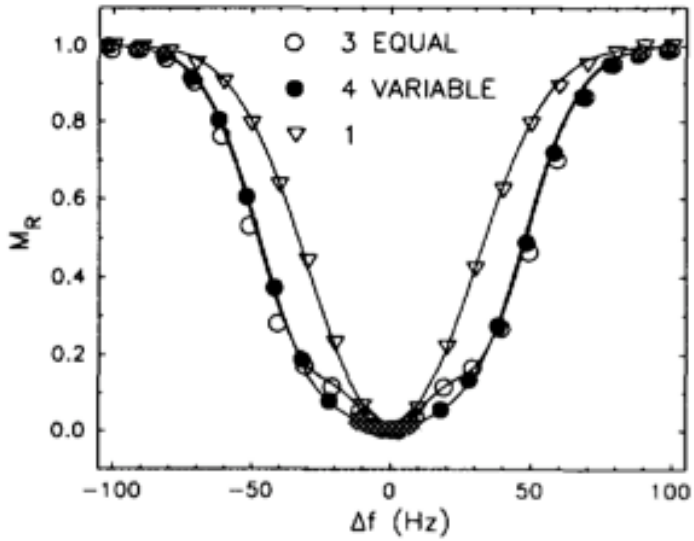

Figure 2.12 Results of Ogg et al. (35), demonstrating the effect of the off-resonance water suppression CHESS pulse on the amplitude of the residual water peak for different (1 pulse, 3 fixed flip angle CHESS pulses and 4 variable flip angle CHESS pulses i.e. WET method).

Lastly, it is essential to use high power crusher gradients which completely dephase the water spins when CHESS is employed for water suppression otherwise a residual magnetisation refocuses and unwanted echoes appear in a spectrum (34). To avoid unwanted echoes after CHESS Moonen et al. (34) suggests the use of 2 or more CHESS pulses applied with different amplitudes of crusher gradients. In addition, B_o inhomogeneity also limit complete spoiling, as a result additional crusher gradients in the PRESS sequence (as shown in Figure 2.5) are routinely employed to avoid spurious echo artifacts (27).

2.4 MR Thermometry

MR thermometry is based on temperature sensitivity of a number of MR imaging parameters, which include relaxation times T_1 and T_2, proton density, water diffusion coefficient and proton frequency. The reviews by Quesson et al. (36) and Rieke et al. (37) provide an excellent overview of the physical basis of the temperature sensitivity of MR imaging parameters and the various approaches employed to measure temperature changes. Among the various parameters, water or proton frequency shift (PFS) is considered to be the most reliable and robust parameter to estimate temperature (38). While the temperature sensitivity of other imaging parameters allows us to monitor temperature changes, absolute temperature can only be measured using the temperature sensitivity of the proton frequency. The temperature sensitivity of proton frequency is discussed in section 2.4.1, while in section 2.4.2 various studies which explore this temperature sensitivity of the proton frequency to estimate brain temperature are summarised.

2.4.1 Proton frequency shift

The protons in the liquid water molecules form covalent bonds (indicated by solid lines in Figure 2.13) with the oxygen atom. However the electronegative oxygen atom reduces the electron charge density around the protons, thereby introducing a polarity in the water molecule and leads to formation of hydrogen bonds (indicated by dotted line in Figure 2.13). As a result of this hydrogen bonding, different water molecules are connected as illustrated in Figure 2.13. In section 2.3.1 it was described that the resonance frequency not only depends on the applied external magnetic field B_o but also on the screening due to the electron cloud. The electron cloud distribution around the O-H bonds of the water molecule varies with temperature (T) changes as illustrated in Figure 2.13. Thus a change in temperature changes the shielding constant (σ), which in turn produces a change in the resonance frequency of the proton. This effect was first reported by Hindman (39) in 1966 who reported a temperature coefficient of chemical shift of 0.01 ppm/^{0}C for pure water.

While the electronic screening for water is temperature dependent, the screening for a number of metabolites is temperature independent. Thus the resonance frequency of these metabolites is temperature independent. As a result absolute temperature can be estimated by calculating the frequency difference (Δ) between the temperature sensitive water peak and temperature independent metabolite (typically NAA) from a MRS spectrum using equation 2.6, where A and B are calibration constants.

This basic principle is illustrated in Figure 2.14. As a metabolite signal is used an internal reference, this method is known as internal reference MRS thermometry. It should be noted that an increase in temperature increases the electronic shielding which in turn reduces the Larmor frequency of the water molecule (also known as upfield shift).

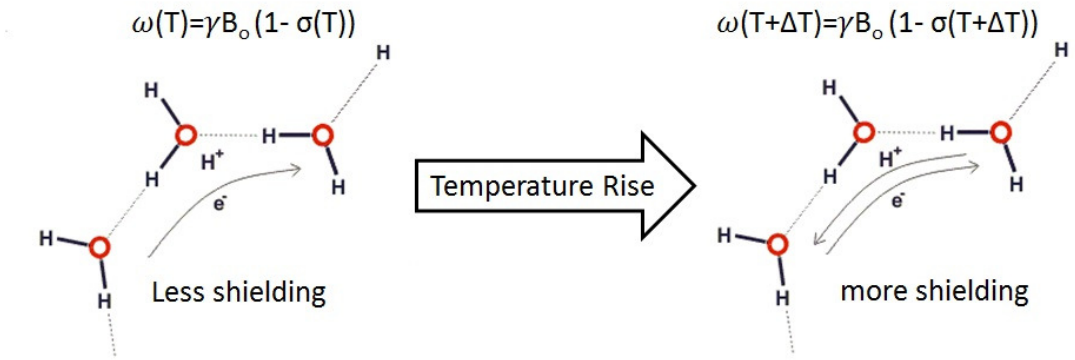

Figure 2.13 Temperature sensitivity of hydrogen bonds in a water molecule, illustrating the changes in the electronic screening with temperature rise. It should be noted that temperature changes may influence the bond angle of the hydrogen bonds but these changes are not shown here for simplicity.

$$T = A + B\,(\Delta_{water\text{-}reference}) \qquad (2.6)$$

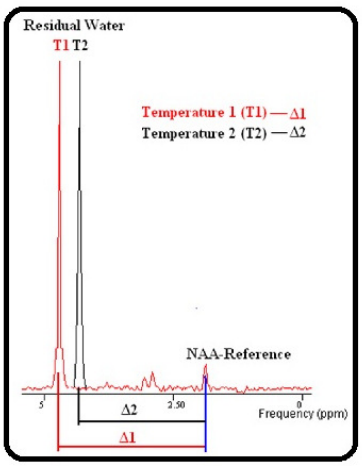

Figure 2.14 Illustration of proton frequency shift with temperature variations in typical ^{1}H MRS spectrum of solution containing brain metabolites used to estimate temperature by computing frequency difference (Δ) between water and reference (NAA) peak.

Changes in proton frequency with respect to temperature also produce a change in the phase information in MR image acquired using a gradient recalled echo sequence (GRE), thus acquiring a series of phase images and subtracting them from a reference image (generally the first image of the series), provides another way to monitor temperature changes. The phase mapping sequences are fast, compared to spectroscopic localisation and have better spatial resolution. Thus phase mapping methods are widely used for tissue ablation using LASER beams or high frequency focussed ultrasound under MRI guidance (37). MR imaging is used for both temperature monitoring and visualizing of the target tissues like tumours and fibroids during the course of the therapy. However it is only possible to measure temperatures changes from a baseline using this method. The main differences between these two approaches are summarised in Table 2.1. It should be noted that in contrast to the phase mapping method, internal reference MRS thermometry uses the frequency difference between the reference peak and water acquired under the same experimental conditions and is thus reported to be insensitive to the errors that may be introduced due to changes in magnetic field variation and tissue susceptibility (38).

Method	Internal reference MR Spectroscopy	Phase mapping (MR Imaging)
Absolute temperature	Possible	No, Only temperature change
Temperature maps	Possible (but lower spatial resolution)	High spatial resolution
Speed	Longer acquisition time but single acquisition needed	Relatively fast, but 2 or more acquisition necessary
Sensitivity to motion	Low	High
Tissue susceptibility effects	Low	High
Calibration	Extremely crucial	Less important
Application	Determine absolute temperature	MR guided tissue ablation

Table 2.1 Summary of comparisons of PFS based MR thermometry methods.

2.4.2 Absolute brain temperature measurement

The need for a non-invasive technique to measure absolute brain temperature has been presented in Chapter 1. Techniques such as near infrared spectroscopy and microwave thermometry have been explored for measuring brain temperature. These signals can penetrate only to a few (2-3) mm in-vivo and thus can only be applied to measure the temperature of the surface of the brain. In contrast, MRS data can be acquired from deep and superficial brain structures and can be readily employed to measure temperature using internal reference MRS thermometry. A number of studies have been published, which employ internal reference MRS thermometry to measure absolute brain temperature. These studies are summarised in the following sections.

2.4.2.1 Validation studies

The first reports which exploits the linear temperature dependency of the proton frequency to measure absolute brain temperature using internal reference MRS were published independently by Corbett et al. (40) and Cady et al. (41). These two independent reports can be argued to be the 'proof of concept' studies, where MRS data was acquired from temperature controlled phantoms (or test objects) and animals (piglets) at different temperatures in the range 23-40^{0}C by Corbett et al. (40) and between 30-39^{0}C by Cady et al. (41). Both studies confirmed that the frequency difference between water and the NAA internal reference ($\Delta_{water-naa}$) varied linearly with temperature using phantom and animal data. Fibre optic temperature probes were used to monitor the temperature of the phantom/animals during temperature cycling. Regression analysis was performed between the frequency difference $\Delta_{water-naa}$ (measured in ppm units) and the temperature (in ^{0}C) measured using fibre optic thermometers to obtain calibration constants A and B as shown in Table 2.2. Corbett et al. (40), also report variation in pH of the sample had little effect on the calibration constants (A and B). These experiment were performed on the high field strength research scanners, Corbett et al. (40) employed a 4.7T scanner while Cady et al. (41) used a 7T scanner. In

addition, Cady et al.(41) employed internal reference MRS to estimate the temperature of the thalamus of the brain for 6 normal human infants using a 2.4T scanner and report a mean thalamic temperature of 38.1 ^{0}C (SD=0.4 ^{0}C) for these 6 infants.

In their next report, Corbett et al. (42) employed a 1.5T clinical scanner and provided the first insights into regional brain temperature variation. In this study Corbett et al. (42) used single voxel internal reference MRS to estimate temperature of superficial (frontal lobe) and deeper structures (thalamus) of the brain, for 10 healthy volunteers. They report a mean temperature of 37.2 ^{0}C (SD 0.6 ^{0}C) for the frontal brain area. This was lower compared to the mean temperature of 37.7 ^{0}C (SD 0.6 ^{0}C) reported for the thalamus, which is a deeper structure. They also report lower forehead temperature (mean 34.0 ^{0}C SD 1.1 ^{0}C) and oral temperature (mean 36.5^{0}C SD 0.6 ^{0}C) measured after the scans for these volunteers. The calibration constants (A and B) were obtained using animal (piglets) experiments at the same field strength (i.e. 1.5T), by performing regression analysis between the MRS data and fibre optic temperature measurements as previously discussed. In this study the feasibility of using different internal reference (tri-methylamines (TMA) of Choline at ~3.20 ppm) rather than NAA was also investigated. Choline was argued to be a suitable substitute to NAA as internal reference in conditions where NAA levels decrease e.g. stroke.

In 2001, Jayasunder et al. (43), used single voxel internal reference MRS thermometry to estimate the brain temperature of various tumours. They report a range of temperature variations (29.7~43^{0}C) in this study for different types of tumours. The number of subjects used to obtain temperature estimates for various tumour types varied in the range 1 to 31. The large range of temperature variations reported in this study indicated the necessity for pooling a large number of dataset to assess whether temperature is important in the study of tumour physiology. NAA was employed as the internal reference to obtain absolute brain temperature from the MRS data.

The large variation in temperature estimates may have been a result of the reduced NAA levels as previously discussed, however NAA levels were not presented in this study.

The studies discussed so far have employed SVS to measure temperature from isolated regions of the brain. In contrast, MRSI allows acquisition of a series of spectra from across volume of interest (VOI) and may allow measurement of spatial distribution of temperature. Validation of MRSI based absolute brain temperature mappings was performed by Marshall et al. (44). They employed a standard MRSI sequence based on PRESS localisation (acquisition time ~10 minutes) on a 1.5T clinical scanner. Firstly, single voxel MRS was employed to collect MRS data from 20 volunteers to obtain the frequency difference between water and internal reference (NAA) from the occipital region of brain assumed to be at 37^0C and was used to obtain a working formula (equation 2.7) to estimate temperature on a voxel by voxel basis from MRSI data by using the temperature sensitivity of the water peak (of 0.01ppm/^{0}C) from the literature.

$$T=37+100(CS_{NAA}-2.035) \qquad (2.7)$$

Equation 2.7 is based on the fact that that scanner is always tuned to resonance at water frequency and as result water peak is always at resonance at 4.7 ppm and thus as a result of temperature variations the frequency of the NAA peak (CS_{NAA} in ppm) appears to vary. Thus it is only necessary to estimate the frequency of the internal reference (NAA) to estimate temperature. Equation 2.7 was used to estimate temperature maps from the water suppressed MRSI data acquired from 40 patients with acute stroke. Diffusion weighted imaging (DWI) was employed to delineate stroke area. The temperature maps were then overlaid on the DWI data and a comparative study of MRS temperature estimates in stroke area and normal tissue was performed on a subject by subject basis. It was found that, on average, the stroke lesion had elevated temperature compared to normal

tissue types 0.17^{0}C, however SD was high (~2^{0}C). The NAA amplitude in the stroke lesion was lower by 30% compared to normal tissue. Thus spectral simulation was employed to assess the effect of the reduced NAA amplitude on temperature estimation. The effect of varying the linewidths of NAA peak on temperature estimation was also estimated in a simulation study. The result of simulation study indicates variability in temperature estimates increases as the amplitude of NAA reduces or the linewidths (LW) of the NAA increases. These results were explained using the Cramer Rao framework for model parameter estimation (i.e. the frequency of the internal reference NAA) using equation 2.8, where t_s is the sampling time.

$$CRB_{\omega} = 2\sqrt{2}\ (-LW \times \Pi)^{3/2}\ \sqrt{t_s}\ (1/SNR) \qquad (2.8)$$

A similar study (45) was reported by the same group to assess the association of elevated brain temperature with metabolic rate and poor outcome in stroke patients. For this purpose patterns of increase in the lactate concentration and temperature evaluation were assessed in stroke patients. It was not possible to associate temperature or lactate variations with severity of the stroke and thus it was not possible to associate augmented metabolism due to temperature changes to explain early fever in severe stroke and its poor outcome.

A comparative study between, single voxel MRS and multi voxel MRSI internal reference thermometry was reported by Childs et al. (46). A 3T scanner with PRESS based localisation and CHESS based water suppression at a reduced level was employed to collect SVS and MRSI data from 8 healthy volunteers. SVS was reported to have an excellent precision (within 0.2^{0}C) for temperature measurement. The accuracy of MRSI temperature estimates was within 0.8^{0}C. The broader linewidths obtained due to a number non temperature dependent of factors such as shimming, B_o inhomogeneity and heterogeneity of the brain were argued as the primary reasons for this relatively large variability in MRSI temperature mapping.

This study also reports difference between brain and body temperature and indicates brain temperature to be higher in comparison to body temperature by (0.1-0.8^{0}C). SVS was performed at 4 different locations (from surface to core) to identify a brain temperature gradient. The absolute temperature estimates indicate a slightly higher (~0.25^{0}C) core brain temperature, but a detailed discussion on this finding was not provided.

A recent report by Cady et al. (47) suggests the reproducibility of internal reference MRS thermometry can be improved by using amplitude weighted combination of the temperature estimate obtained using different internal references (Ch, Cre, NAA). In the first part of the study, animal experiments were used to obtain calibration curves using three different internal references as shown in Table 2.2. The temperature was then estimated using the frequency difference ($\Delta_{water\text{-}reference}$) for these 3 internal references (NAA, Cre and Cho) and a final temperature was obtained by an amplitude weighted combination of the temperature estimates obtained using different metabolites used as internal reference. This method was used to obtain brain temperature estimates from the thalamus (TH) and the occipito-parietal lobe (OP) of 8 human infant brains. The mean (SD) of temperature estimates using AWC for the TH and OP were 37.49 ^{0}C (0.49 ^{0}C) and 38.14 ^{0}C (0.40 ^{0}C) respectively, and indicates a regional difference in brain temperature. The SD of the temperature estimates were slightly lower (~0.49 ^{0}C) when AWC was employed, compared with an SD of ~0.6^{0}C when a single internal reference (NAA or CH or Cre) was employed to estimate temperature. It was thus argued that AWC improves reproducibility and makes the temperature less insensitive to pathological or regional variation of the metabolite amplitudes.

2.4.2.2 Calibration Studies

A number of studies as discussed in the previous section have validated internal reference MRS thermometry to measure brain temperature. However inaccuracies in absolute temperature estimates may arise if the calibration constants (i.e. A and B see equation 2.1) are inaccurate. Thus a comprehensive study of calibration was performed by Zhu et al. (48). This study was performed on rat brain using an 11.74T scanner. Water circulation pads were employed to vary body temperature which in turn varies brain temperature of the animals. A fibre optic temperature probe was used to measure the brain temperature invasively. Single voxel MRS data using high bandwidth RF pulses was employed during temperature cycling. Regression analysis was performed on the fibre optic temperature measurement and frequency difference ($\Delta_{water\text{-}reference}$) calculated at various temperatures to obtain calibration constants A and B. Three metabolites (NAA, Cr, Ch) were investigated as internal reference, the calibration coefficients obtained using three metabolites are shown in Table 2.2. Zhu et al. (48), suggest temperature estimates obtained using calibration at high field to be accurate within 0.1 ^{0}C.

Another calibration study was reported by Covaciu et al. (49), who employed an aqueous solution and temperature controlled phantom for temperature cycling for calibration using a 1.5T Philips scanner. The results of this calibration study are shown in Table 2.2. In this study Covaciu et al. (49), acquired single voxel MRS data from the occipito parietal region just above the corpus callosum from 18 healthy volunteers. Internal reference MRS temperature estimates were similar (mean 38.3^{0}C SD 0.5^{0}C) when different internal references (NAA, Cr, Ch) were employed. The rectal temperature measured after scanning was lower by 1.3 ^{0}C (+/-0.5^{0}C) compared to brain temperature estimates obtained using MRS. Covaciu et al. (49) suggest the brain temperature estimate will be lower (mean 37.7^{0}C SD 0.6^{0}C) if the calibration suggested by Cady et al. (41) was employed. Thus it is critical to investigate calibration issues in further detail.

A recent report by Vescovo et al. (50;51), assesses the effect of varying ionic strength and protein content on the calibration constants A and B. A temperature controlled phantom was used for temperature cycling. A number of different aqueous solutions with varying ionic strength and protein content as shown in Table 2.2 were employed to obtain calibration constants. It was observed that the calibration constants depend on the ionic strength and changes in ionic strength can introduce an error of $+/-2^0$C in absolute temperature estimates. They also report that the calibration constant is sensitive to protein content and thus recommend using a solution or species which mimics human tissue to obtain calibration constants.

Study	Internal Reference	Slope (^{0}C)/ppm	Intercept (^{0}C)	Δ at 37 (^{0}C)	Sample/Solution
Corbett et al. (40)	NAA	-97.26	293.3	2.6352	Water solution NAA (20mM), KCl (150mM), $MgCl_2$ (1.5mM), lactate (6.6 mM)
Cady et al.(41)	NAA	-97.6	293.1	2.6240	Water solution, NAA (10mM)
	NAA	-94	286.9	2.6585	Piglet
Corbett et al. (42)	NAA	-72.2	228.2	2.6482	Swine
	Choline	-77.8	149.6	1.4473	
Corbett et al. (52)	NAA	-82.3	255.9	2.6598	Dog
	Choline	-70.1	140	1.4693	
Zhu et al. (48)	NAA	-103.8	313.7	2.6657	Rat
	Creatine	-101.7	205.6	1.6578	
	Choline	-106.1	194.4	1.4835	
Covaciu et al. (49)	NAA	-97.1	296.1	2.6684	Water solution Cho, (25mM), Cre (50mM) and NAA (50mM), pH~ 7.2
	Creatine	-94.8	193.3	1.6487	
	Choline	-100.8	184.5	1.4633	
Vescovo (51)	NAA	-100.9	303.5	2.6418	KCl(83mM),NaCl (26mM),water, NAA (25mM), ph buffer
	NAA	-100.6	302.3	2.6372	KCl(136mM),NaCl (20mM),water ,NAA (25mM), ph buffer
	NAA	-99.7	301.6	2.6540	Water solution NAA (25mM) phosphate buffer (20mM, pH~7) NaCl (0mM)
	NAA	-98.92	299.1	2.6496	Water solution NAA (25mM) phosphate buffer (20mM, pH~7) NaCl (50mM)
	NAA	-100.3	302.7	2.6491	Water solution NAA (25mM) phosphate buffer (20mM, pH~7) NaCl (100mM)
	NAA	-102.7	307.6	2.6349	Water solution NAA (25mM) phosphate buffer (20mM, pH~7) NaCl (200mM)
	NAA	-101	305.4	2.6574	Water solution NAA (25mM) phosphate buffer (20mM, pH~7)NH_4Cl(100mM)
	NAA	-105.8	320.6	2.6805	Water solution NAA (25mM) phosphate buffer (20mM, pH~7) 10% BSA
Cady et al. (47)	NAA	-92.2	282	2.6573	Piglet
	Choline	-88.7	166.4	1.4589	
	Creatine	-99	199	1.6364	

Table 2.2 Calibration constants (A and B) reported in the literature; also reported are nominal frequency difference (Δ) anticipated at 37^{0}C for the respective calibration curves.

2.4.2.3 Application Studies

The studies discussed so far demonstrate that internal reference MRS thermometry can be considered a validated method to non-invasively investigate brain temperature. This method was employed to probe temperature and its association with cerebral blood flow (CBF) by Katz-Brull et al. (53) and Kauppinen et al. (54) . Katz-Brull et al. (53) used NAA as internal reference to non-invasively estimate brain temperature during visual stimulation. For this purpose single voxel MRS was performed at the location of the visual cortex, both at rest (i.e. no visual stimulation) and during the period of stimulation on 9 healthy volunteers. The mean (SD) temperature at rest was 36.6 ^{0}C (0.8^{0}C) and did not change significantly over the course of the visual stimulation (mean change 0.1^{0}C $P>0.05$). It was argued that increased temperature due to the increased metabolite activity during the visual stimulation was regulated by an increase in the relatively cooler CBF to the site of the simulation, where the cooler CBF acts as a heat sink. Kauppinen et al. also report similar findings. In contrast to only one single voxel MRS in the visual cortex, Kauppinen et al. employed 3 three single voxels (2 placed at the site of activation and one away from the activated area). However for all of the three voxels the temperature variation was within the precision of the technique (0.2^{0}C). In addition to visual stimulation experiments on 11 volunteers, which result in increase of the CBF and oxygenation, Kauppinen et al. measured temperature changes only due to increase in the CBF, by inducing hypercapnia in 8 volunteers. They report a reduction in temperature (Mean 0.32^{0}C SD 0.33 ^{0}C $P<0.05$) when hypercapnia was employed and argue these results indicate a complex relation between the CBF and brain temperature in normal physiological conditions.

The MRSI method proposed by Marshall et al. (44) has also been used to assess the feasibility of brain cooling using a convection based device by Harris et al. (55), who employed a device which consists of a nylon hood to circulate cold air (Temperature=14.5^{0}C, flow rate 42.5 L/s) to cool the head

and thus brain. The device also consists of an additional collar arrangement and allows to cool the blood flowing in the carotid arteries in neck region and thus cools both the head and blood flowing into the brain. The device was used to cool the brains of 5 volunteers in 2 different ways, by application of head cooling only for the first case and both head and neck cooling for second. It was found that head and neck cooling reduced mean temperature of the brain by 0.37^0C at the slice location of basal ganglia after about 30 minutes of cooling. In contrast when only head cooling was applied then brain temperature was reduced by mean value of 0.45^0C after 30 minutes cooling. A regional analysis showed that this cooling method is only able to cool the superficial areas of brain as cooling did not penetrate to deeper regions of the brain.

Internal reference MRS thermometry was also used to study brain temperature changes in schizophrenia patients by Shiloh et al. (8). In this study single voxel MRS data were acquired from three different gray matter regions (frontal cortex, anterior thalamus and occipital cortex). The MRS temperature estimates obtained using NAA as the internal reference as shown in Table 2.3. It was reported that the temperature of the frontal cortex was significantly lower ($P<0.05$) in patients compared to healthy aged matched volunteers as shown in Table 2.3, while that for thalamus and occipital cortex were not. They also report a temperature gradient (~1.1^0C) between the frontal and occipital regions was correlated with the psychopathology scoring ($R=0.61$, $P=0.083$) for schizophrenia patients. Based on these results they argue decreased metabolic activity in the frontal cortex of Schizophrenic patients was the reason for lower temperature estimates. Their data also suggest the minor regional brain temperature difference in healthy volunteers with the deeper brain structure (i.e. thalamus) being slightly warmer than the surface regions (frontal and occipital cortex) as shown in Table 2.3. This regional temperature difference is not same for Schizophrenia patients as seen in Table 2.3. It was also found that mean

brain temperature (i.e. mean of the three regions) was warmer compared to oral temperature estimates by ~0.6^{0}C for healthy volunteers.

Type	No of subject	Frontal Cortex T (^{0}C)	Anterior Thalamus T (^{0}C)	Occipital cortex T (^{0}C)
Schizophrenia Patients	9	36.7 (1.1)	37.5 (0.8)	38.0 (1.1)
Healthy volunteers	10	37.6 (0.9)	37.9 (0.9)	37.8 (0.5)

Table 2.3 Results of the Shiloh et al. (8), showing regional temperature variations in healthy volunteers and schizophrenia patients using internal MRS thermometry.

2.4.2.4 Summary

To summarise, the temperature sensitivity of proton frequency and the two methods which employed temperature dependent proton frequency shifts to measure temperature changes (using MR phase mapping) and estimate absolute temperature (using internal reference MRS) were discussed. It was seen that a number of studies have employed single voxel MRS to measure brain temperature at specific locations. These studies indicate regional variation in brain temperature. Temperature maps can also be computed using MRSI and will provide a time efficient method to study regional brain temperature variations, however only a few studies have employed MRSI. Thus further validation of the MRSI based absolute temperature mapping is necessary and is the primary focus of this PhD study.

2.5 MRSI acquisition and processing

The proton frequency shift varies linearly with temperature with a coefficient of 0.01ppm/^{0}C, which at 1.5T translates to 0.64Hz/^{0}C. This temperature sensitivity of proton frequency is small compared to the Larmor frequency (63.5MHz at 1.5T). Thus it is crucial to use a robust acquisition protocol and processing protocol to measure these small changes in proton frequency and precisely estimate temperature. The key factors which affect the choice of the acquisition parameters of MRSI data for temperature mapping and MRS processing will be discussed in the following paragraphs.

2.5.1 MRSI acquisition

The appearance of the spectra acquired from a particular metabolite, depend on a number of factors such as echo time *TE*, J-coupling, T_1, T_2 and T_2^* as discussed in section 2.3.1 and have been widely studied. For temperature estimation using MRS it necessary to compute the frequency difference ($\Delta_{water\text{-}reference}$) accurately. The reference generally used is the NAA singlet (i.e. single peak) at 2.01 ppm. This peak can be easily detected in MRS spectrum for a healthy volunteer at all echo times. However when a short echo time is employed, a complex spectrum is produced as shown in Figure 2.15. This is due to the presence of metabolites like glutamate and glutamine, which produces complex peaks (multiplets) between 2.00 and 2.46 ppm (due to spin-spin coupling as previously discussed in section 2.3.1) and shorter T_2. The signals from the glutamate and glutamine decay faster and produce a simple spectrum with a longer echo time (>70ms) as shown in Figure 2.16. Thus use of longer echo time is preferred as it produces a simpler spectrum. PRESS sequence is best suited when long echo times are used and it also offers better SNR and less sensitivity to motion compared to STEAM (18). Thus a PRESS based localization was used to acquire MRSI data for all the experiments reported in this thesis. The detailed acquisition parameters of the pulse sequence are reported in Table 2.4. In addition it is extremely important to reduce the magnetic field inhomogeneity to obtain

good quality MRSI data as discussed in section 2.3.4, thus manufacturer provided automatic shimming routines were employed to maximize B_o homogeneity before acquiring MRSI data. The water suppression was varied and will be discussed in detail in Chapter 3.

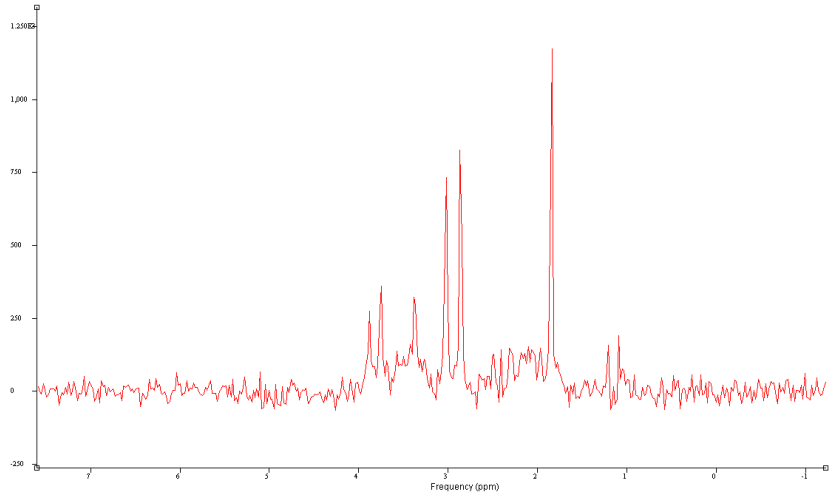

Figure 2.15 Water suppressed MRS spectrum (after removal of residual water using HLSVD) acquired using a room temperature phantom containing various metabolites at physiological concentration using a short echo time *TE=35ms* at 1.5T.

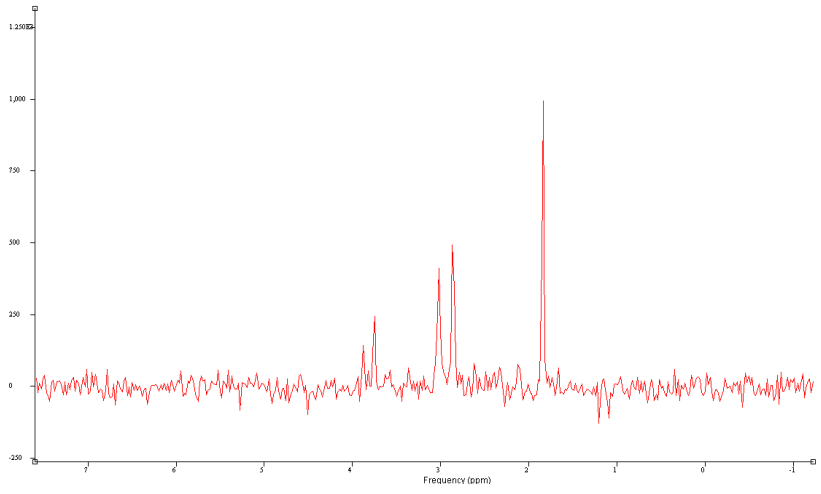

Figure 2.16 Water suppressed MRS spectrum acquired using a room temperature phantom containing various metabolites at physiological concentration using a long echo time *TE=145ms* at 1.5T.

Sequence	MRSI (2D-PRESS)
Orientation	AXIAL
TE/TR(ms)	145/1000
Bandwidth (Hz)	1000 (spectral width)
Number of samples	512
FOV (mm)	240-320
Slice thickness (mm)	10
Matrix	24X24
No. Slices	1
Sat bands	4 -A,P,R,L
Scan time	09 minutes 40 seconds

Table 2.5 MRSI acquisition parameters.

2.5.2 MRSI data processing

While the temperature estimation using equation 2.7 is reasonably simple, a number of post processing steps have to be applied before the frequency of the metabolites and water peak can be estimated. The post processing of the MRSI data has been widely discussed in the literature. An interested reader is referred to the manuscript by Jiru (56) and references within for an overview of the principles of the post processing techniques. A detailed description of the technicalities can be obtained from articles by Young and Soher et al. (57-59).

In routine MRSI, processing consists of the three stages namely pre-processing, metabolite estimation (or commonly known as spectral fitting) and display. A processing protocol based on these steps was developed by Prof Ian Marshall for the purpose of quality assurance at this institution and can be readily employed for temperature estimation using MRS; this is described as below.

2.5.2.1 Pre-processing

As the name suggests a number of processing steps are applied to the raw data obtained after a PRESS excitation before the spectrum fitting packages can be employed to compute frequency of the metabolites and water peaks. The first stage is generally reading the raw data from the manufacturer specific data files. These files generally consist of a header, containing the details of the acquisition protocol, followed by frame by frame (or the k-space) of the MRSI data. After reading the k-space data from the raw data files it is necessary to determine if zero padding needs to be applied. Zero padding is applied to the k-space of the MRSI data to make the file matrix size (N) a multiple of 2^N so that Fast Fourier transforms can be applied. Thus when the MRSI matrix is 24 (or 24*24 phase encodes are used), zero padding is applied to edges to final matrix size N=32 which is equal to 2^5. No zero padding is necessary if 16*16 phase encodes if are used. The final

matrix size also determines the effective voxels size. A mild cosine apodization is then applied to reduce the influence of voxel bleeding as discussed in section 2.2. A 2D Fourier transform is then used to produce a series of FIDs in the image space. The spectrum phasing is then achieved by self referencing of the spectrum, in this approach the spectrum phasing is achieved by hard phasing (or self referencing) the phase of the largest signal (generally water or residual water peak) to zero. The self-reference approach is a modification of the well documented phase correction using reference acquisition as proposed by Ordidge et al. (60). A detailed explanation can be obtained in the article by Johnson et al. (61). It should be noted that this self reference phase correction makes the spectra symmetrical (about the water peak). The FIDs are then scaled based on the RF transmit and receive gain settings and the voxel size. This scaling normalizes the FIDs and allows direct comparison of MRSI data acquired during different sessions. Finally a series of the FIDs are outputted in a text file which can then be read into the spectral fitting package jMRUI to compute $\Delta_{water\text{-}reference}$ on a voxel by voxel basis. The pre-processing is achieved using a utility written in C originally written by Professor Ian Marshall but modified by the author.

2.5.2.2 Spectral fitting

Once the pre-processing is complete, spectral fitting can be performed using the jMRUI (version 3) software package (62). A time domain spectral fitting algorithm, AMARES as described by Vanhamme et al. (63) was employed to estimate frequency, amplitude and line width of the metabolites and water peak on a voxel by voxel basis. Firstly the data are loaded in jMRUI and quantification of the water (or residual water) peak is performed by loading appropriate prior knowledge files as shown in Figure 2.17, and the results are then saved in a text file.

Even when water suppression is employed, the water suppression factors are adjusted to retain a proportion of water (~10%) so as to measure both the frequency of the water and internal reference (metabolite) for the same spectrum. Thus it is necessary to employ software based filter to remove the

residual water peak to visualize the metabolites signal. A software filter 'Hanckel-Lanczos Singular Value Decomposition (HLSVD)', integrated in the software package jMRUI, was used to filter the water (or the residual water) peak as shown into Figure 2.18. The spectra after the removal of water or the residual water peak are shown in Figure 2.19; the metabolite peaks can be easily visualised now. A different set of prior knowledge files is then loaded as shown in Figure 2.19 and AMARES is employed to estimate the metabolites frequency, amplitude, amplitude-SD and linewidths of the three metabolites (NAA, Creatine and Choline). The results of the AMARES quantification are then stored in a text file. It should be noted that as the spectrum is self referenced the water peak always appear at 4.7ppm and the resulting temperature changes are evident by variation of the NAA frequency. Thus it is only necessary to estimate NAA frequency to estimate temperature using equation 2.7

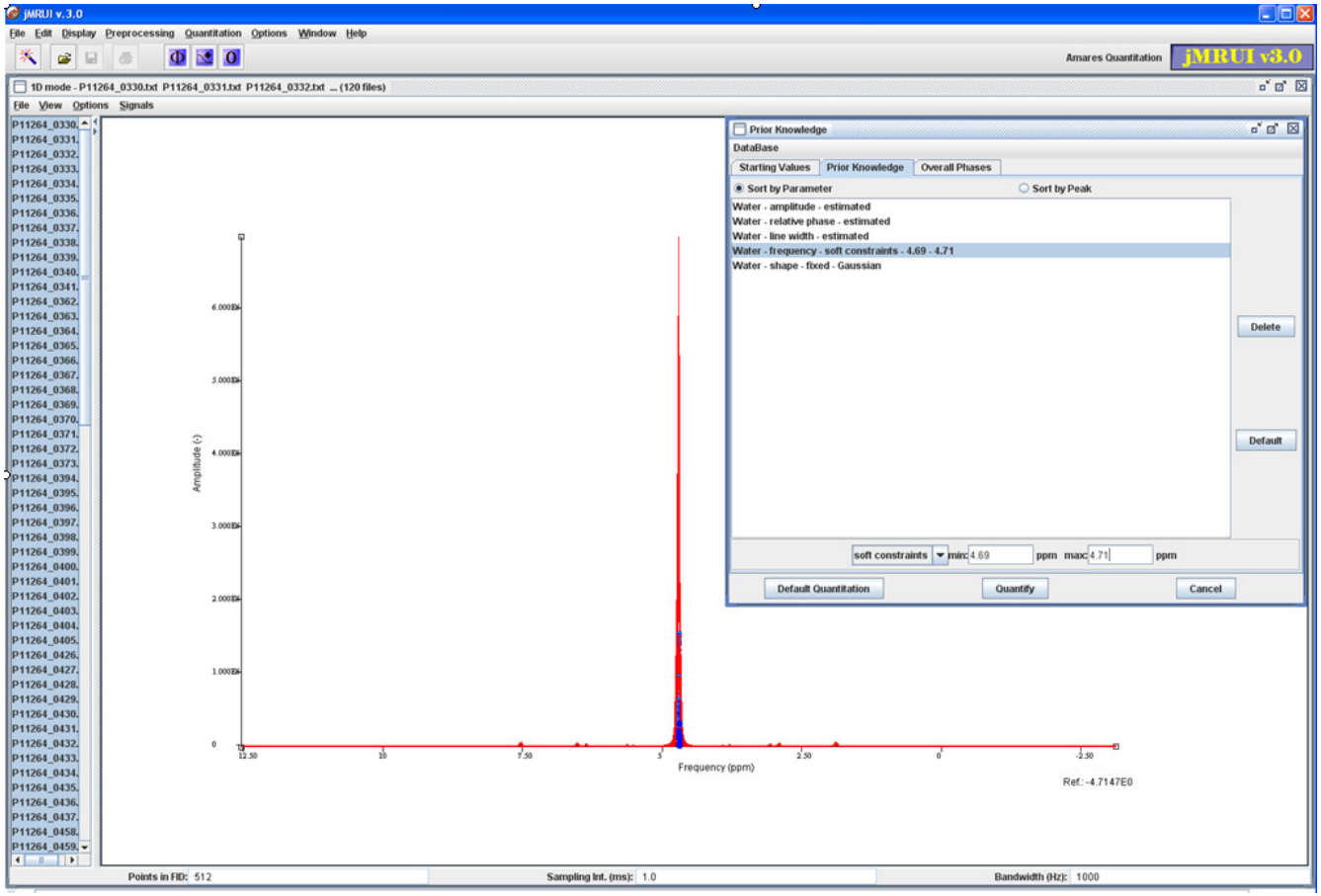

Figure 2.17 jMRUI interface with the MRSI spectra loaded. The residual water peak is quantified first by loading the prior knowledge file as shown in the insert. The MRSI data was acquired from a homogeneous room temperature phantom with the protocol described in section 2.5.2

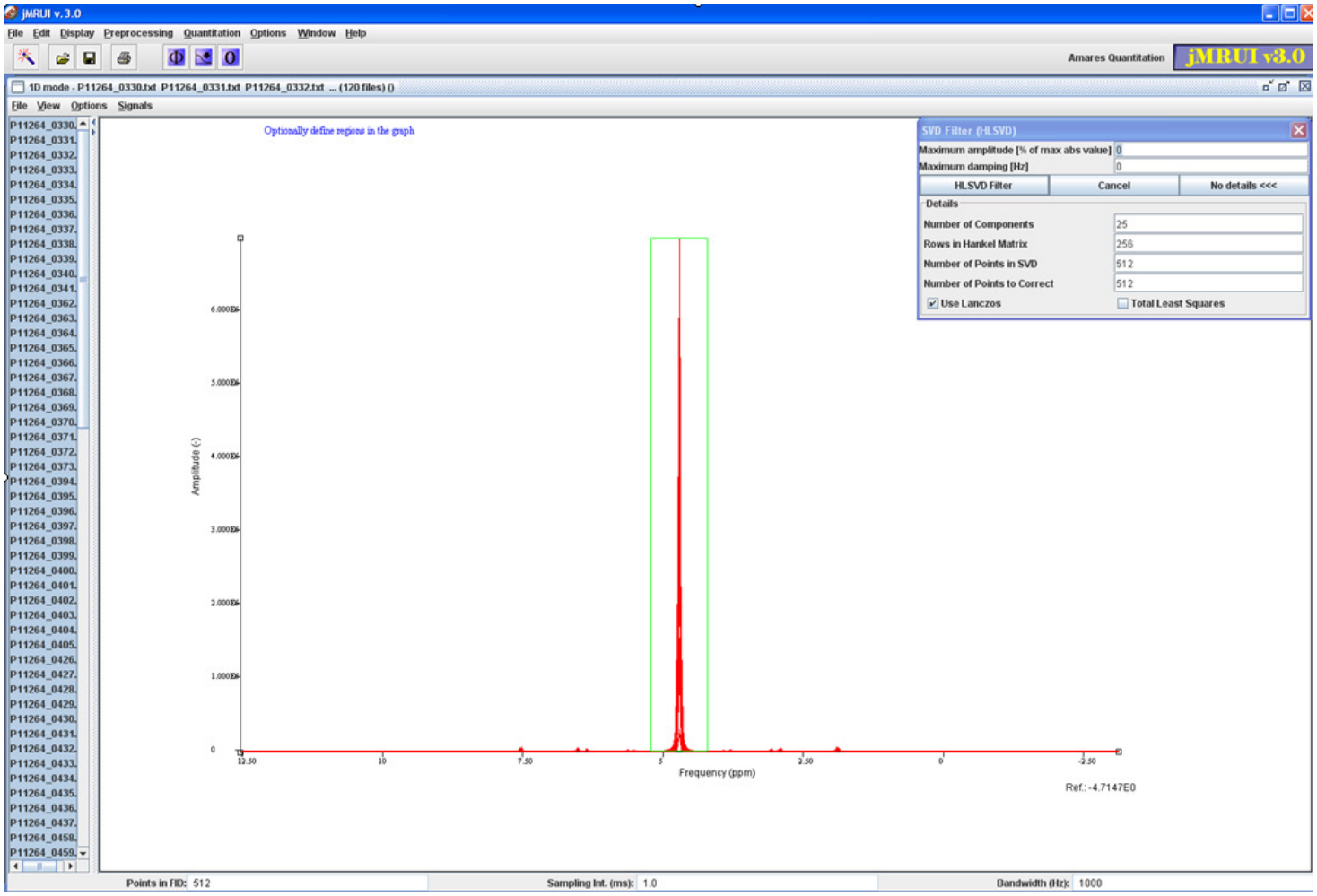

Figure 2.18 jMRUI interfacing showing removal of the residual water peak using HLSVD filter. The filter parameters are shown in the insert.

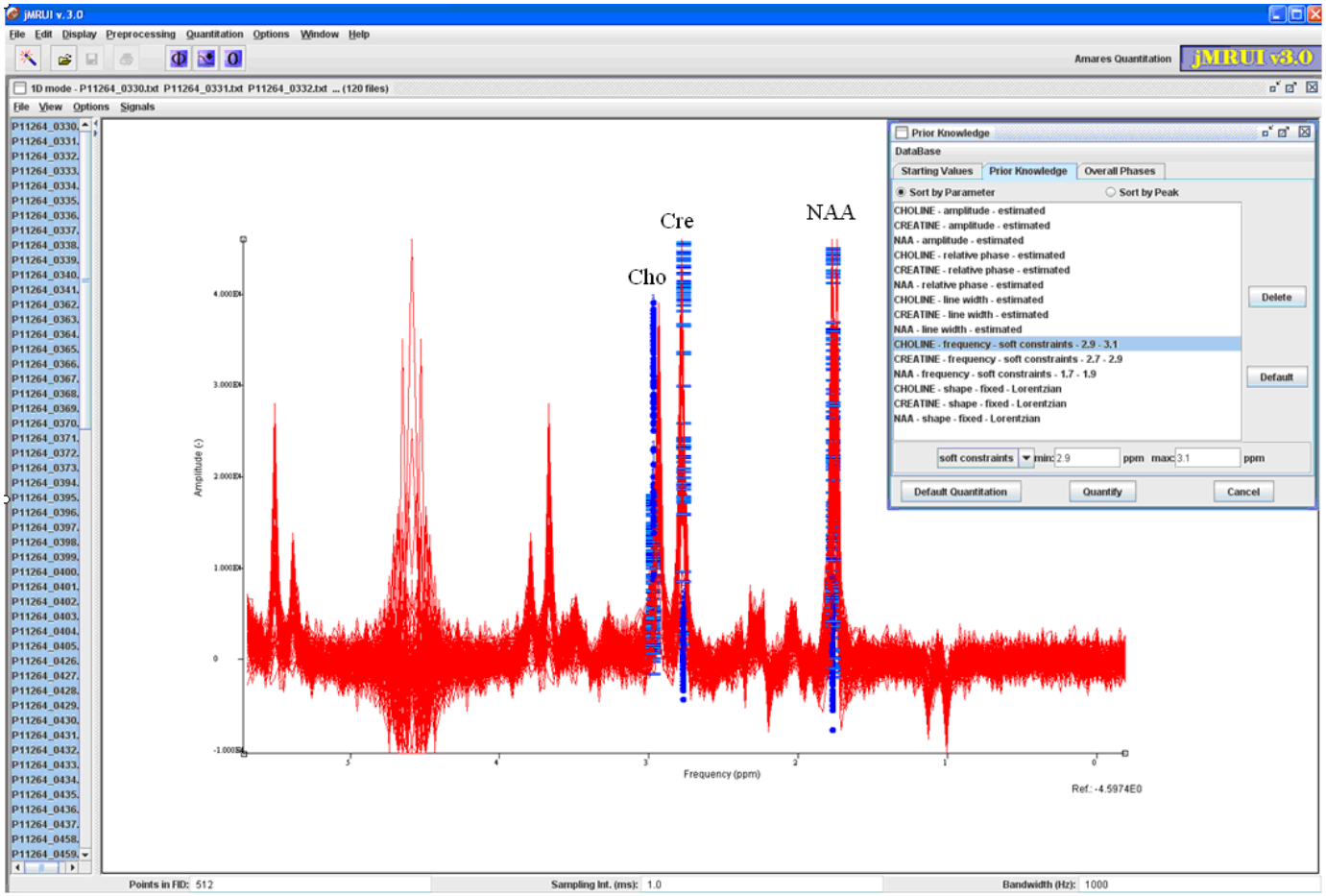

Figure 2.19 jMRUI interface showing the spectra after removal of the residual water peak using the HLSVD filter. The metabolite peaks (Cho, Cre and NAA) can be identified. The prior knowledge file used to estimate the frequencies amplitudes and linewidths of the metabolite peaks using AMARES are shown in the insert.

2.5.2.3 Display

Once the results of spectral fitting are available, two MATLAB scripts ('display_MRSI_raw.m' and 'display_MRSI_results.m') originally written by Prof Ian Marshall but modified by the author are used to display spectra on a voxel by voxel basis and to generate temperature and metabolite maps. The MATLAB script 'display_MRSI_raw.m' is used to display the raw spectra obtained after pre-processing from each MRSI data set on a voxel by voxel basis as shown in Figure 2.20. 'Display_MRSI_results.m' reads the result file of AMARES fitting and builds and displays the model spectrum from the estimated fitting parameters as shown in Figures 2.21. In-addition using 'display_MRSI_results.m' the frequency of the metabolite internal reference (NAA) is used to estimate temperature on the voxel by voxel by using equation 2.7. Metabolite and temperature maps are recorded for future reference as shown in Figure 2.22. An Excel sheet, which summaries the metabolite and temperature estimates, is stored for recording purposes.

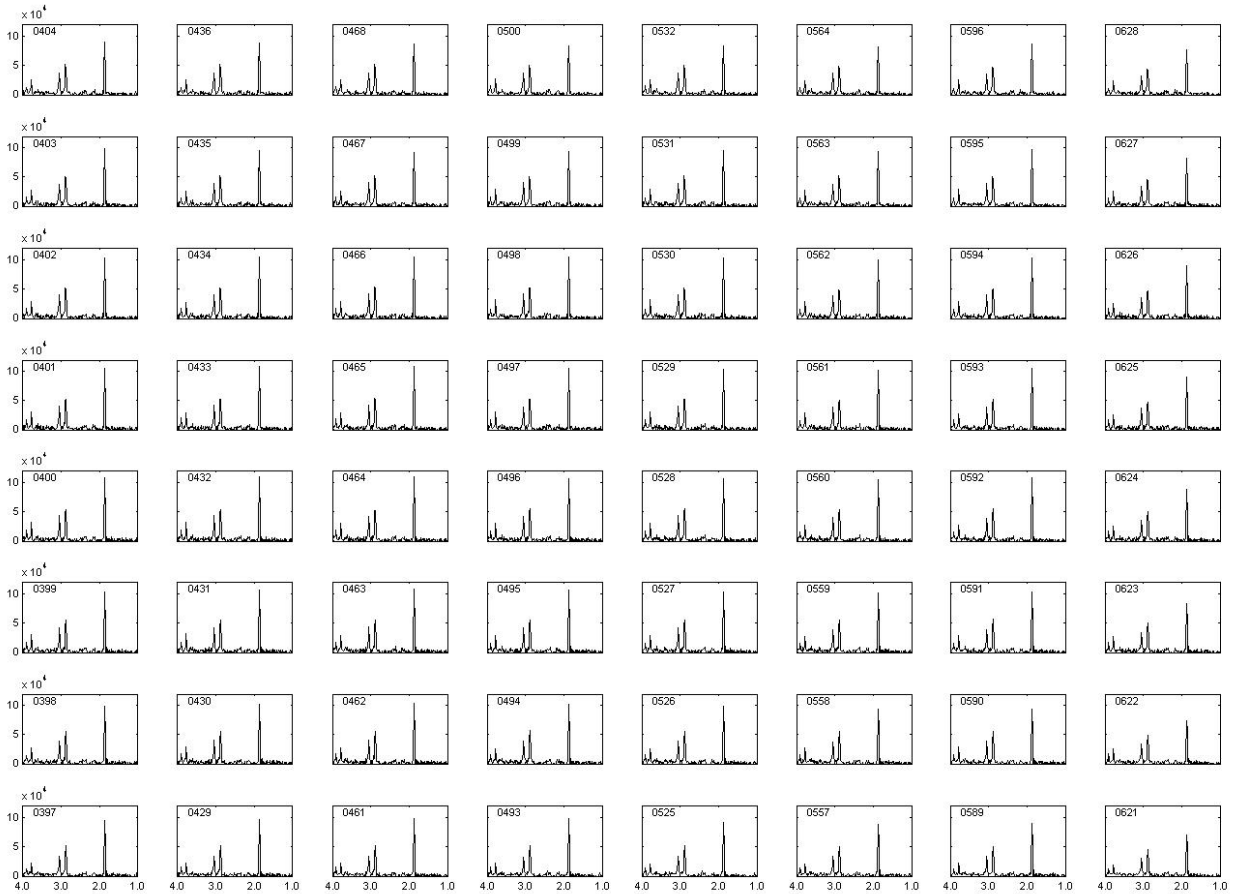

Figure 2.20 The central (8*8) voxels showing the raw MRSI spectra obtained after pre-processing, plotted using display_MRSI_raw.m. The MRSI dataset was acquired using the protocol discussed in section 2.5.1. This display provides a quick snap shot of the raw MRSI spectra and facilitates visual quality assessment by comparing the raw spectra with the modelled spectra obtained after spectral parameter estimation (as shown in Figure 2.21).

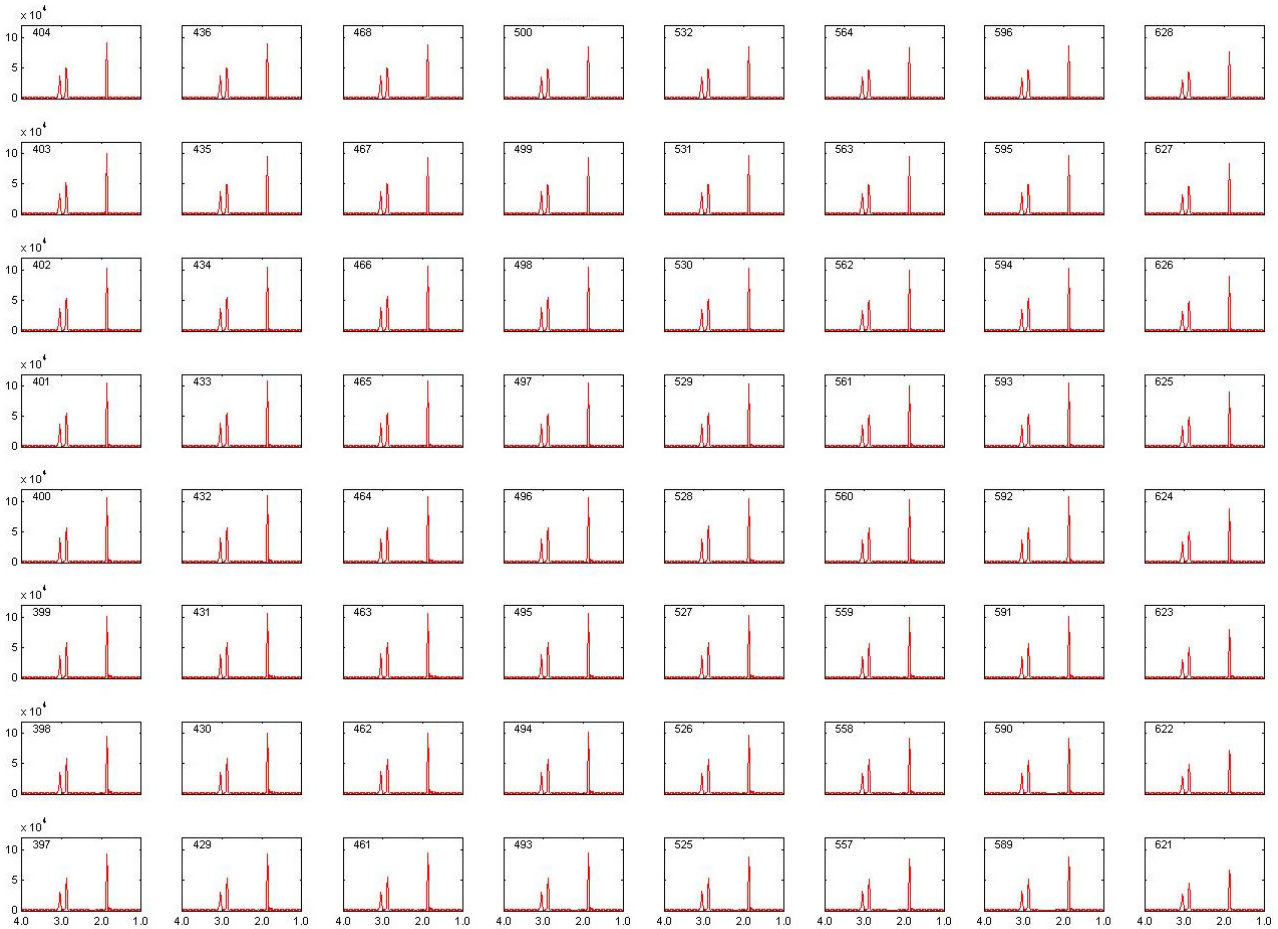

Figure 2.21 Modelled spectra generated from AMARES spectral fitting estimates (plotted using display_MRSI_results.m), to facilitate visual spectral quality assessment by comparing the estimated spectra with the raw spectra (as shown in Figure 2.20). Central 8*8 voxels are shown.

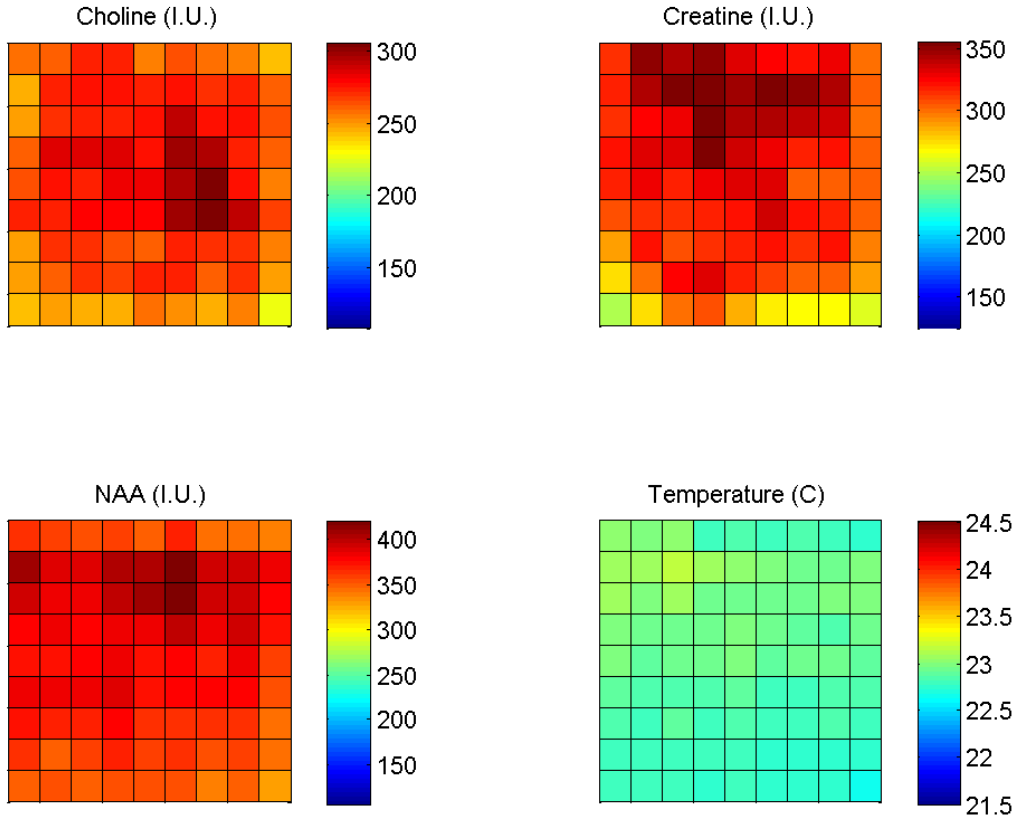

Figure 2.22 Metabolite (Cho, Cr and NAA) amplitude and temperature maps obtained after processing of MRSI phantom data using display_csi_results.m.

2.6 Summary

In this chapter the basic concepts of MR Physics and MR spectroscopy were presented. The temperature sensitivity of the proton frequency to measure absolute brain temperature was discussed and a number of studies which have employed internal reference MRS to measure brain temperature were summarised. It was seen brain temperature maps can be obtained non-invasively using MRSI and thus MRSI temperature mapping can be particularly used in study of the thermoregulation of the brain.

However MRSI is technically demanding and factors such as water suppression, chemical shift misregistration influence MRSI acquisition. Thus it is crucial to assess whether these factors introduce errors in brain temperature mapping. Therefore comprehensive validation of the MRSI temperature mapping will be performed. In the following chapter (chapter 3) uniform temperature maps acquired using a room temperature phantom will be employed to assess, how water suppression and chemical shift mis-registration influence brain temperature mapping.

3 Reduction of systematic error in MRSI based Temperature Mapping

3.1 Introduction

Single voxel MRS has been widely used to measure brain temperature at specific locations as discussed in section 2.4 and to identify brain temperature variations. Large coverage offered by MRSI makes it an attractive option for temperature mapping to study regional brain temperature variations. Compared to singe voxel MRS spectra, the signal to noise ratio (SNR) for metabolite peak is lower for MRSI spectra due to smaller voxel size and metabolite linewidths are broader for MRSI as it is challenging to shim a large volume of interest (VOI). As a result it is argued that the precision of MRSI temperature mapping is poor compared to single voxel (SVS) internal reference MRS (46). Chemical shift misregistration as discussed in section 2.3 is another potential source of the error in MRS (single and multi voxel) thermometry, as B_o inhomogeneity across the VOI has the potential to affect chemical shift separation. In MRSI, the B_o field inhomogeneity encountered over the larger VOI affects frequency selective water suppression (CHESS) and may introduce systematic errors in temperature mapping. Unlike SVS it's not always possible to collect a non water suppressed reference using MRSI, as it doubles the acquisition time. Thus it is necessary to established whether systematic errors exist in water suppressed (WS) MRSI based temperature maps.

In this chapter, a systematic error identified in temperature maps acquired using WS-MRSI data from a homogenous room temperature phantom using different scanners is presented in section 3.2. The effect of varying MRSI data processing and WS parameters on this systematic error is investigated in sections 3.3 and 3.4 respectively. It will be shown that the systematic error can be reduced by changing water suppression settings. In section 3.5 with the help of optical thermometry these results will be validated and in section 3.6, it will be assessed whether the systematic error exists in temperature maps estimated from in-vivo MRSI data.

3.2 Systematic error in temperature maps

3.2.1 Introduction

WS-MRSI data are collected at the Brain Research Imaging Centre, University of Edinburgh on monthly basis from a uniform room temperature phantom. These MRSI data sets were processed to produce temperature maps and to assess if systematic error is present in the temperature maps.

3.2.2 Methods

WS-MRSI data were acquired using a GE 1.5T SIGNA scanner (GE Healthcare Slough UK) and manufacture provided homogeneous spectroscopy phantom ('BRAINO') as a part of quality assurance routine at Brain Research Imaging Centre, Edinburgh, UK. The phantom consists of the brain metabolites at physiological concentration as shown in Table 3.1. The phantom was kept in the scan room at all times to ensure thermal equilibrium and its temperature was determined using a liquid crystal display (LCD) thermometer strip (accuracy of $1^{o}C$) attached to the phantom. The manufacturers' quadrature head coil and two dimensional MRSI pulse sequence (PRESS-CSI) were employed to acquire MRSI scans. The acquisition protocol was similar to that described in section 2.5.1 and the main acquisition parameters are listed in Table 3.2. Automatic shimming and default CHESS based water suppression were employed. The CHESS based WS was achieved by employing three frequency selective fixed bandwidth (BW, default value: 75Hz) sinc-shaped RF pulses each followed by a crusher gradient (one for each direction x/y/z).

MRSI data were processed as described in section 2.5.2. The mean and the standard deviation of the metabolites (NAA) and temperature estimates were computed for the central area of the VOI that included the central 80 voxels. As a quality assurance measure all the spectra with NAA linewidths greater than 10 Hz were excluded from the analysis. The temperature maps were normalized by subtracting the temperature of the central voxel for each session for display purposes.

Chemical name	Concentration (mM)
Potassium phosphate monobasic	50
Sodium hydroxide	56
N-acetyl-aspartic acid	12.5
Creatine Hydrate	10
Choline Choride	3
Myo-inositol	7.5
L-Glutamic acid (monosodium salt)	12.5
DL-lactic acid (lithium salt)	5
Sodium azide	0.10% (w/v)
Magnevist	0.10% (w/v)

Table 3.1 Contents of the GE MRS (BRAINO) phantom as listed in GE spectroscopy manual, version 2001.

WS-MRSI data were also acquired from different scanners; these include a GE 1.5T and GE 3T scanners installed at the Institute of Neurological Sciences, University of Glasgow, Glasgow, UK and a Siemens Verio 3T scanner, installed at the Clinical Research Imaging Centre, University of Edinburgh, Edinburgh, UK, respectively. The MRSI pulse sequence used was similar to that discussed previously for the two GE scanners, while the scan from the Siemens 3T scanner was acquired using a manufacturer provided version of the semi-LASER pulse sequence as described by Scheenen et al. (64). Manufacturer provided second order shimming was used while acquiring data from the 3T scanners.

Sequence	MRSI (2D-PRESS)
Orientation	AXIAL
TE/TR(ms)	145/1000
Bandwidth (Hz)	1000 (spectral width)
Number of samples	512
FOV (mm)	320
Slice thickness (mm)	10
Matrix size	24X24 interpolated to 32*32
No. Slices	1
Voxel Volume (cm^3)	1.00 (post processing)
Scan time	09 minutes 40 seconds

Table 3.2 Acquisition protocol for MRSI quality assurance at the Brain Research Imaging Centre, University of Edinburgh.

3.2.3 Results

Temperature maps estimated using the water suppressed MRSI data from a homogeneous room temperature phantom from different sessions using a GE 1.5T are shown in Figure 3.1. It is seen that the temperature maps are not uniform and a systematic temperature gradient of about 0.5^0C exists along the anterior-posterior dimension. The systematic error persists for several months as shown in Figure 3.1. The mean and SD of the temperature maps are reported in Table 3.3. A similar temperature gradient of about 0.4^0C was observed in the temperature map acquired using another GE 1.5T scanner with similar set up as shown in Figure 3.2. The appearance of the systematic errors changed when 3T scanners were employed. The temperature maps acquired using the GE 3T was not uniform although a linear temperature gradient as seen in Figure 3.2 could not be identified. The temperature map estimated from MRSI data acquired using the Siemens 3T scanner appears to be uniform within 0.1^0C as shown in Figure 3.2.

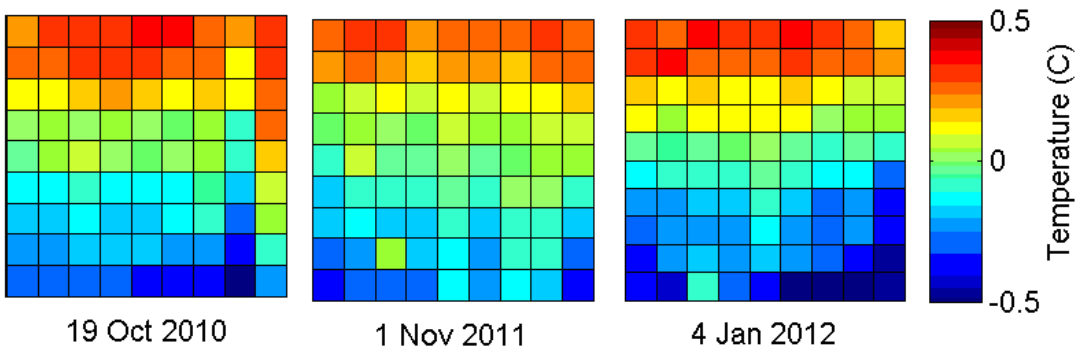

Figure 3.1 Normalized temperature maps computed using MRSI data acquired on a homogenous room temperature phantom acquired using strong WS (WS factor 90) on different sessions on a GE 1.5T scanner. A systematic temperature gradient of about 0.5^0C is observed along the (Anterior-Posterior axis) in the temperature maps (also see Table 3.3)

Date	19oct2010	1Nov2011	4jan2012
T_{mean} (^{0}C)	20.3	22.6	21.93
T_{SD} (^{0}C)	0.27	0.18	0.20
$T_{phantom}$ (^{0}C)	20	22	22

Table 3.3 Mean and SD of temperature estimates for the temperature maps shown in Figure 3.1. Also reported is the phantom temperature ($T_{phantom}$) measured using the LCD thermal strip.

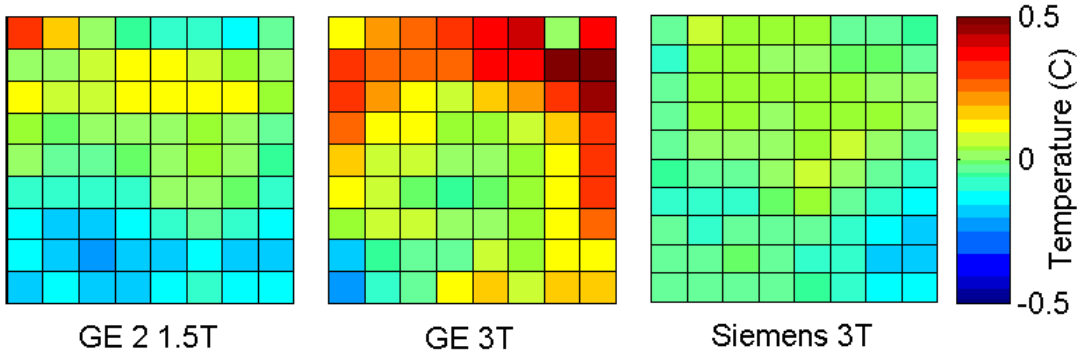

Figure 3.2 Normalized temperature maps computed using WS-MRSI data acquired on a homogenous room temperature using different scanners. The temperature maps were acquired using manufacture provided sequence with default (strong) water suppression.

3.2.4 Discussion

A systematic error was identified in the temperature maps estimated using the water suppressed MRSI data acquired from a homogenous room temperature phantom using a 1.5T GE scanner (see Figure 3.1). The systematic error is persistent over many months. The appearance of the systematic error varies between different scanners (see Figure 3.2). Temperature maps acquired using the 3T Siemens scanner exhibited the smallest temperature variation. In addition to second order shimming, this scanner employs WET based water suppression and adiabatic RF pulses for localisation. The WET based water suppression employs 4 CHESS pulses with variable flip angles to produce uniform water suppression in presence of B_o inhomogeneity (65) and adiabatic pulses are reported to reduced error due to chemical shift misregistration and RF inhomogeneity (64). Thus water suppression and chemical shift mis-registration, as previously argued are the likely causes of the systematic error in the temperature map. In the following sections it will be assessed if this systematic error can be reduced and whether this (of ~0.5^0C) error can be identified in temperature maps estimated from in-vivo MRSI data.

3.3 Chemical Shift misregistration

3.3.1 Introduction

Spatial origins of the water and internal reference metabolite signals are different due to chemical shift misregistration (see section 2.4.4). The B_o variations across water and metabolites slices may influence estimation of the frequency difference between water and metabolite internal reference, and thus may affect MRS temperature estimates. However it is not clear whether and to what extent chemical shift mis-registration affects MRSI temperature mapping. The misregistration between water and different metabolites signals depends on their chemical shift difference; as a result the slice offset (in MRSI) between water and different metabolites (Cho, Cre and NAA) due to chemical shift mis-registration is different. Thus use of different metabolites as internal reference to assess effect of chemical shift mis-registration on MRSI temperature mapping was investigated and is presented in this section.

3.3.2 Methods

MRSI data acquired as part of the quality assurance protocol as discussed in the previous section can readily be employed to assess the effect of chemical shift misregistration. The MRSI data was processed in the standard manner as previously discussed in section 2.5.2. However, temperature maps were computed using different metabolites (Cho, Cre and NAA) as internal references; equation 2.7 was used to obtain temperature maps using NAA as the internal reference as discussed in section 2.4.2, while equations 3.1 and 3.2 were used to obtain temperature estimates using choline and creatine as the internal references. Equations 3.1 and 3.2 were obtained using the nominal chemical shift difference of 1.028 ppm between NAA and Creatine and 1.1850 ppm between NAA and Choline as reported by Govindaraju et al. (21).

$$T_{cho}=37+100(CS_{cho}-0.85) \quad (3.1)$$

$$T_{cre}=37+100(CS_{cre}-1.007) \quad (3.2)$$

3.3.3 Results

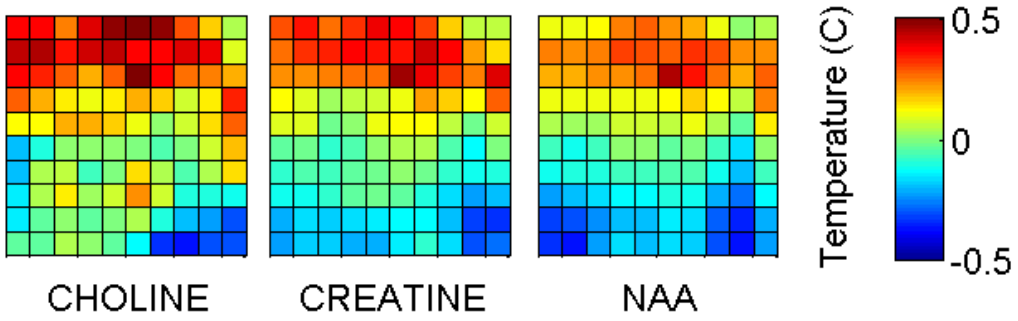

Figure 3.3 Normalized Temperature maps computed using various metabolites as reference using MRSI data acquired with default water suppression settings; for Mean (SD) of temperature estimates see Table 3.4.

Metabolite	Temperature (°C)	Amplitude (I.U.)	Linewidths (Hz)
Choline	22.01 (0.20)	199.3 (31.9)	2.99 (0.26)
Creatine	21.70 (0.19)	231.2 (34.5)	2.07 (0.24)
NAA	21.94 (0.21)	287.9 (34.7)	1.37 (0.2)

Table 3.4 Mean (SD) of the temperature and amplitude estimates for various metabolites used as internal references (also see Figure 3.3).

The temperature maps computed using various metabolites as internal reference are shown in Figure 3.3. The mean and the standard deviation of the temperature estimates, metabolite amplitudes and linewidths are reported in Table 3.4. It is seen that the absolute temperature estimates obtained using different internal references were similar. The MRSI data was acquired using the default water suppression settings, thus a similar systematic gradient in temperature maps is observed for all 3 metabolites used as internal reference. A minor increase in variance of the amplitude and linewidths estimate of choline and creatine were observed as reported in Table 3.4.

3.3.4 Discussion

The chemical shift misregistration on the GE 1.5T scanner with maximum gradient strength of 6mT/m (employed in this study) will result in slice offset of 0.7mm between NAA and water, assuming a 10mm slice thickness (44). The slice offset between water and Cho and water and Cre will be even smaller. The similar temperature maps obtained using different metabolites as internal reference suggest that this small slice offset between water and metabolites has little effect on temperature mapping. Chemical shift mis-registration is also reported to have no effect on estimation of frequency difference at 3T in-vivo (66). As a result chemical shift misregistration appears to have little or no influence on MRSI based temperature mapping.

3.4 Water suppression

3.4.1 Introduction

Temperature maps estimated using WS-MRSI data acquired using a homogenous room temperature phantom, exhibit a systematic error (Figure 3.1). The systematic error was similar (~0.5^0C) when different metabolites were employed as internal reference to compute frequency difference (Δ) and to estimate temperature. These results indicated that the systematic error in temperature maps is likely to be a result of a systematic variation in the frequency of residual water peak across the VOI rather than that of the 3 metabolite peaks employed as internal reference.

For effective water suppression (using CHESS) it is crucial that the CHESS pulses are applied on resonance to water frequency (see section 2.4.5 for details). It is difficult to shim a larger VOI encountered in MRSI, thus the B_o inhomogeneity exists across the VOI. As a result the water frequency systematically varies across the VOI and CHESS pulses may not to be applied on resonance. This may systematically influence the frequency of the residual water peak and induce systematic errors in MRSI temperature maps. Thus in order to assess the effect of water suppression on systematic error in temperature maps, the effect of varying different parameters for CHESS based water suppression was examined. In addition MRSI data were acquired with water suppression and without water suppression were compared for temperature mapping. These results will be discussed in this section.

3.4.2 Methods

A series of MRSI data were acquired and processed using the protocol as described in section 3.2.2. The bandwidth of RF pulses (BW) used for CHESS and the delay (τ) between the end of the CHESS pulses and start of PRESS localisation were changed from the default values of 75 Hz and 48 ms respectively for consecutive scans in the order as described in Table 3.5. MRSI data were processed using the standard processing as discussed in section 2.5.2. The CHESS based water suppression was switched ON and OFF using the research options (CVs) 'SUPPRESS' (default value=1, CHESS ON) and 'SUPP' (default value=1 CHESS ON). Consistent prescan set up and

shim values were used for all MRSI scans. Where required the water suppression factors were determined on a voxel by voxel basis, by computing the ratio between the amplitude of the water peak (measured from the non water suppressed reference scan) and the amplitude of the residual water peak (measured from the water suppressed scan).

3.4.3 Results

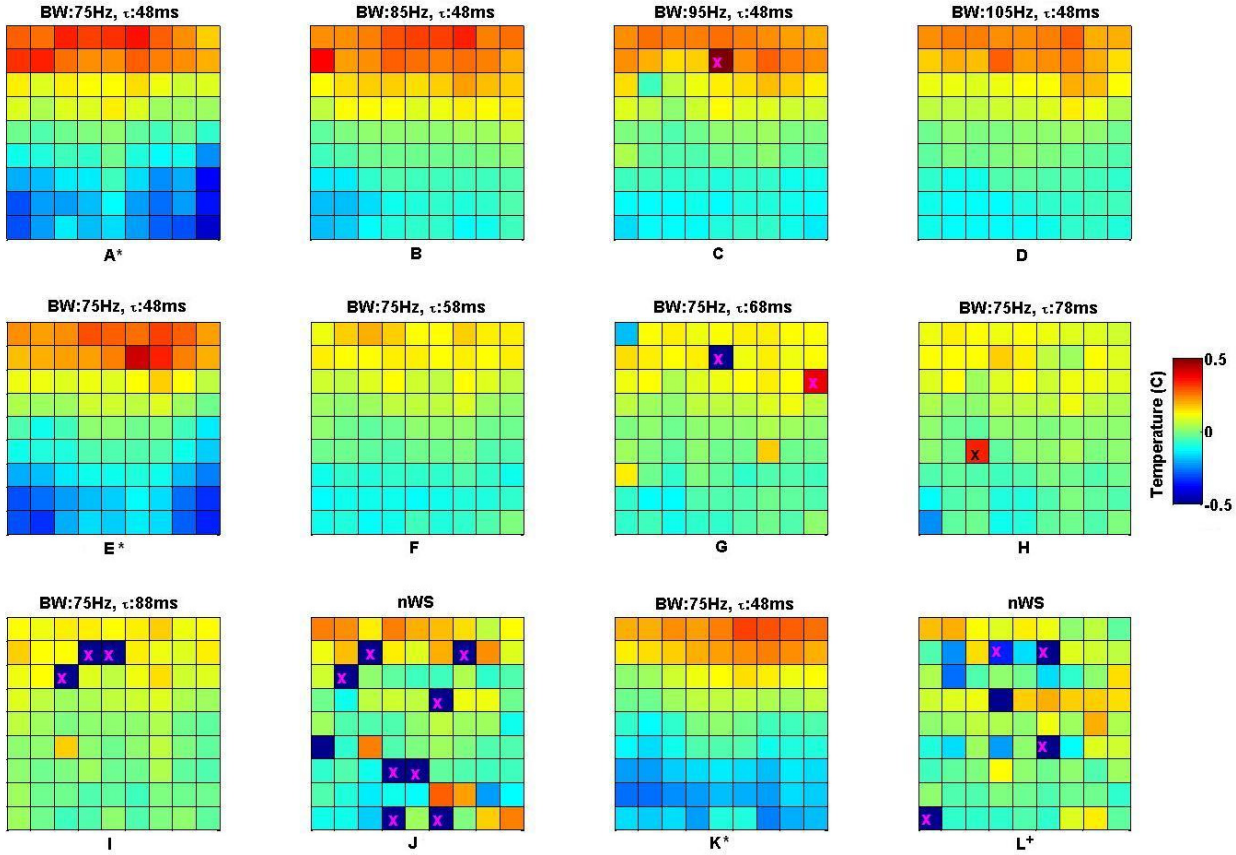

Figure 3.4 Normalized temperature maps acquired from a uniform room temperature phantom at different water suppression settings. "*" indicates temperature maps acquired with strong water suppression i.e. default settings τ=48ms and BW=75Hz. "+" indicates temperature maps acquired using no WS and used as reference to compute WS factors. "x" indicates voxels rejected from the analysis (as the NAA linewidth>10 Hz). Also see Table 3.5.

WS parameter			Temperature (^{o}C)		WS factor	
scan#	τ (ms)	BW (Hz)	Mean	SD	Mean	%COV
1	48*	**75**	21.93	**0.2**	84.7	5.25
2	48	**85**	22.07	0.14	51.1	3.46
3	48	**95**	22.15	0.14	38.5	3.91
4	48	**105**	22.24	0.13	32.7	3.88
5	**48***	75	22.24	**0.18**	88.6	4.57
6	**58**	75	22.36	0.09	24.6	1.19
7	**68**	75	22.42	0.09	14.5	1.25
8	**78**	75	22.51	0.08	10.3	1.04
9	**88**	75	22.61	1.01	8.1	0.94
10	n-WS	75	22.91	1.07	1	0.41
11	48*	75	22.67	**0.17**	88.3	6.89
12	n-WS	75	22.72	1.03	+	+

Table 3.5 Mean and SD of temperature estimates and WS factors for temperature maps reported in Figure 3.4. "*" indicates temperature maps acquired with strong water suppression i.e. default setting τ=48ms and BW=75Hz. "+" indicates temperature maps acquired using no WS and used as reference to compute WS factors.

The temperature maps acquired at different WS settings are shown in Figure 3.4 and the mean (T_{mean}) and standard deviation (T_{sd}) of the temperature estimates across the VOI are reported in Table 3.5. Examples of MRSI spectra, before and after removal of the water (or residual water) peak are shown in the Figures 3.5 and 3.6. When no water suppression is employed, a large proportion of voxels were rejected; although a temperature gradient was not apparent in the non water suppressed scan, the distribution of temperatures increases and inspection of the data revealed increased measurement uncertainty in the frequency estimates generated by AMARES. With increased τ there was an apparent reduction in the anterior-posterior temperature gradient (less than 0.1^{0}C at τ = 68 ms) and the measured water suppression factor was reduced.

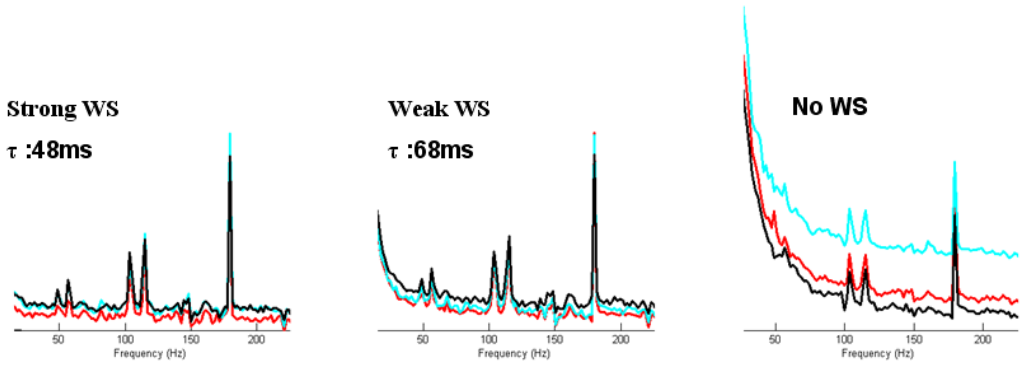

Figure 3.5 Selection of MRSI spectra from different locations of the VOI at three levels of water suppression without filtering the water peak using HLSVD, as seen the metabolites can be visualised at either level of water suppression. It is observed that the non WS suppressed spectra may exhibit significant baseline distortion.

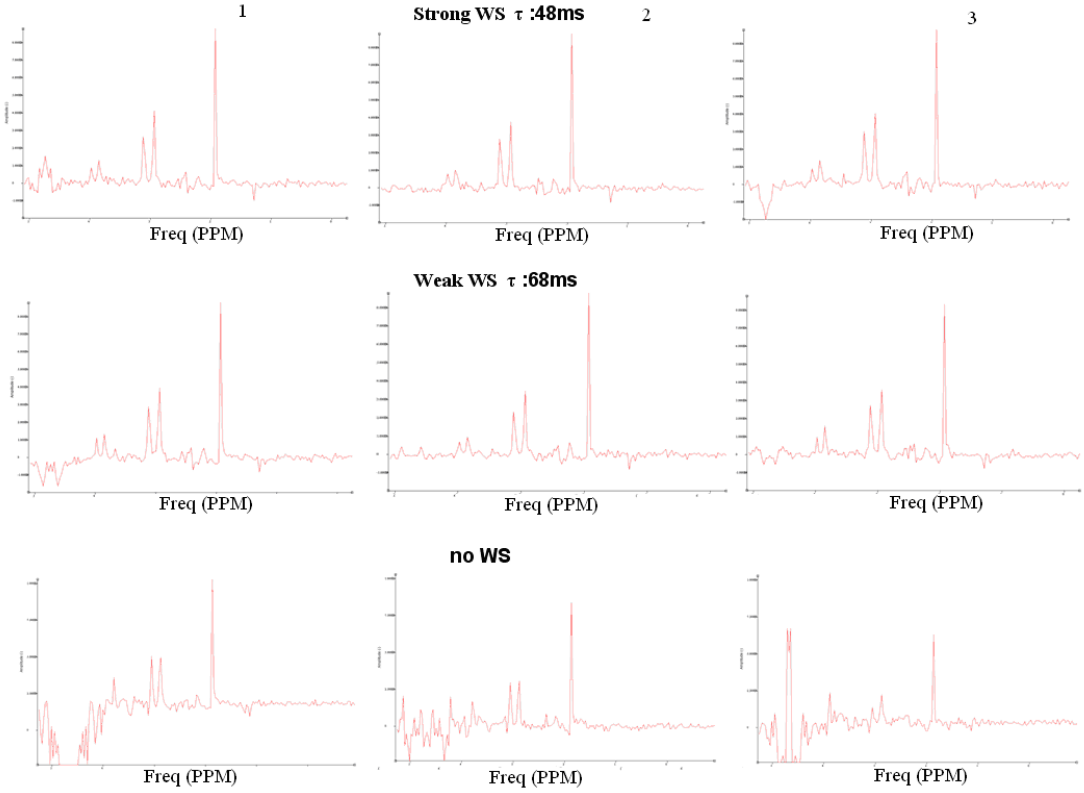

Figure 3.6 The same spectra as shown in Figure 3.5 (shown separately i.e. one spectrum per column), but the after removal of the water peak using HLSVD using jMRUI. It is evident that spectra acquired with water suppression are of better quality.

The amplitude of the residual water peak changes as BW or τ is varied, however the coefficient of variation (COV) in amplitude of the water (or residual water) peak did not change and was constant at ~27% for all the scans. The COV of the WS suppression factors however decreases on increasing the BW or the delay τ as shown in Table 3.5

The temperature maps at successive scans were always warmer and the mean temperature always increases irrespective of the order of the acquisition as reported in Table 3.5. This indicates RF related heating of the phantom during the scan. The variation of the B_o field across the VOI was assessed by the computing variation in frequency of the water peak for non WS scans (i.e. scans 10 and 12). The frequency of the water peak for non WS scans varied between 0-5Hz across the VOI and 0-2Hz across the central column of voxels in the A-P direction.

3.4.4 Discussion

Water suppression techniques were introduced to avoid the problem of limited digital resolution for analogue to digital conversions of signals with a large dynamic range. The modern day A/D converters have sufficiently large range to allow metabolite detection from the same spectrum which contains a large water signal and this permits the acquisition of non water suppressed MRS data. The large water peak can be used for spectrum phasing, B_o estimation, estimation of sensitivities for multi-coil elements (30) and to estimate the frequency difference (Δ) to estimate temperature. However, the main problem that limits the use of non water suppressed MRSI is the broad tails of the water peak and the sideband artefacts, which cause baseline distortions and inhibit accurate quantification of the metabolite signals (67;68). A number of approaches have been suggested to ameliorate this problem, but elimination cannot be guaranteed (31;67;69;70). As a result the temperature maps estimated using non WS MRSI data are not uniform as shown in Figure 3.4. Child et al. (46) report similar findings and recommend use of partial WS for MRS thermometry to avoid problems with a large baseline. Thus it is important to suppress the water peak to acquire good quality MRSI data for temperature mapping.

Frequency selective (CHESS) WS is routinely employed in MRSI for accurate quantification of the milli-molar metabolite signals. For effective WS using CHESS it is essential to have minimum B_o variation across the VOI (34). In this study using automated shimming the B_o variation was reduced to 0-2 Hz

across the central region of the VOI. As a result the water (or Larmor) frequency varies slightly across the VOI and relatively large bandwidth (75Hz) RF pulses used for CHESS will be applied at off resonance. The temperature maps estimated using MRSI data acquired with default strong water suppression (τ=48ms and WS factor 90) exhibit the strongest apparent temperature gradient of about 0.5^0C, the appearance of the systematic error varied as the water suppression parameters were varied (Figure 3.4). By increasing the recovery delay to τ=68ms, the amplitude of the residual water signal increased and the observed systematic error was reduced to below 0.1^0C, and thus reduces the standard deviation of the temperature estimates in the temperature maps as shown in Table 3.5. These results, together with the reference signal-independent nature of the artifact as discussed in section 3.3, confirm that erroneous estimation of the water, not metabolite, frequency is responsible for the systematic error. The range of frequencies required to induce the observed temperature variation is just 0.4 Hz; thus even minute distortions to the water lineshape caused by the water suppression pulses or other factors may significantly affect the apparent temperature.

The default value of the BW of the RF pulses used for the CHESS was already higher (75Hz) compared to the B_o variations of 0-2 Hz thus further increase in BW does not reduced the systematic error in WS MRSI temperature mapping. It is not recommended to increase BW of CHESS pulses as it may reduce the intensity of the metabolite signals closer to water peak and may increase the SAR deposition. In contrast to strong water suppression, weakening the water suppression by increasing the delay τ produces uniform temperature maps. Weakening of WS can also be achieved by varying the flip angle (θ) of the RF suppression pulses or the delay τ (35). In this study three fixed bandwidth (75 Hz) RF pulses employed for CHESS had different flips angles (θ_1=105^0, θ_1=80^0, θ_3=145^0), changing θ_3 from 145^0 to 105^0 weakens the water suppression and produce similar results as obtained by using τ=68ms (data not shown). It is seen that the weakening the water suppression reduces the COV for WS factors (Table 3.5), thus it is argued that the uniform WS obtained by weakening WS, reduces systematic errors in MRSI temperature mapping.

Another approach to reduce the systematic error is to acquire water reference scans along with WS MRSI data as routinely acquired in SVS. The large water peak from the non-WS reference can be used to obtain the water frequency while the frequency of the metabolite internal reference can be estimated from the WS data to compute the frequency difference (Δ) and to estimate temperature. Using this approach it may be possible to avoid the systematic error observed using WS MRSI and the variability associated with using non WS data for temperature mapping. However collection of the additional non-WS reference scans doubles the acquisition time to 20 minutes. Thus this approach was not explored in this study. A more time efficient approach is to employ the faster echo planar spectroscopic imaging sequence as discussed by Ebel et al. (71), using this sequence a single WS-MRSI and the additional non water suppressed reference data (acquired in an interleaved manner) can be acquired in less than 3 minutes. The feasibility of this approach for temperature mapping will be discussed in Chapter 6, while following sections in this chapter will focus on further validation of the findings presented in this section and their applicability in-vivo.

3.5 Validation

3.5.1 Introduction

The appearance of the systematic error in MRSI temperature maps varies as the water suppression parameters are varied as discussed in section 3.4. It is also seen that the mean temperature of the phantom estimated using MRSI increased by ~1^0C during the course of the scans (Table 3.5) and indicates heating of the phantom during the course of the scans. The temperature of the phantom was monitored using a thermal strip with poor accuracy (±1^0C). This thermal strip does not allow direct quantification of this heating during MRSI scans and it is not clear whether internal real temperature gradients are present within the phantom and whether they are correlated with the systematic error. In this section a similar spherical phantom was constructed and provisions were made to monitor its temperature using optical thermometry, in order to assess internal temperature gradients within the

phantom and to quantify the heating of the phantom that occurs during MRSI scans.

3.5.2 Method and Materials

A spherical acrylic phantom was constructed. The phantom had similar volume to the GE MRS phantom (~2.7 litres) and phantom contained deionised water, N-acetyl-aspartic acid (12.5mM), L-Glutamic acid (mono-sodium salt) (12.5mM), Dotarem 0.1% (w/v). Provisions were made to measure the temperature of the phantom during the scans, using a two channel fibre optic thermometer (Model Luxtron 812, Luxtron Corp., Santa Clara, CA, USA) with an accuracy of 0.1^0C.

In order to assess internal temperature gradients the new phantom was placed in the scan position and its temperature was monitored by inserting 2 fibre optic probes at different depths along the axial scan plane. In order to assess the heating of the phantom during the scans, a number of MRSI scans in the order described in Table 3.7 were acquired after waiting overnight (>8 hours) to ensure thermal equilibrium was established. The MRSI data acquisition protocol and processing was similar to that discussed in section 2.5.2.

In order to verify the findings the scans using new home made spherical phantom, the manufacturers MRS sphere phantom (used in previous sections) was redeployed. The manufacturers MRS phantom was placed the scan position overnight to ensure thermal equilibrium and water suppressed MRSI scans (at two levels strong water suppression (τ=48ms) and weak water suppression (τ=68ms)) were acquired the next morning. These scans were repeated on different days to check for consistency.

3.5.3 Results

3.5.3.1 Real temperature gradient

The assessment of physical (real) temperature gradient performed using the new sphere phantom indicate an internal temperature gradient of 0.1-0.2^{0}C immediately after placing the phantom in the scan position as shown in Figure 3.7. It is also seen that following an equilibration period of several hours (>5 hours) in the scanner, the internal temperature gradients in the phantom are reduced to undetectable levels (<0.1^{0}C).

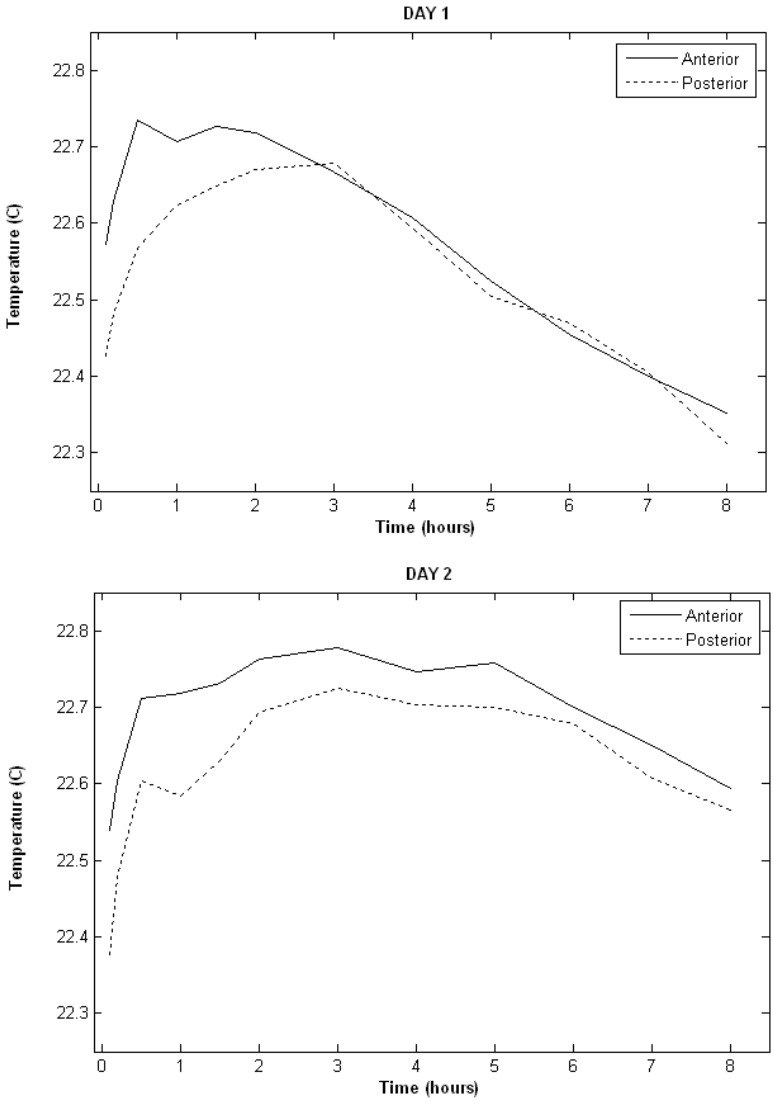

Figure 3.7 Physical temperature gradient in the custom made phantom measured using two fibre optic temperature probes on different days. The fibre optic thermometers were placed at different depths along the axial plane to measure the real temperature gradient.

3.5.3.2 Systematic error in temperature maps

A selection of temperature maps estimated using the WS MRSI data acquired using the home built sphere phantom are shown in Figure 3.8. The mean and SD of the temperature estimates obtained using MRSI are reported in Table 3.6. The temperature of the phantom monitored using the two fibre optic thermometers placed at different depths during the scans are also shown in the Figure 3.8. It can be seen that internal temperature gradients were not present during the scan. However the temperature maps acquired using strong WS (WS factor 90, BW:75, τ:48ms) exhibit a systematic error of 0.3^0C. This systematic error is further reduced when WS is weakened by increasing the delay τ to 68ms. The temperature maps acquired with weak WS are uniform within 0.1^0C. It is noted that the MRS temperature estimates obtained using this phantom are 2^0C higher compared to the measured temperature.

The temperature maps acquired using the manufacturers MRS phantom on different days are shown in Figure 3.9. Mean (SD) for these temperature maps are shown Table 3.7. It is seen that temperature maps acquired with strong WS (WS factor 60, τ=48ms) exhibit a systematic error, as phantom temperature was allowed to equilibrate overnight in the scanner the systematic error consistently reduces from 0.5^0C (reported in section 3.4) to 0.3^0C across different days. This systematic error consistently reduces to less than 0.1^0C when weak water suppression is employed (WS factor 15, τ=68ms) as previously discussed.

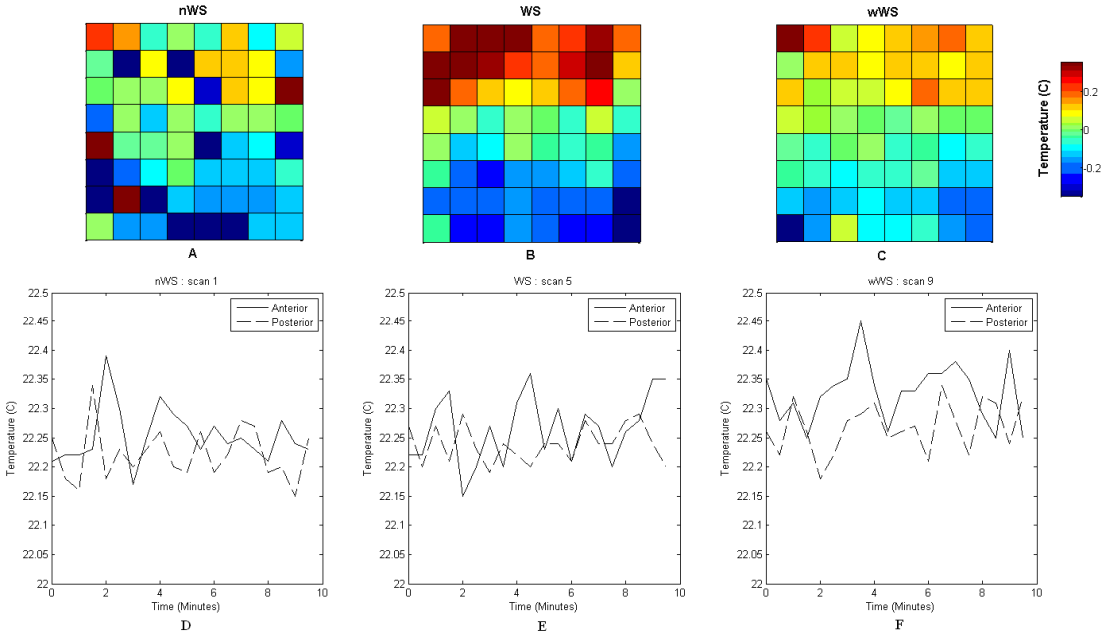

Figure 3.8 (A-C) Normalized temperature maps for scan number 1, 5 and 9 reported in Table 3.6, D-E, Temperature of the phantom during the respective scans measured using optic thermometry.

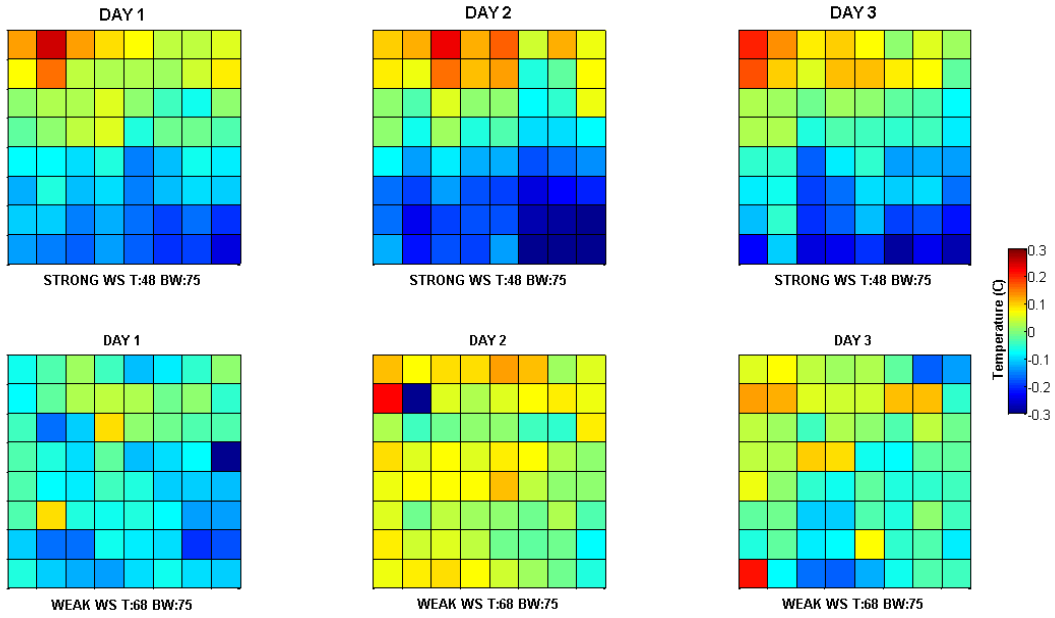

Figure 3.9 Normalized temperature maps acquired using the GE MRS sphere phantom on different days. The phantom was kept overnight in the scan position to reduce internal temperature gradients within the phantom. Top row are the temperature acquired using strong WS (τ=48ms) and bottom row are the temperature maps acquired using weak WS (τ=68ms), also see Table 3.7

	Water suppression			MRSI Temperature (^{0}C)		Number of voxel rejected
Scan #	Level	τ (ms)	BW (Hz)	Mean	SD	
1	NWS	NA	NA	24.48	0.59	14
2	NWS	NA	NA	24.56	0.34	13
3	NWS	NA	NA	24.63	0.31	19
4	NWS	NA	NA	24.59	0.28	7
5	WS	48	75	24.54	0.46	2
6	WS	48	75	24.57	0.39	0
7	WS	48	75	24.58	0.35	1
8	WS	48	75	24.63	0.33	0
9	wWS	68	75	24.63	0.12	1
10	wWS	68	75	24.70	0.27	5
11	wWS	68	75	24.67	0.14	0
12	wWS	68	75	24.72	0.18	1
13	WS	48	75	24.75	0.22	0
14	WS	48	90	24.76	0.21	0
16	WS	48	105	24.77	0.19	1
17	WS	48	120	24.80	0.18	1
18	WS	48	75	24.81	0.18	1
19	wWS	58	75	24.82	0.14	0
20	wWS	68	75	24.83	0.19	1
21	wWS	78	75	24.83	0.17	2
22	wWS	88	75	24.86	0.21	3

Table 3.6 Mean and SD of series of MRSI scans acquired back to back to assess heating effecting during the scans. The temperature of the phantom was monitor using 2 fibre optic thermometers and the phantom was kept in the scan position overnight to ensure thermal equilibrium. (also see Figure 3.11).

Day	WS	Temperature (^{0}C)		Number of voxels rejected
		Mean	SD	
1	Strong	22.85	0.11	0
1	Weak	22.92	0.07	3
2	Strong	22.75	0.13	0
2	Weak	22.77	0.06	1
3	Strong	22.49	0.13	0
3	Weak	22.56	0.08	1

Table 3.7 Mean (SD) of the temperature maps reported in the Figure 3.9, the temperature of phantom monitored using thermal strip was constant at 22^{0}C on these three days.

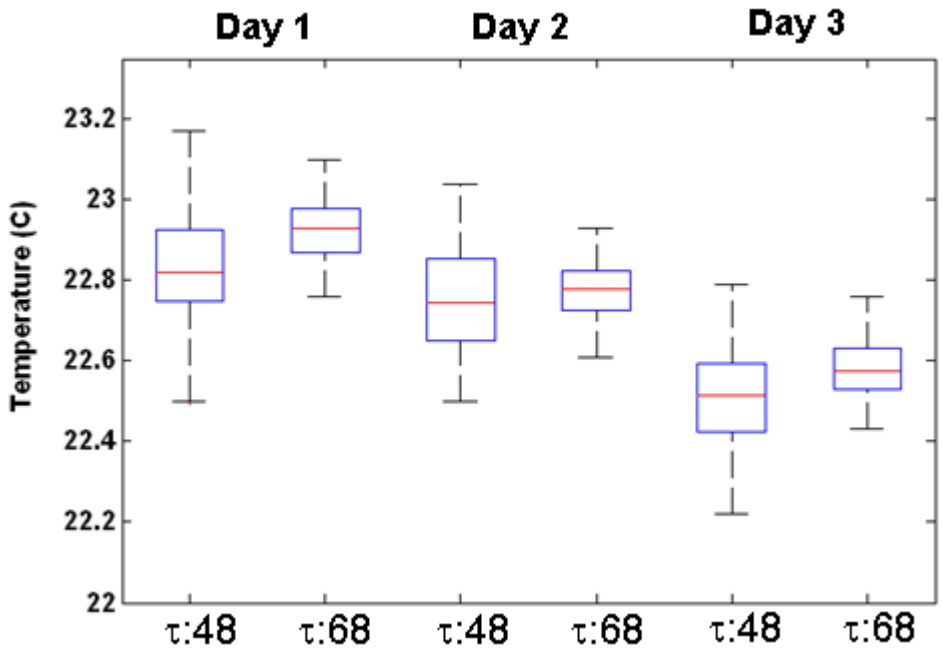

Figure 3.10 Box plots of the temperature maps reported in Figure 3.9

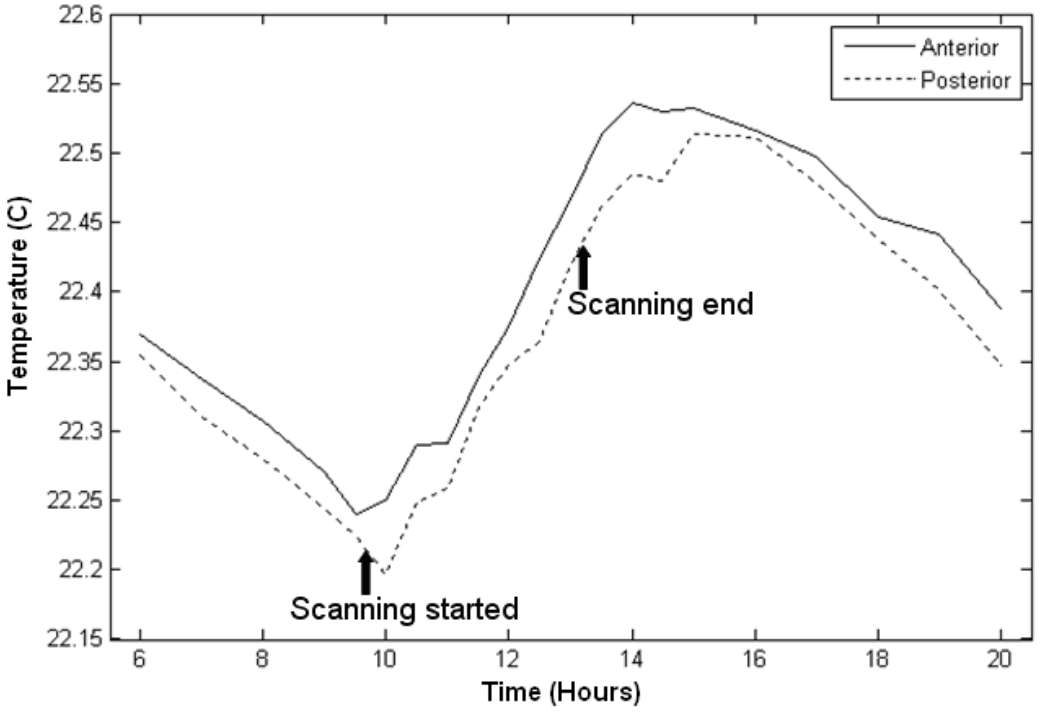

A

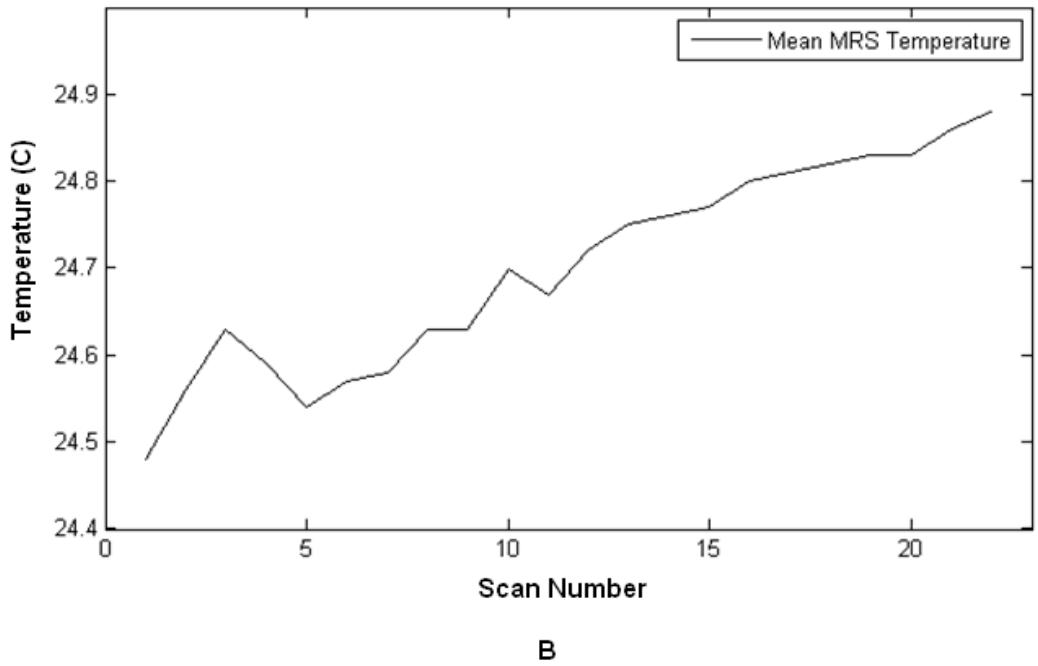

B

Figure 3.11 The temperature of the sphere phantom monitored a) using fibre optic temperature probe b) mean MRS temperature estimates during the scan reported in Table 3.6.

3.5.3.3 Heating effect during MRSI

The temperature of the custom built sphere phantom was monitored during the scanning session as shown in Figure 3.11. It can be seen that the temperature of the phantom increases during the course of the MRSI scans by ~0.3^0C. The mean MRS temperature estimates of the phantom during the scans as reported in Table 3.7 are plotted in Figure 3.11 b. The net temperature increase of the phantom after the MRSI scans computed using the mean temperature of each scan reported in Table 3.8 was 0.38^0C and was similar to that obtained using optical thermometry. Again the absolute temperature estimates obtained using the MRS were higher by ~2^0C.

3.5.4 Discussion

Physical temperature gradients in the custom built spherical phantom were measured using optical thermometry. It was seen that the internal temperature gradients (of about 0.1-0.2^0C) are present in the phantom immediately after placing the phantom in the scanner and long waiting period (>5 hours) is required for thermal equilibrium to be established. Thus all scans reported in this section were performed early in the morning after keeping the phantom in the scan position overnight to ensure thermal equilibrium. The systematic error observed in temperature maps estimated using strong WS (WS factor ~90, BW=75Hz and τ=48ms) consistently reduces from 0.5^0C as reported in section 3.4 to 0.3^0C for the both the custom built and manufacturers spherical MRS phantoms as seen Figures 3.8 and 3.9 and this error (of 0.3^0C) is reduced to less than 0.1^0C by using weak water suppression. The consistency of these findings on different days (Figure 3.9) suggests that part (0.1-0.2^0C) of the systematic error in the temperature maps (reported in section 3.2) was due to internal temperature gradients with in the phantom and the remainder is artifactual (due to WS) and this artifactual component of the systematic error can be reduced by weakening WS (as discussed in section 3.4)

It is well known that the use of RF pulses for localisation and water suppression increases the specific absorption rate (SAR) and may heat the sample (69). The temperature rise due to SAR deposition can be computed using the Pennes bioheat equation (9), but is challenging to perform localised SAR measurements and thus it is difficult to compute related temperature changes. The modelling approaches employed to estimate SAR are often qualitative and may or may not be applicable in-vivo (72). Thus, in this study a series of MRSI scans were acquired while monitoring the temperature of the (custom built) phantom using optical thermometry, in-order to quantity the heating effect (if any).

The optical temperature measurements suggests a minor ~0.3^0C increase in the temperature of the phantom after 22 MRSI scans and is in good agreement with temperature rise obtained using MRSI temperature estimates of the consecutive scans as shown in Figure 3.11. This result indicates an average temperature rise of less than 0.1^0C per MRSI scan and is too small to be measured accurately for each scan. It is also seen in Figure 3.11 (a) that temperature of phantom increases after the scans, indicating a rise temperature in the bore of the scanner as result of heat generated by the scanner electronics. These results indicate temperature rise due SAR related heating are likely not to influence MRSI based temperature mapping. However it is noted that these measurements were performed using 1.5T clinical scanner and at higher field strengths (3T or higher) the SAR related heating is likely to increase. Thus errors in temperature mapping due to RF heating during MRSI scans can be considered an active question at higher field strengths.

The MRSI temperature estimates obtained using the in-house sphere phantom were higher by 2^0C compare to the optical temperature measurements. In contrast the temperature of the manufacturers MRS phantom measured using the LCD thermal strip and MRS was similar (~ 22^0C). Both spherical phantoms were always stored in the scanner room as the temperature of the scan room is regulated to 22^0C (+/-0.3^0C) and the only major difference between the two phantoms is the constituents of their

aqueous solutions. Recently, calibration constants used to obtain absolute temperature from the MRSI data are reported to depend on the ionic strength of the solution employed to obtain calibration constants and thus may explain this inconsistency (50;51) and will be explored in detail in chapter 4. In the following section the in-vivo applicability of these results will be determined.

3.6 In-vivo study

3.6.1 Introduction and Methods

The temperature maps from phantom data exhibit a systematic error, thus it is necessary to assess whether the systematic errors can be identified and reduced in the temperature maps estimated using in-vivo WS-MRSI data. For this purpose MRSI dataset at various levels of WS were collected from 2 young healthy volunteers (1 Male, aged 33 years and 1 Female, aged 26 years) by changing the delay τ from default value of 48ms to 88ms using 10ms increments. A non water suppressed data set was also acquired. Consistent shim and prescan settings were employed for all MRSI scans acquired within the same sessions. The MRSI acquisition and processing were the same as those reported in section 3.4. Additionally, four saturation bands were used to suppress subcutaneous lipid signals and volumetric T_1 weighted (coronal; TR/TE 4/8 ms, slice thickness 1.3mm.) and T_2 weighted (axial; TR/TE 102/11320ms) scans were acquired to facilitate positioning of the VOI as shown in Figure 3.12. Both volunteers gave informed consent and the scanning was approved by the local research ethics committee.

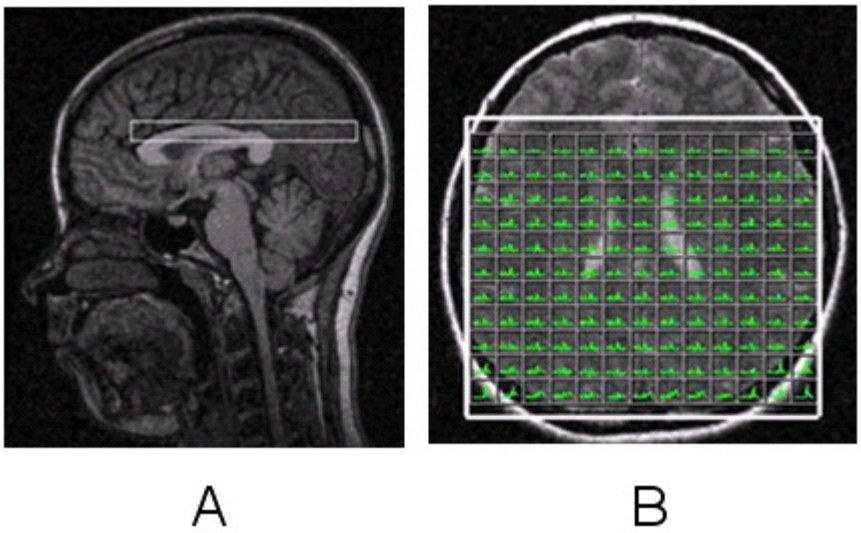

Figure 3.12 MRSI slice positioning for acquiring in-vivo temperature maps

3.6.2 Results

The temperature maps estimated from a volunteer scan acquired using strong WS and weak WS is shown in Figure 3.13. As seen the systematic error previously observed in phantom scans cannot be identified in in-vivo temperature maps. The mean and SD of the temperature estimates for all scans is reported in Table 3.8 and as seen a higher T_{sd} is reported for volunteers scans compared to phantom scans. The default/strong WS factor (i.e. at τ=48ms) obtained in-vivo was lower (by a factor of ~2.5) compared to that obtained for the phantom scans. The WS factors obtained using weak WS (τ=58-88ms) were similar in-vivo and in phantoms. The box plot for temperature estimates for the in-vivo scans shown in Figure 3.14, indicates a reduced temperature variation when weak water suppression (τ=68ms) is employed. For each of the 3 scans reported in Table 3.8, a higher number of voxels were rejected (based on the quality assurance criteria, NAA linewidths <10Hz) when no WS was employed.

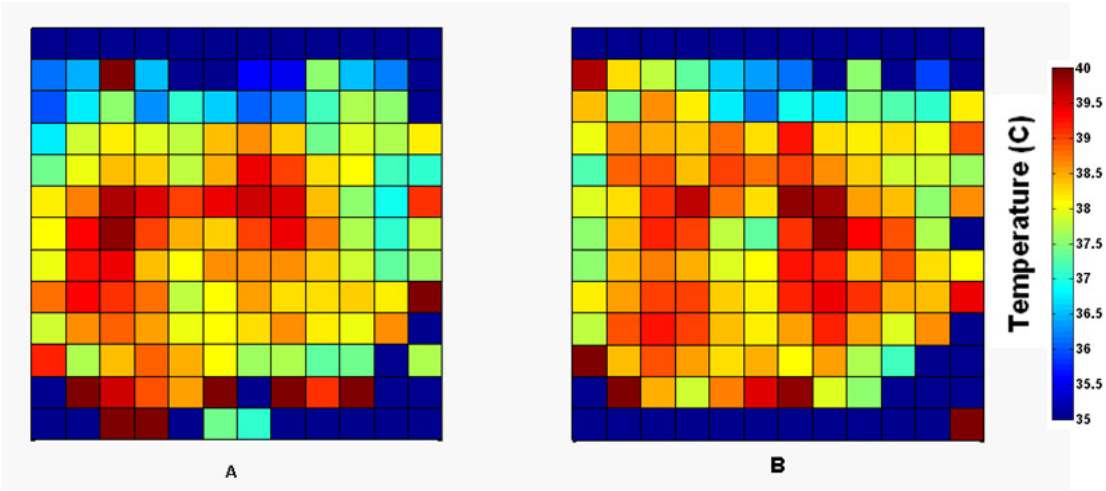

Figure 3.13 Examples of in-vivo temperature maps acquired from a volunteer using a) strong WS (τ=48ms) b) weak WS (τ=68ms).

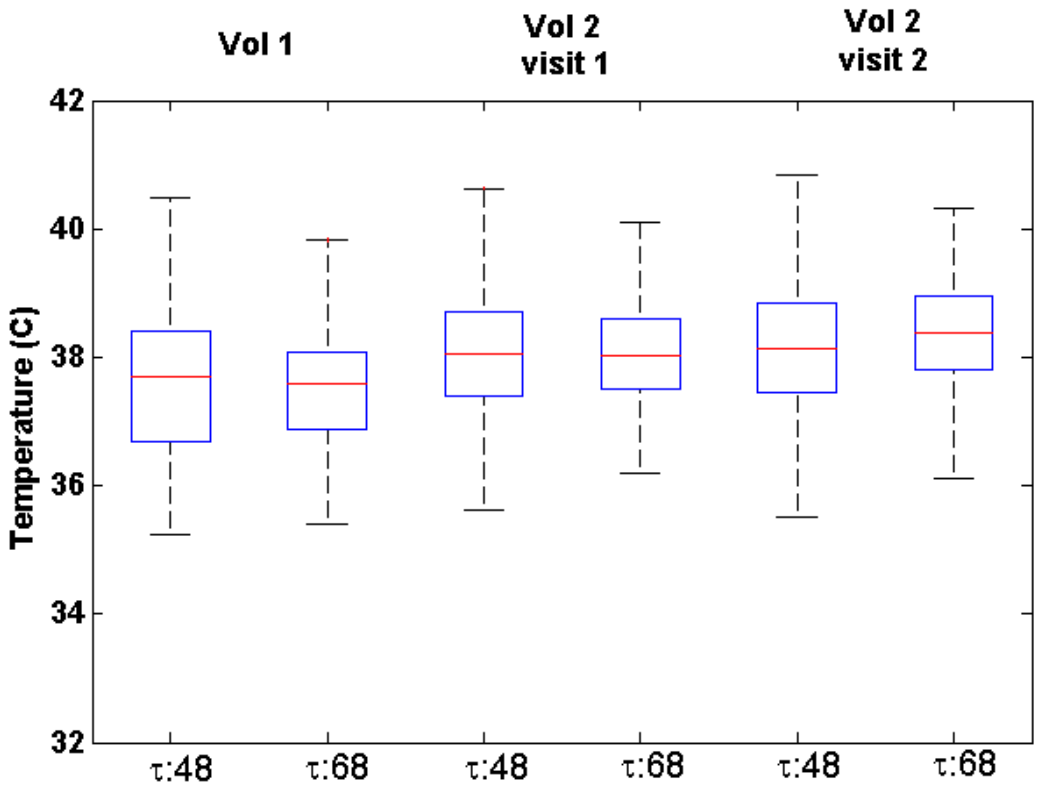

Figure 3.14 Box plots of temperatures maps acquired using strong and weak water suppression for the two volunteer scans.

	Volunteer 1			Volunteer 2 visit 1			Volunteer 2 visit 2		
τ (ms)	Rejected voxels	Temperature (^{0}C)	WS Factor	Rejected voxels	Temperature (^{0}C)	WS Factor	Rejected voxels	Temperature (^{0}C)	WS Factor
48	8	37.1 (2.24)	36.7 (15.3)	26	38.1 (1.87)	39.6 (11.3)	8	38.1 (1.47)	35.8 (10.1)
58	7	37.3 (1.96)	21.7 (7.9)	30	38.4 (1.46)	22.8 (5.3)	11	38.3 (1.46)	19.8 (4.8)
68	10	37.0 (2.02)	15.1 (4.8)	21	38.3 (1.26)	15.9 (3.0)	12	38.0 (1.51)	16.3 (2.8)
78	11	37.5 (1.57)	13.1 (4.2)	23	38.3 (1.55)	12.4 (2.9)	7	37.9 (1.35)	12.4 (2.1)
88	20	36.6 (1.68)	10.2 (2.3)	37	38.4 (1.51)	10.6 (3.9)	12	38.2 (1.16)	10.11 (2.0)
nWS*	20	37.9 (2.09)	1	37	38.4 (1.16)	1	23	37.8 (1.19)	1

Table 3.8 Mean (SD) of temperature estimates across the VOI at different levels of WS for volunteer scans.

3.6.3 Discussion

The systematic errors cannot be identified in the temperature maps obtained using WS-MRSI data acquired in-vivo. The T_{sd} varies between 1.50-2.24 ^{0}C (table 3.9) and is higher compared to that obtained for the phantom studies. The main reason for the higher T_{sd} in the volunteer scans is the random errors in temperature estimates due to the larger linewidths. The prescan linewidths of the water peak for in-vivo scan varied between 6-10Hz and were higher compared to those (1Hz) obtained for the phantom scans. Thus it is possible that the random errors due to larger linewidths may have masked the relatively smaller systematic errors (0.3^{0}C) observed in the phantom scans. The variability in the in-vivo temperature estimates (somewhat) reduces, when the water suppression was weakened (Figure 3.14). It is also worth noting that default water suppression appears to be substantially less effective in-vivo, which may have reduced systematic effects. Thus although it is uncertain whether this systematic error affects data in-vivo, it would be prudent to avoid the use of highly optimised water suppression when acquiring brain temperature maps using MRSI.

3.7 Summary

In this chapter, it was shown that systematic error exists in MRSI based temperature mapping acquired with strong water suppression. The nature of this systematic error depends on the set up, the design of the MRSI pulse sequence and WS scheme employed. Weakening WS reduces the systematic error in temperature maps due to water suppression. Although the systematic error cannot be identified in the temperature maps obtained using in-vivo MRSI data these errors may affect regional temperature estimates pooled for a number of volunteers. Thus it is prudent to employ weak WS while acquiring MRSI data to reduce the scope of the systematic error in temperature maps.

Although the systematic errors due to MRSI water suppression can be reduced, there are other considerations, which may influence estimation of the frequency difference between water and internal reference metabolite peak and thus MRS temperature estimates. Firstly, a recent study reports that the frequency of the metabolite peaks (used as internal reference) are different in gray and white matter (66). It is also reported that the calibration curves used for internal reference MRS thermometry may be sensitive to tissue composition (50;51). Thus further validation of temperature estimates obtained using MRSI is necessary and discussed in the following chapters.

4 In-vitro validation

4.1 Introduction

The linear variation of the proton frequency shift with temperature has been validated to measure brain temperature using single voxel spectroscopy (SVS) (41;73). In contrast to SVS, MRSI is technically demanding and a comprehensive validation of MRSI temperature mapping is necessary but lacking. In this chapter a series of experiments designed for in-vitro validation of MSRI temperature mapping are discussed. In section 4.2, the design of a 2 chamber temperature controlled phantom will be presented. The minimum temperature difference detected using MRSI will be discussed in section 4.3. The effect of varying the ionic strength of the solution used to obtain the calibration constants in order to estimate absolute temperature using MRS data will be investigated in section 4.4, while the effect of varying the amplitude of the internal reference (NAA) on repeatability MRSI of temperature estimation will be presented in section 4.5.

4.2 Design of a temperature controlled phantom

The need to employ a temperature controlled phantom for in-vitro validation of MRSI temperature mapping has already been presented. MRSI based temperature maps acquired using the room temperature phantom are subjected to room temperature variations and heating during the scan as discussed in chapter 3. Thus the first aim of this work was to design a temperature controlled phantom to allow in-vitro validation of MRSI based temperature mapping. A number of studies have employed temperature controlled phantoms for in-vitro validation of single voxel internal reference MRS thermometry (41;42;47;49;50;73). These studies employ a phantom which consists of a central chamber consisting of a solution containing brain metabolites. The temperature of the metabolite solution is regulated generally by circulating water around the chamber at constant temperature using a water bath. Optical thermometry is used to measure the temperature of the solution during the scans. This set up is also useful to obtain calibration constants by acquiring SVS at different temperatures (details: Table 2.2,

chapter 2). The calibration constants are inferred from the regression analysis on the frequency difference between water and the internal reference metabolite peaks (usually NAA) and the temperature of the solution (or sample) measured using optical thermometry.

As MRSI offers a larger coverage, the aim was to construct a phantom with 2 metabolite chambers with independent temperature control. Thus metabolite chambers can be set to different temperatures and direct regional analysis of MRSI temperature maps can be performed. Although simplistic, the design of the phantom needs to be tailored so that excellent shimming can be performed and good quality MRSI data can be acquired. A number of phantom prototypes were tested for this purpose and are described in the following paragraphs.

4.2.1 Prototype 1

The use of water baths poses a risk of water spillage inside the MRI scanner, thus an alternate set-up was proposed Dr Steven Hammer. It was suggested to employ Peltier elements to cycle the temperature rather than using water baths. Peltier elements are semiconductor devices with metallic coating. Applying a DC voltage across the device causes one face to get cooler and the other face to heat up as heat is transferred across the device. The elements are available in different sizes and cooling powers. The Peltier element employed for this prototype is shown in Figure 4.1.

The first prototype of the temperature controlled phantom is shown in Figure 4.2 and consists of a cylindrical plastic container with a solution holder. The phantom is filled with water and on closing the lid, the MRS solution (within the metabolite chamber) is completely immersed in water. The heat sink and Peltier element is attached to the bottom end of the container as shown in Figure 4.2 c and is used to control the temperature of the phantom. Temperature control is achieved by regulating the DC voltage to the Peltier element. To minimize heat loss to the surroundings a thermal sleeve was employed. After preliminary bench testing for temperature control, this

prototype was scanned using a GE 1.5T SIGNA MR scanner (GE Healthcare, Slough, UK).

Figure 4.1 Peltier element (SealTEC, ST1.4-127-06L, Melcor Thermoelectric Devices, NJ, USA) employed for temperature control phantom (also see Figure 4.2).

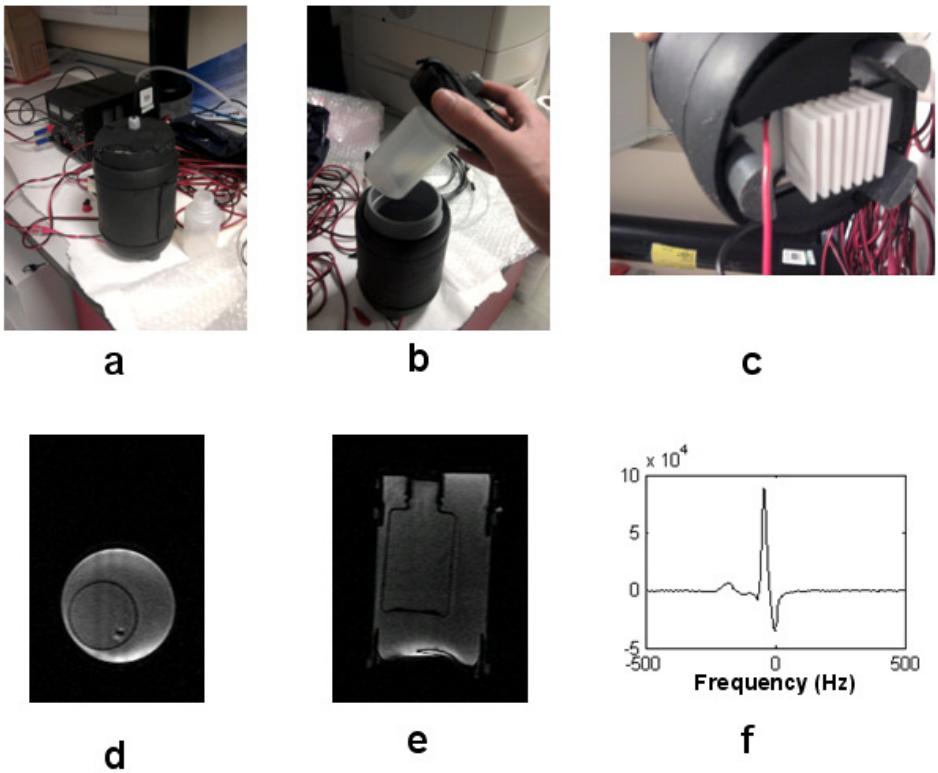

Figure 4.2 a) Temperature controlled phantom and the DC supply to the Peltier element. b) The Metabolite chamber c) Peltier element attached with the heat sink d) and e) Coronal and axial localiser images of the phantom f) typical water suppressed single voxel spectrum (without removal of the residual water peak).

The coronal and axial localiser images of the phantom are shown in the Figure 4.2 (d-e). The water and metabolite chambers can be easily visualized. The metabolite chamber was filled with a 12mM sodium acetate solution. A water suppressed single voxel spectrum acquired from the central region of the metabolite chamber acquired as electric current was being applied to the Peltier device is shown in Figure 4.2 f. It is seen that the residual water peak is severely distorted. The B_o field inhomogeneity was assessed by recording the linewidth of water peak obtained after automatic shimming. This prescan linewidth was 8 Hz and was higher compared to typical linewidth of 1-2 Hz obtained using a uniform room temperature phantom as reported chapter 3. The shape of the phantom, its metallic content and interference of the magnetic fields generated by electric current applied to the Peltier element, were the likely reason for the poor shimming. Thus it was necessary to pursue an alternative set-up to improve the B_o homogeneity and improve MRSI data quality. This phantom prototype (i.e. Prototype 1) was constructed jointly by Dr Hammer and Dr Michael Thrippleton. The author jointly performed MR testing of the phantom with Dr Thrippleton.

4.2.2 Prototype 2

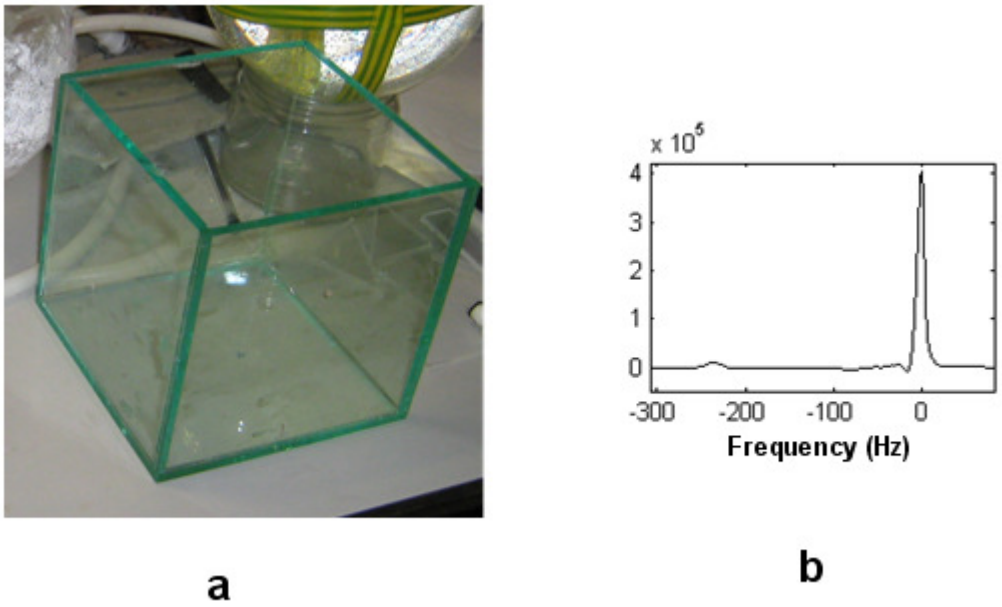

Figure 4.3 (a) Prototype 2 used to assess the effect of geometry on design considerations b) typical water suppressed single voxel spectrum (without removal of the residual water peak).

In order to assess the influence of geometry on shimming a second prototype was tested. A number of single voxel MR spectra (TE/TR, 144/1500ms and voxel size 1.5cm^3) were acquired using a cubic acrylic phantom as shown in Figure 4.3. The phantom was filled with 12mM sodium acetate and the voxel was located centrally. The typical prescan linewidth obtained was 4-5 Hz and was closer to 1-2 Hz linewidth obtained using spherical phantoms. This observation fits in the theoretical consideration that improved shimming is obtained over spherical objects, as a result of which the routinely employed automatic shimming routines are based on spherical harmonics functions (74;75). Thus it was a natural choice to employ a spherical design for the phantom.

4.2.3 Prototype 3

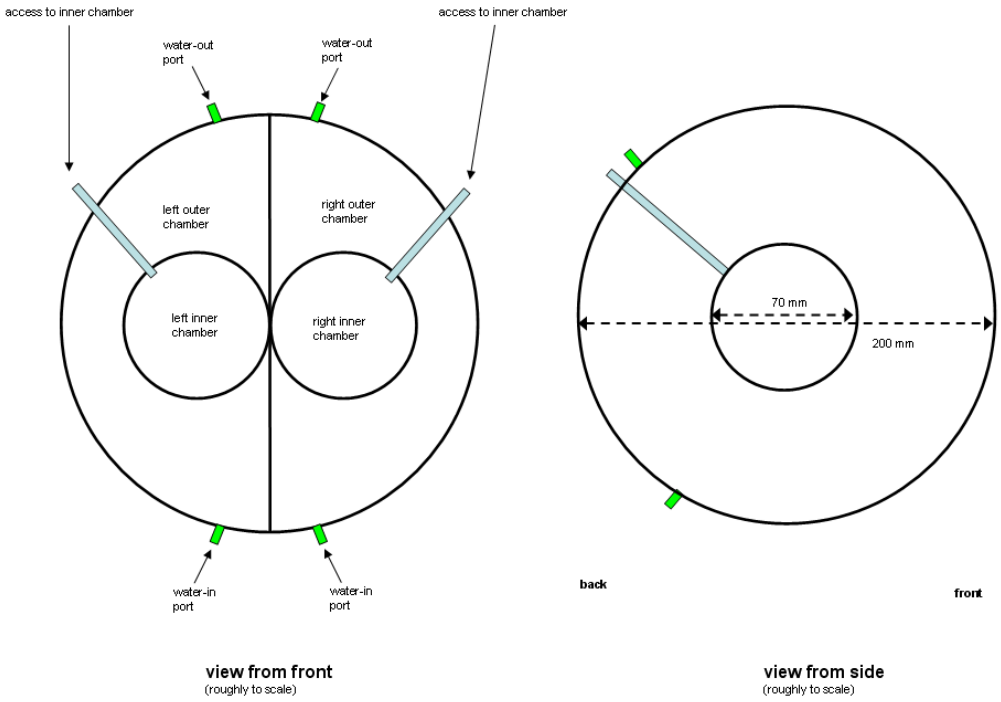

Figure 4.4 Schematic diagram of the 2 chamber temperature controlled phantom (Prototype 3).

Prototype 3 is the first spherical design as shown in Figure 4.4. It consists of two metabolite chambers (volume ~115ml each) separated by an acrylic sheet. Water baths were employed to circulate water around each chamber to achieve temperature control. Provisions were made to measure the temperature of the phantom using fibre optic thermometers as shown in Figure 4.4. Bench tests were performed to determine a waiting time of 45 minutes to ensure temperature stabilisation and to achieve set temperatures after the onset of temperature cycling using water baths (see Figure 4.5). Internal temperature gradients in the metabolite chambers were minimal during the temperature cycling as shown in Figure 4.6. Both of the sides had similar response. The temperature of the water bath also had to be adjusted to account for heat loss of the water en route to the phantom. Thus using optical thermometry the temperature of the metabolite chamber was monitored and if necessary the water bath settings were varied to ensure set temperature during the scan. The construction of this phantom and related lab testing was performed jointly by the author and Dr Thrippleton.

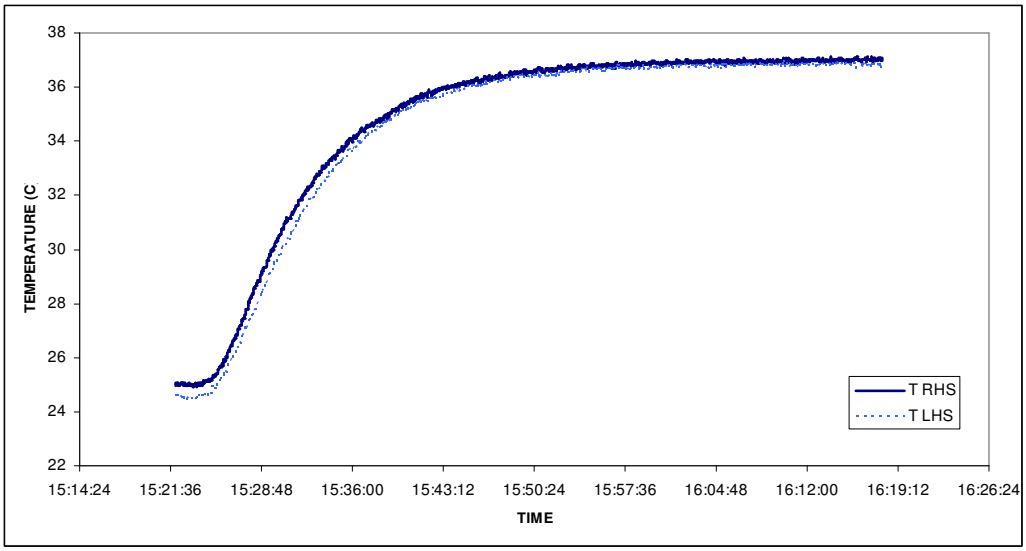

Figure 4.5 Temperature of the metabolite chamber monitored while heating the metabolite chamber from room temperature to 37^{0}C. It is seen that stable temperature can be observed after 45 minutes of heating.

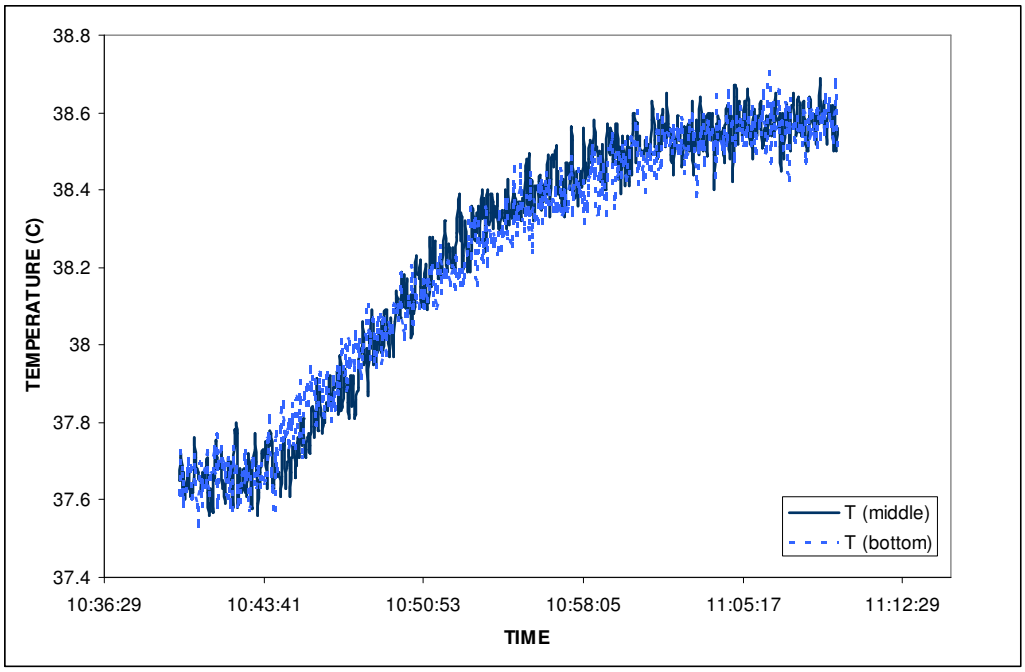

Figure 4.6 Temperature distributions within the metabolite chamber obtained by placing 2 fibre optic thermometers at different depths (middle and bottom) within the chamber during temperature cycling. No internal temperature gradients were observed as the temperature of the metabolite chambers was increased by 1^{0}C.

4.3 MRSI testing of prototype 3

4.3.1 Introduction

After promising results of the bench tests, a number of preliminary scans were performed. A working scan set-up to prevent water spillage in the scanner was determined. The prescan linewidths obtained after shimming varied between 1-2Hz. Test MRSI scans were acquired by using a 12mM sodium acetate solution and the two chambers were set to different temperatures (LHS~30^{0}C and RHS ~35 ^{0}C), this temperature difference (of 5^{0}C) was identified in the MRSI temperature map. Thus a series of MRSI scans were acquired to identify the minimum temperature difference, which can be detected using MRSI and temperature controlled phantom. The results of this experiment are presented in this section.

4.3.2 Methods

Weak water suppressed MRSI data (τ=68ms) were acquired using the protocol previously discussed in section 2.5.1 at different temperature settings using temperature controlled phantom (Prototype 3). Acquisition parameters are described in Table 4.1. Weak water suppression (τ=68ms) was employed to reduce systematic errors as discussed in chapter 3. The MRSI VOI 'PRESS box' was carefully positioned as shown in Figure 4.7 to avoid artifacts from flowing water using localiser scans. The metabolite chambers had identical solution containing 12.5mM NAA, 12.5mM L-Glumatic acid and 0.1% weight/volume of Dotarem. The temperature of the left metabolite chamber was always held constant at 37^{0}C during the scans, while the temperature of right metabolite chamber was varied between 37-38^{0}C in the order as shown in Table 4.2. This set up allows us to assess whether MRSI temperature mapping can be employed to identify small temperature difference (in the range of 0.2-1^{0}C) between the two chambers. In order to ensure thermal equilibrium during the scans, the waiting time between temperature cycling and subsequent MRSI acquisitions was 1 hour. The temperature of the metabolite chambers was continuously monitored using two fibre optic

thermometers (Model Luxtron 812, Luxtron Crop, Santa Clara, CA, USA) for the scan duration (~6 hours).

Sequence	MRSI (2D-PRESS MRSI)
Orientation	AXIAL
TE/TR(ms)	145/1000
Spectral width (Hz)	1000
Number of Samples	512
FOV (mm)	300
Slice thickness (mm)	10
Matrix size	24*24 (interpolated to 32*32)
Number of slices	1
Voxel size (cm^3)	0.85
Scan time	9 minutes 40 seconds

Table 4.1 MRSI acquisition setting used for in-vitro validation experiments.

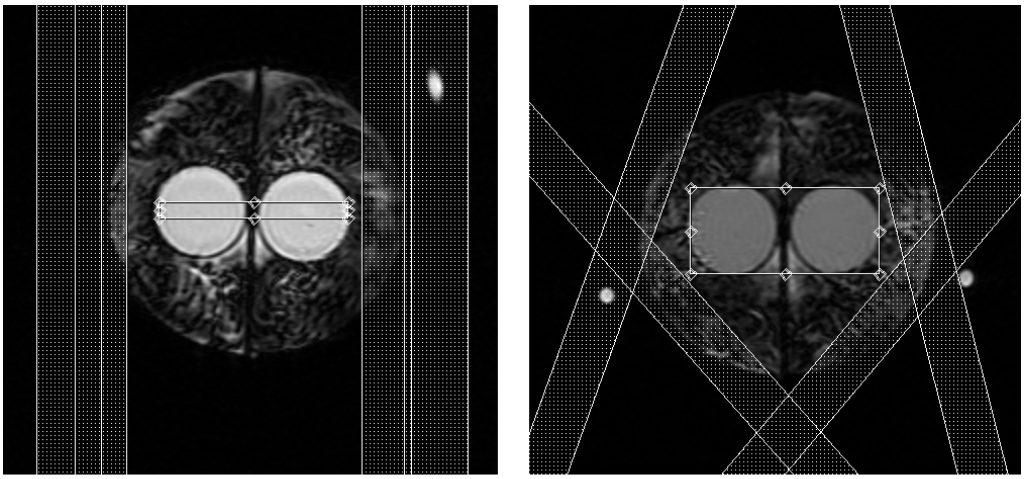

A B

Figure 4.7 Coronal (a) and Axial (b) localiser images of the temperature controlled phantom showing the MRSI VOI positioning. The MRSI VOI encloses the two metabolite chambers which are separated by a plastic partition.

The MRSI data were processed in the standard manner as described in section 2.5 to obtain temperature maps using NAA as the internal reference. The mean and the standard deviation of the temperature estimates were computed from 2 regions of interest (ROI) for the left and right metabolite

chambers as shown in Figure 4.8. As a quality assurance measure all the spectra with NAA linewidths greater than 10 Hz were excluded from the analysis. The temperature maps were normalized by subtracting the median MRSI temperature (of the respective ROI) for display purposes.

4.3.3 Results and Discussion

A typical MRSI array of spectra obtained using the temperature controlled phantom is shown in Figure 4.8. The mean linewidth of NAA peak for left and right regions of interest (ROI) were 1.3 Hz (SD 0.2 Hz) and 1.4 Hz (SD 0.3 Hz) respectively. The linewidths were similar for all 5 scans and are comparable to that obtained using the room temperature phantom (1-2 Hz). The MRSI temperature maps acquired at different temperature settings are shown in Figure 4.9. The temperatures of the chambers monitored using the fibre optic thermometers during the MRSI scans are shown in Figure 4.10. Mean of the fibre optic temperature measurement and MRSI temperature estimates are shown in Table 4.2. The SD of the fibre optic temperature and MRSI temperature estimates was less than 0.1^0C for all scans and both the metabolite chambers and thus indicates excellent temperature stability of the set up and that excellent temperature control can be obtained to perform in-vitro validation. It can be seen that using a single MRSI scan, a temperature difference as low as 0.2^0C can be detected using this set up. It is also noted that absolute MRSI temperature estimates are higher by ~2^0C than the temperature of the metabolite chamber measured using fibre optic temperature probes and thus further validation for accurate calibration is necessary (see section 4.4).

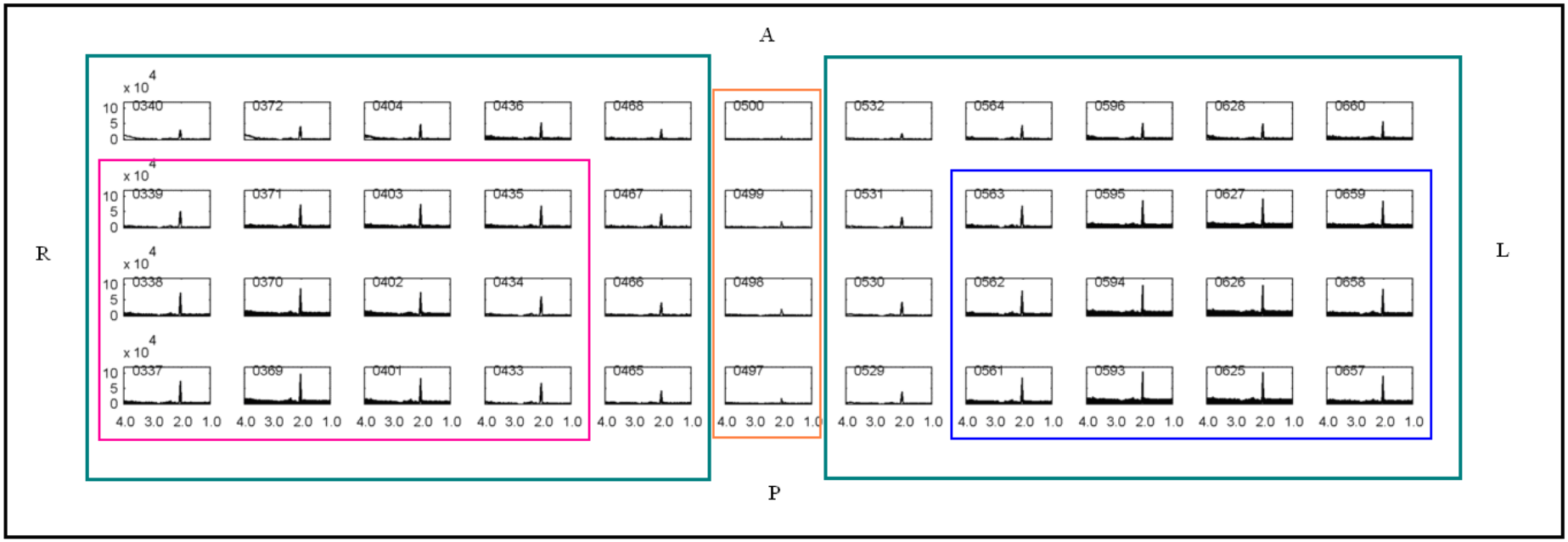

Figure 4.8 Array of MRSI spectra within the PRESS box, obtained using the temperature controlled phantom. Also shown are the voxels across the 2 metabolite chambers (in green) and respective regions of interest (RHS in red and LHS in blue). The metabolite chambers contained the same metabolites (12.5mM NAA, 12.5 mM L-Glumatic acid and 0.1% w/v Dotarem) and were maintained at the same temperature ($T_{set}=37^0C$). The voxels enclosed in the orange box include the plastic partition in the midline between the two chambers (as seen in Figure 4.7). Notice the presence of marginal NAA signal in these voxels due to voxel bleeding as discussed in section 2.3.2.

		Fibre optic Temperature (^{0}C)			MRS temperature (^{0}C)		
Scan	Set temperature difference	LHS	RHS	ΔT	LHS	RHS	ΔT
1	0.0	36.98	37.00	0.02	39.45	39.49	0.04
2	0.2	36.99	37.16	0.17	39.50	39.68	0.18
3	0.3	36.98	37.25	0.27	39.48	39.76	0.28
4	0.5	37.00	37.42	0.42	39.49	39.94	0.45
5	1.0	37.03	37.91	0.88	39.51	40.40	0.89

Table 4.2 Mean MRSI temperature estimates for the two (left and right) regions of interest for temperature maps as reported in Figure 4.9 and fibre optic temperature of the chambers are also shown.

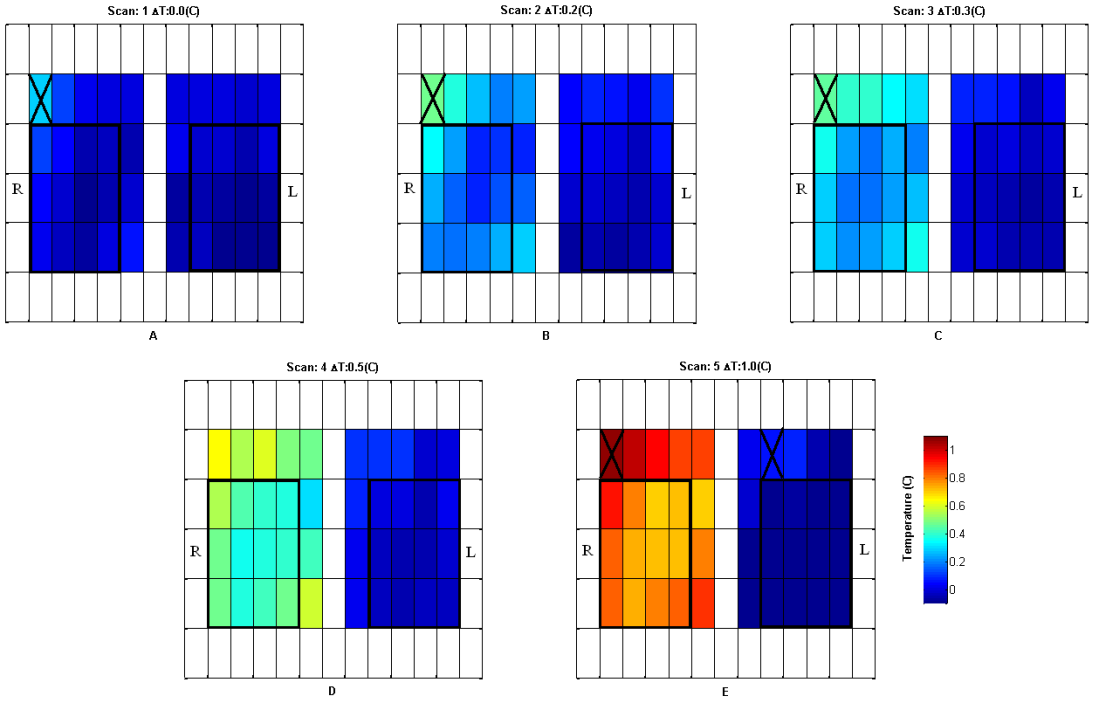

Figure 4.9 Normalized temperature maps estimated using MRSI data acquired from the temperature controlled phantom, the voxels rejected based on quality assurance criteria are indicated using a cross and the two ROI for left and right metabolite chamber are shown. (see also Table 4.2).

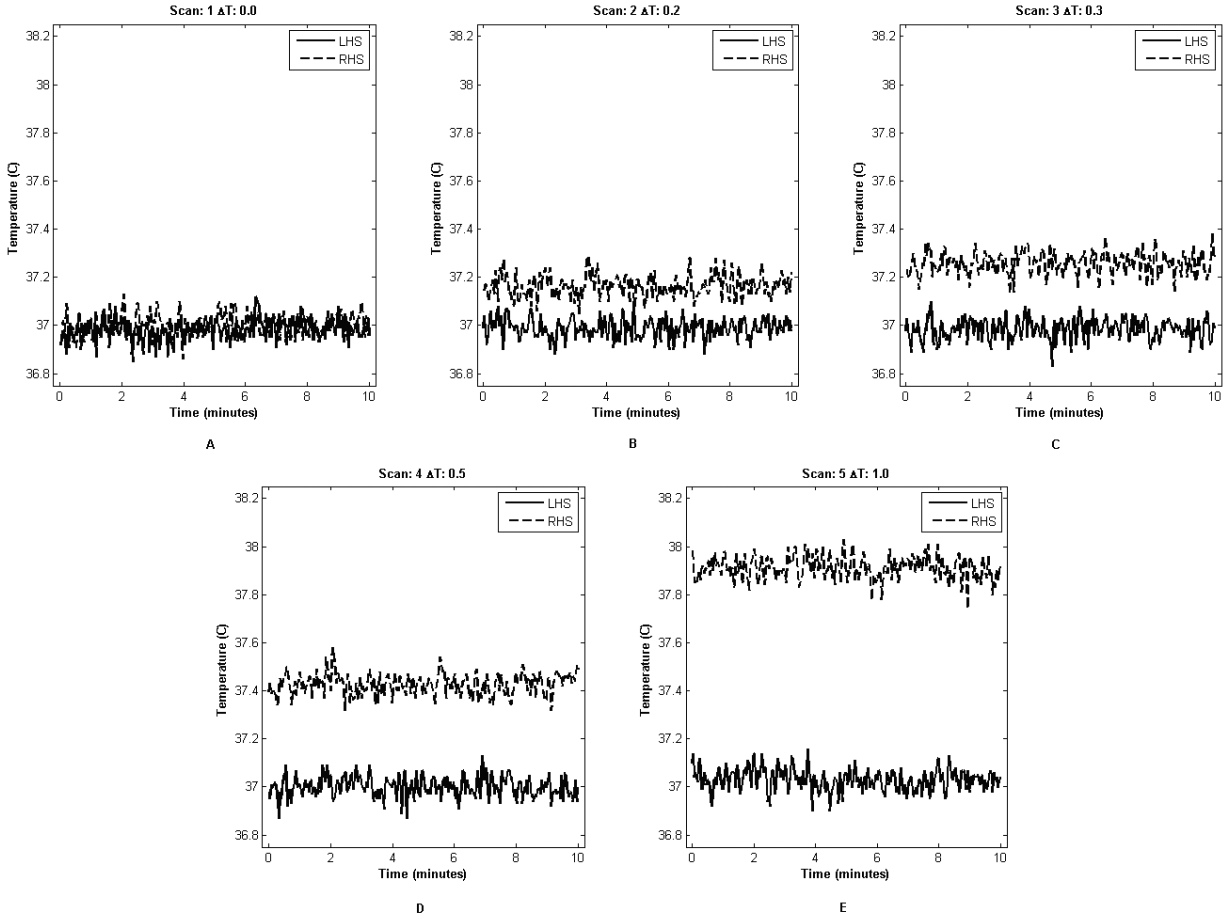

Figure 4.10 Temperatures of the two metabolite solution chambers monitored using two fibre optic thermometers for temperature maps reported in Figure 4.9

4.4 Calibration

4.4.1 Introduction

It is crucial to accurately calibrate the frequency difference (Δ) between the water and metabolite peak to obtain accurate temperature estimates using internal reference MRS. It was seen in the previous section that temperature differences of as low as 0.2^0C can be identified using MRSI, however the absolute MRS temperature estimates differed by 2^0C compared to the actual temperature measured using optical thermometry, this systematic over estimation of the temperature is a likely result of calibration error. A number of studies have calibrated the frequency difference (Δ) to obtain accurate temperature estimates using MRS (see Table 2.2 Section 2.4). It is seen that the nominal frequency difference (Δ) anticipated at 37^0C between water and NAA peaks varies and thus the absolute temperature estimated using MRS may vary by up to ~3^0C depending on which calibration curve (reported in Table 2.2) is employed. Thus it is important to investigate the source of this in-consistency. A recent study by Vescovo et al. (50;51) suggests that the ionic strength and the protein content of the solution employed for calibration influences the calibration curve. The aim of the experiment presented in this section was to verify the finding whether changes in the ionic strength of the solution affect the calibration constants (slope-A and intercept-B).

4.4.2 Methods

In order to calibrate the frequency difference (Δ), a solution (label Solution 1) containing brain metabolites at physiological concentration was used (for details refer Table to 3.1 Section 3.2). To assess the influence of change in ionic content on the calibration curve 100 mM NaCl was added to this solution. The temperature controlled phantom (prototype 3) was employed. The two metabolite chambers of the temperature controlled phantom contained the same aqueous solution but at different ionic strength (LHS- Solution 1 plus 100mM NaCl, RHS- Solution 1). The temperature of the chambers was varied using water baths and the waiting time between each temperature set points was 1 hour to ensure thermal equilibrium. Weak water

suppressed single voxel spectra using PRESS localisation (TR/TE/Nx, 1500/144/16 (ms), spectral width 1000Hz and voxel size 2 cm^3) were acquired at 4 different temperatures (24.0^0C, 30.5^0C, 37.0^0C and 43.5^0C) on both hemispheres. Single voxel data were processed in similar manner as discussed in section 2.5.2 to obtain the frequency difference (Δ) between water and metabolite internal reference peaks (Cre, Cho and NAA) at various temperatures. The temperature of the solution was measured using fibre optic thermometers during the scans and regression analysis was performed between the fibre optic temperature and the frequency difference (Δ) to obtain calibration constants.

4.4.3 Results

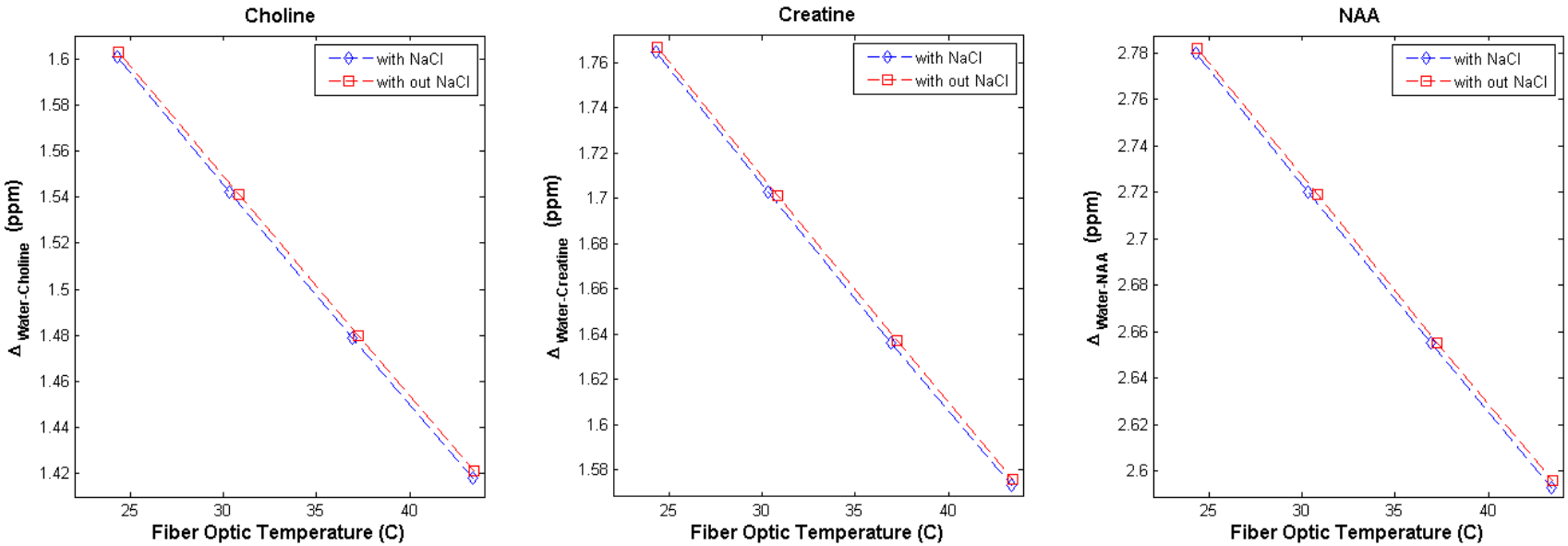

Figure 4.11 Plot of the frequency difference ($\Delta_{water\text{-}reference}$) and optical temperatures for different metabolites used as internal reference (also see Table 4.3)

Mixture	Internal Reference	Slope (^{0}C/ppm)	Intercept (^{0}C)	Δ at 37^{0}C (ppm)	ΔT (^{0}C)
Solution 1 **without** 100mM NaCl	Choline	-105.1	192.8	1.4824	-
	Creatine	-100.1	201.5	1.6434	-
	NAA	-102.5	309.5	2.6585	-
Solution1 **with** 100mM NaCl	Choline	-104.4	191.3	1.4780	0.4
	Creatine	-99.3	199.5	1.6365	0.7
	NAA	-102	307.9	2.6559	0.3

Table 4.3 Calibration constants (slope A) and (intercept B) for different metabolites used as internal reference obtained from data presented in Figure 4.11. The anticipated frequency difference (Δ) at 37^{0}C for each calibration curve and the temperature difference (ΔT) between the calibrations (with and without NaCl) are also shown. Solution 1 contains brain metabolites at physiological concentration (for details refer Table to 3.1 Section 3.2).

Plots of the frequency difference (Δ) and fibre optic temperatures for different internal references and ionic strengths are shown in Figure 4.11 and the results of the regression analysis are reported in Table 4.3. In addition to the calibration constants (A and B), the typical frequency differences ($\Delta_{water-reference}$) for the phantom mixture (Solution 1 without NaCl at 37.11^{0}C) and for primary white matter voxels estimated using MRSI data acquired at the level of the corpus callosum from 12 healthy male volunteers (for details refer section 5.3) are shown in Table 4.4.

Sample	$\Delta_{Water-Choline}$ (ppm)	$\Delta_{Water-Creatine}$ (ppm)	$\Delta_{Water-NAA}$ (ppm)
Solution 1 at 37.11 ^{0}C	1.481	1.639	2.656
Human white matter	1.449	1.637	2.654

Table 4.4 The typical frequency difference obtained from MRSI scans of phantom and volunteers MRSI scans.

4.4.4 Discussion

A new set of calibration curves, obtained using a solution containing brain metabolites at physiological levels are reported in this section. It is verified that the ionic strength of the solution influences the calibration constants. It is observed that on increasing the ionic strength, both the slope and intercept reduces slightly as shown in Table 4.3 and thus produces lower temperature estimates. However these findings are different to those reported by Vescovo et al. (51) who suggests that increasing the ionic content increase the intercept and reduces the slope (see Table 2.2 Section 2.4). This difference of observation is likely due to the fact that Vescovo et al. (51) employed a simpler solution compared to that reported in this study and in addition to temperature the strength of the hydrogen bonding in water is affected by the concentration of the ions due to changes in the microscopic arrangement of hydrogen bonds in a solution. The exact mechanisms in this process are beyond the scope of this work and an interested reader is referred to the literature (76;77).

In this study ionic strength of NaCl (100mM) was employed as it is similar to the ionic strength of the 2 major classes of brain cells, the neuronal cells (~110 mM) and glial cells (~150 mM) and the solution contained a range of metabolites present in the human brain. Thus the nominal frequency difference (Δ) estimated using the new calibration curve is similar to that measured at ~37.1^{0}C using aqueous solution and temperature controlled phantom and in-vivo MRSI data (see Tables 4.4 and 4.3). The variation in the nominal frequency difference (Δ) anticipated at 37^{0}C, between the two calibration curves presented in this section and the various calibrations obtained using in-vivo samples (Table 2.2, section 2.4) was lower (-0.0103 to 0.0072 ppm) to compared that for aqueous solutions (-0.0220 to 0.0345 ppm). These frequency differences although small may lead to apparent temperature differences of up to ~3^{0}C in MRS temperature estimates (depending on the calibration curve employed). Thus it is necessary to employ tissue mimicking material to account for differences in the ionic content in order to obtain accurate calibration constants (A and B), otherwise the MRS temperature estimates will be inaccurate and extreme care needs to

taken while reporting and comparing MRS temperature estimates from different studies.

Although not investigated here, the fast exchange of the protons between water and macromolecules is reported to influence the frequency difference Δ. As the macromolecular content of the brain tissues (grey and white matter) are different, this fast exchange may produce tissue specific frequency differences. Based on the results from aqueous solutions, Vescovo (51) anticipate at same temperature, $\Delta_{water\text{-}naa}$ measured from white matter regions should be lower than in grey matter regions by ~0.005ppm. This anticipated frequency difference between grey and while matter is smaller compared to 0.015ppm, recently reported by Chadzynski et al. (66) using healthy volunteer MRSI data. These tissue specific differences and differences in the ionic of content of the brain tissues (grey and white) matter may influence in-vivo regional MRSI temperature estimates, producing apparent (and not real) temperature gradients. Thus further validation is necessary in order to obtain accurate calibration curves and to account for tissue specific differences.

4.5 Amplitude of the reference metabolite (NAA)

4.5.1 Introduction

The temperature sensitivity of the proton frequency shift is low (~0.01 ppm/^{0}C), thus robust estimation of the frequency difference (Δ) is crucial for estimation of temperature. Simulation studies indicated the need to obtain lowest linewidth and highest signal noise ratio (SNR) for the metabolite (internal reference) peak to accurately determine the frequency difference (Δ) and thus temperature (44;46). The metabolite linewidths obtain are largely dependent on the effectiveness of shimming procedure and nature of the sample. In contrast, the SNR is largely dependent on the amplitude of the metabolite peak. However a number of factors affect the amplitude of the internal reference metabolite peak (NAA). It is well known that NAA levels vary across different regions of the brain and with age (78), NAA levels are reduced in clinical conditions like stroke and traumatic brain injury. Again, the metabolite amplitude (and thus the SNR) measured from spectra acquired using the same set up (i.e. volunteer, scan settings and data processing) may vary by 17% (79). Thus it is important to assess, how the variation in amplitude of the metabolite signal affects the precision of MRSI temperature mapping. A number of experiments designed to investigate this are discussed in this section.

4.5.2 Methods

In order to determine the effect of varying NAA amplitude on estimating a temperature difference, MRSI scans were acquired using four solutions with different NAA concentrations (Solution A - NAA concentration 30% (3.8mM), Solution B - NAA concentration 50% (6.3mM), Solution C - NAA concentration 75% (9.4mM) and Solution D - NAA concentration 100% (12.5 mM)). These 4 solutions also contained additional metabolites at physiological levels (for details see Table 3.1 section 3.2). MRSI scans were acquired in 4 sessions (one for each NAA level) using the temperature controlled phantom. For each session both metabolites chambers contained the same metabolite solution (i.e. at same NAA concentration). A regional temperature difference (of ~0.5^{0}C) was achieved by setting the two metabolite chambers at different

temperatures (LHS set point 37^0C and RHS set point 37.5^0C) for all scans. In order to determine the repeatability (within the session), 5 MRSI scans were acquired in back to back succession for each session. MRSI acquisition parameters and data processing was same as that discussed in section 4.3.2. The calibration constants (A=102.5 and B=309.5) as reported in Table 4.3 were employed to obtained temperature estimates using NAA as the internal reference from the MRSI data. For simplicity the analysis was limited to one central voxel for both metabolite chambers.

4.5.3 Results

The MRSI temperature estimates and the fibre optic temperature during the scans are reported in Table 4.5. The temperature difference estimated using MRS (Δ_{mrs}) and optical thermometry (Δ_{fo}) are also shown in Table 4.5. The plot of the error (Δ_{mrs} - Δ_{fo}) in the estimation of the temperature difference at different NAA levels is shown in Figure 4.12. The SD of the optical temperature measurements during each scan was less than 0.1^0C for both chambers and indicates excellent temperature stability during the course of the scans. The NAA and the prescan linewidths for the all the scans varied between 1-2 Hz indicating excellent shimming over the field of view.

Solution/ NAA concentration	Scan	LHS			RHS			Temperature Difference (^{0}C) (RHS-LHS)	
		NAA Amplitude (I.U.)	Temperature (^{0}C)		NAA Amplitude (I.U.)	Temperature (^{0}C)			
			MRS	Optical		MRS	Optical	MRS	Optical
Solution A NAA 30% (3.8 mM)	1	74.9	37.06	37.07	68.1	37.77	37.55	0.71	0.48
	2	75.3	36.93	37.08	68.7	37.38	37.56	0.45	0.48
	3	77.9	36.79	37.09	68.6	37.05	37.56	0.27	0.47
	4	73.8	36.97	37.09	67.9	37.40	37.55	0.43	0.46
	5	82.4	36.87	37.09	74.2	37.26	37.56	0.39	0.47
Solution B NAA 50% (6.3 mM)	1	115.1	37.05	37.09	119.0	37.55	37.52	0.50	0.43
	2	117.5	37.05	37.10	110.9	37.58	37.52	0.52	0.42
	3	115.0	37.01	37.10	112.0	37.59	37.51	0.57	0.41
	4	103.9	37.12	37.09	113.8	37.55	37.50	0.43	0.41
	5	122.2	37.00	37.09	113.9	37.67	37.49	0.67	0.40
Solution C NAA 75% (9.4mM)	1	173.6	37.18	37.05	173.3	37.69	37.66	0.51	0.61
	2	176.1	37.12	37.07	176.6	37.64	37.62	0.51	0.55
	3	170.9	37.09	37.07	166.7	37.53	37.56	0.44	0.49
	4	173.8	37.12	37.08	164.8	37.53	37.54	0.41	0.46
	5	181.2	36.99	37.08	170.3	37.39	37.54	0.40	0.46
Solution D NAA 100% (12.5mM)	1	231.7	37.23	37.13	232.1	37.60	37.58	0.37	0.45
	2	223.1	37.11	37.13	221.4	37.51	37.58	0.40	0.45
	3	205.7	37.16	37.11	223.0	37.55	37.60	0.40	0.49
	4	210.1	37.13	37.12	218.6	37.53	37.59	0.40	0.47
	5	227.7	36.98	37.11	220.9	37.44	37.59	0.46	0.48

Table 4.5 MRS and fibre optic temperatures at various levels of the NAA concentrations (also see Figure 4.12).

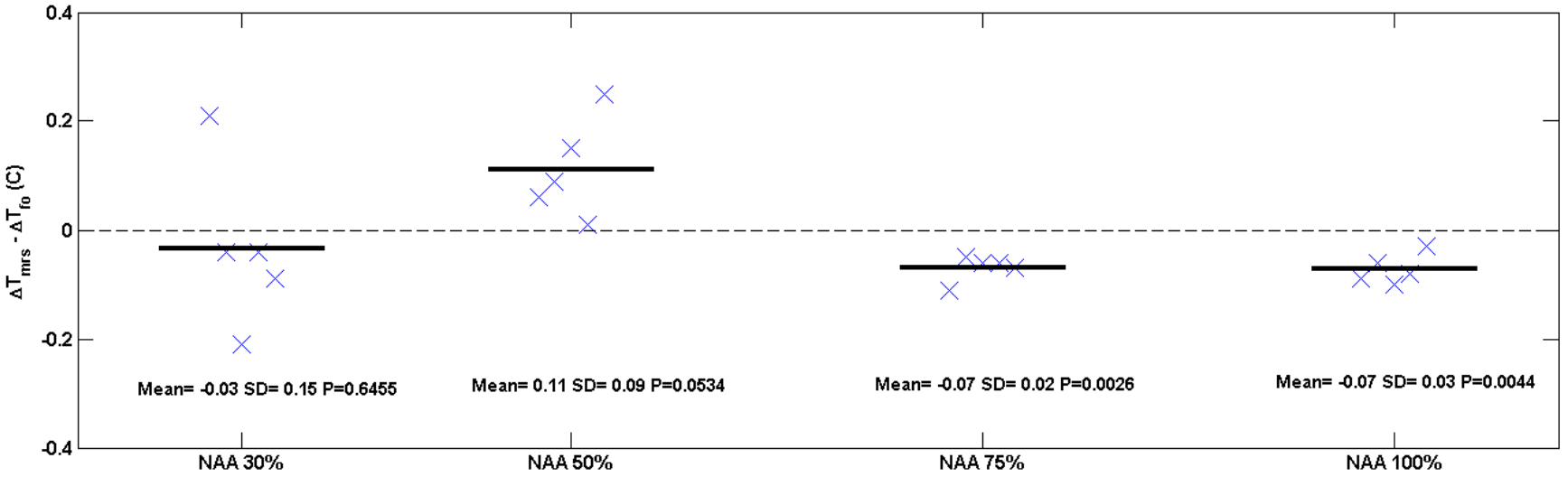

Figure 4.12 Error ($\Delta_{mrs} - \Delta_{fo}$) in the MRS temperature estimation at various levels of the NAA concentration.

4.5.4 Discussion

The results presented in this section confirm a large variation in the MRS temperature estimates at reduced NAA levels (i.e. at NAA concentration 50% or lower). Thus it may be necessary to employ an alterative metabolite (for example choline) as the internal reference in conditions such as stroke, brain tumours and traumatic brain injury where NAA levels may drastically reduce. These results also suggest the nominal regional variation (0-25%) in brain metabolites level encountered in-vivo should not influence MRSI based temperature mapping. It should be noted that the results presented in this section are preliminary and form part of a large study (in collaboration with Dr Michael Thrippleton, PI Prof Ian Marshall), which aims to determine repeatability measurements between sessions and using different scanners (1.5T and 3T). The data acquisition for this study is complete and the near future analysis will include a statistical (general linear model) based approach using all the MRSI voxels to establish inter and intra session repeatability and to check the effect of using different scanners (1.5T versus 3T) and varying NAA amplitude on MRSI temperature mapping.

4.6 Summary

In this chapter construction of a two chamber phantom to be employed for in-vitro validation of MRSI temperature mapping was described. The phantom consists of two chambers with independent temperature control (achieved using 2 water baths) with provisions for monitoring the temperature of the chambers (using optical thermometry) during the scans. The design of the phantom was tailored to achieve excellent temperature control during the scans and excellent shimming could be preformed over the MRSI acquisition volume. The summary of in-vitro validation experiments presented in this chapter using this temperature controlled phantom is as follows

1. The in-vitro experiments confirmed that single scan MRSI temperature mapping could be employed to detect regional temperature variations of as low 0.2^0C.
2. The in-vitro calibration experiments confirmed the calibration constants used to compute temperature are sensitive to the ionic content of the sample. Thus further research is necessary in order to obtain accurate absolute temperature using MRS.
3. The preliminary findings shows decreased reproducibly of the MRS temperature estimates at concentrations of the metabolite peak (used as internal reference) which is less than 75% of the normal physiological level.

5 In-vivo study

5.1 Introduction

A number of studies as summarised in section 2.4, indicate regional brain temperature variations exists. These studies have employed single voxel internal reference MR thermometry. Two studies, one by Marshall et al. (44) for stroke patients and the other by Childs et al. (46) on healthy volunteers have employed MRSI to acquire brain temperature maps. Childs et al. (46) argue the precision of the MRSI temperature maps is worse compared to temperature estimates obtained using single voxel spectroscopy. However extensive in-vitro validation of MRSI temperature mapping presented in previous chapter suggests that MRSI temperature mapping can be employed to estimate small temperature differences (of about ~0.2^0C). Thus the main aim of the work presented in this chapter is to assess whether MRSI can be employed to study regional brain temperature variations.

In section 5.2 MRSI data acquired from 40 healthy elderly volunteers from Lothian birth cohort (LBC) 1936 will be employed to obtain brain temperature maps. A regional analysis will then be performed to identify regional brain temperature variations (if any) and to assess whether the regional brain temperature estimates correlate with structural imaging or cognitive scores. A number of practical considerations to improve MRSI data quality from healthy volunteers will be presented in section 5.3. In section 5.4, the optimized MRSI acquisition protocol was employed to assess regional brain temperature variations in 12 healthy young volunteers, while the repeatability of the MRSI temperature estimates will be assessed in section 5.5.

5.2 Healthy elderly volunteers from LBC 1936

5.2.1 Introduction

It is well known that brain metabolite levels vary across the brain and are different in grey and white matter. Brain metabolite levels are also reported to vary with age (80) and are associated with cognition (81;82). Brain temperature regulation and metabolism are argued to be closely related however the mechanisms of brain temperature regulation and its progression with ageing are not known. At this institution, volunteers from the Lothian birth cohort (LBC) 1936, who were the participants of the Scottish Mental Survey 1947, are being followed for a longitudinal study to characterise changes in brain structure with cognitive abilities (83). As a result a wealth of information on the brain structure and cognitive scoring for these volunteers is readily available. Thus, this population of LBC 1936 represent an ideal cohort to study regional brain temperature variation in healthy ageing. The regional brain temperature estimates from this healthy elderly cohort also provide an ideal baseline to compare the brain temperature variation for stroke and traumatic brain injury patients. Thus MRSI was performed on 40 participants from LBC 1936 in order to assess whether regional brain temperature variations can be identified in this healthy elderly cohort using MRSI data and whether the brain temperature is correlated with structural imaging data and cognitive scores.

5.2.2 Methods

Participants

Forty elderly healthy volunteers (25 women and 15 men) from the Lothian birth cohort 1936, were scanned at the age of 71 years this in pilot study. This cohort of 40 volunteers forms a sub group of 1091 volunteers who participated in a study of brain ageing and cognition and had detailed structural imaging and cognitive scoring available readily (83;84). As brain cognition is related to white matter lesion and brain atrophy scores (85), the participants were selected to have lowest white matter lesion and atrophy ratings. The volunteers gave informed written consent and the study was approved by the local research ethics committee.

MR Examination

MRI and MR spectroscopic imaging (MRSI) were performed on a GE 1.5T HDX clinical research scanner equipped with a quadrature head coil. The imaging protocol included localizer, T_1 and T_2-weighted imaging in addition to MRSI scan. Details of the acquisition parameters are presented in Table 5.1. Total exam time was 30 minutes, which included the planning time. T_2-w images were used to plan a 10mm axial ^{1}H MRSI slice at a level that included basal ganglia. MRSI scan was phase-encoded over a field of view of 240 mm with 24 x 24 encoding steps, producing 1ml voxel resolution. For each phase encode 512 complex data points were acquired at a sampling rate of 1ms i.e. spectral width (1000Hz). Manufacturer provided (first order) automatic shimming was employed to reduce the B_o field inhomogeneity prior to MRSI acquisitions. Water suppression was CHESS based using 3 selective RF pulses with default (manufacturers) setting (bandwidth of RF pulses-75Hz, delay τ between CHESS and PRESS-48ms). Outer volume pre-saturation using 4 saturation bands for lipid artifact suppression was employed.

In order to avoid confounding effects from daily variations in temperature all scans were performed at the same time of day (between 11am-1pm), after equilibration of the participant to room temperature (22^0C) for at least an hour before the scans. Sublingual and aural temperatures were measured immediately before and after each scan as a check on the stability of the participants core temperature.

Coil	Quadrature coil		
Scan number	1	2	3
Sequence	T_1^+	T_2 (FSE)	MRSI (2D PRESS)
Orientation	Coronal	Axial	Axial
TE (ms)	4	105	145
TR (ms)	10	11320	1000
TI (ms)	500		
FOV (mm^2)	256	256	240
Slice thickness (mm)	1.3	2	10
Voxel Volume (mm^3)	1.3	2	1 (cm^3)
Slice gap (mm)	0	0	NA
Matrix	192 x 192*	256 x 256	24 x 24
Number of slices	160	78	1
Options			τ=48ms, 4 (A,P,L,R) Sat Bands Spectral width 1000Hz 512 samples
Acquisition time (minutes.seconds)	8.08	5.06	9.40

Table 5.1 Data acquisition protocol to study brain temperature variations in healthy elderly volunteers (from LBC1936) +3D IR-GRE (Inversion recovery-gradient echo), *zero filled to 256x256.

MRS and Imaging Processing

The MRSI data were processed in the standardised manner as discussed in section 2.5.2 to obtain metabolite maps and temperature maps. Tissue segmentation (CSF only) maps were computed from T_2-w image using the FSL-FAST (FMRIB, Oxford, UK; http://www.fmrib.ox.ac.uk) algorithm. The tissue segmentation (CSF map), temperature and metabolites maps were then overlaid on the T_2 weighted image. The main data processing steps are shown in Figure 5.1. For each spectroscopy voxel the percentage CSF content was calculated. Spectroscopy voxels were rejected if the linewidth of NAA peak was greater than 10 Hz or if the voxel contained more than 20% CSF. To identify any temperature difference between core and outer structures of the brain, the voxels within the VOI were categorised in two regions. The voxels from the central brain structures were classified as 'core' while the voxels in the subcortical/cortical regions were classified 'peripheral/outer' as shown in Figure 5.2. Mean and SD of the temperature in

each region was computed and a paired t-test was performed to determine if the regional temperatures differed significantly.

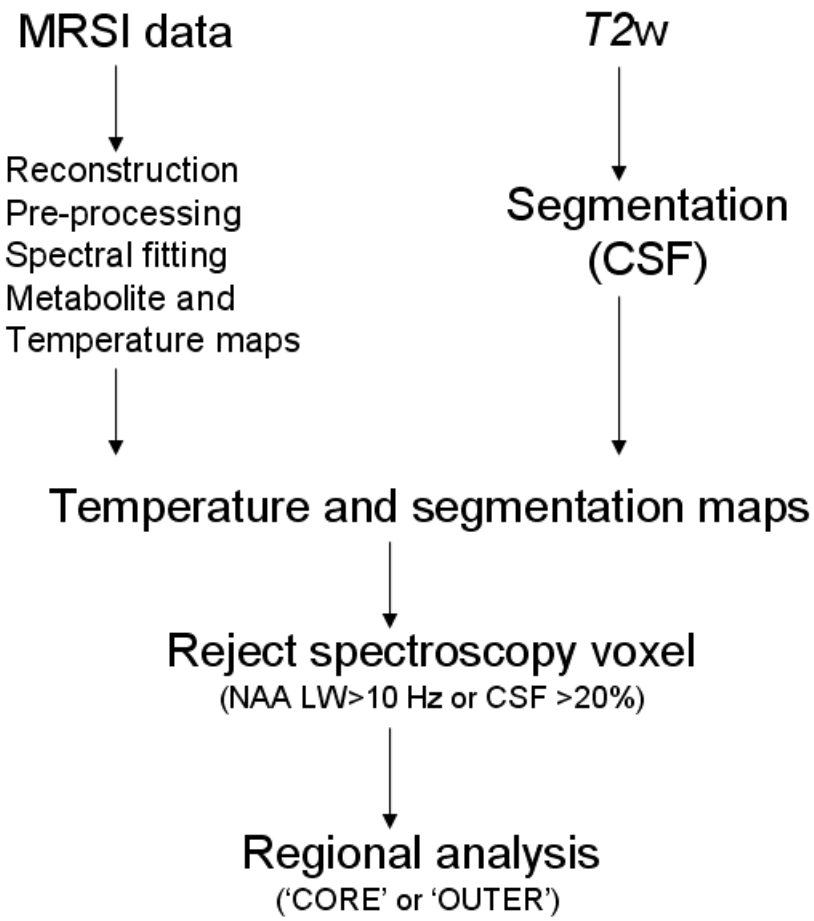

Figure 5.1 Data processing steps to obtain regional brain temperature estimates using MRSI and structural imaging data.

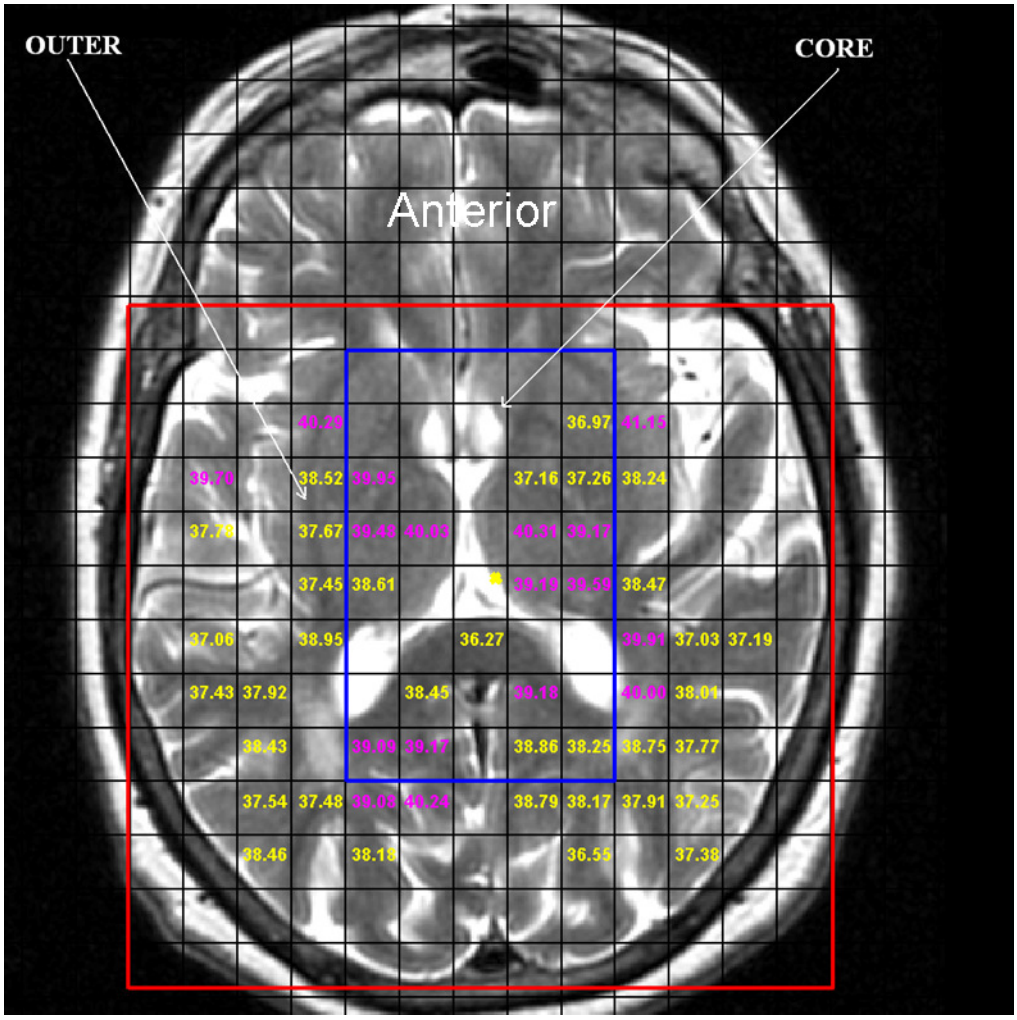

Figure 5.2 Temperature estimates and MRSI grid overlaid on the T_2 weighted image to define core and outer regions of the brain at the level of the basal ganglia. The voxels are colour coded based on the estimated temperature (T), (T<36^{0}C=Cyan, T>39^{0}C=Pink, 36^{0}C <T<39^{0}C=Yellow).

5.2.3 Results

The average percentage of MRSI voxels (for each MRSI dataset) rejected from the analysis based on the quality assurance criteria (NAA LW>10 Hz and voxels CSF content >20%) are shown in Table 5.2. For the 40 subjects, on an average 80% voxels were rejected from each MRSI dataset. Based on the percentage of the voxels rejected for each MRSI dataset, the 40 MRSI datasets were sub-divided into two sub groups (sub-group A with 27 volunteers and sub-group B with 13 volunteers). The average percentage of voxels (per MRSI dataset) rejected from the analysis for both subject groups are also shown in Table 5.2. It was seen that on an average for the 13 volunteers from sub-group B around 90% of the acquired MRSI data was rejected, thus due to rejection of large number of voxels these 13 datasets were excluded from the analysis.

Loss of Voxels (%)			
Group	NAA LW >10 Hz	Voxel CSF >20%	Total
SUB GROUP A (N=27)	55.8	17.0	72.92
SUB GROUP B (N=13)	83.7	6.0	89.79
ALL SUBJECTS (N=40)	69.8	11.5	81.35

Table 5.2 Average percentage of voxels (per MRSI dataset) rejected from the analysis in the LBC study.

The mean and standard deviation (SD) of the regional temperature estimates obtained using the MRSI data from the 27 subjects of sub-group A are reported in Table 5.3. The average values of the mean core temperature and mean outer temperature for these 27 subjects were 38.56^0C (SD 0.85^0C) and 38.21^0C (0.49^0C). The average temperature difference was 0.35^0C (SD 0.89^0C), indicating the 'core' or central brain structures to be warmer than 'outer' cortical or sub-cortical structures as shown in Table 5.4. However this was not significantly different from zero (P=0.051; paried t-test). The plot of temperature difference estimated by subtracting mean outer temperature from mean core temperature on a subject by subject basis is shown in Figure 5.3. The mean temperature difference for the 11 males was lower compared to that obtained from 16 females in this sub-group as shown in Table 5.4.

Subject	Core Temperature (^{0}C)		Outer Temperature (^{0}C)		Global Temperature (^{0}C)		Temperature difference (^{0}C)
	Mean	SD	Mean	SD	Mean	SD	(Core-Outer)
1*	38.00	1.42	37.96	1.81	37.97	1.72	0.04
2	38.51	1.93	38.88	1.45	38.79	1.56	-0.36
3*	38.35	1.92	38.38	1.75	38.37	1.77	-0.03
4*	37.32	1.87	37.76	1.53	37.67	1.60	-0.44
5*	38.78	1.11	38.46	2.08	38.53	1.90	0.31
6*	39.48	1.58	37.51	1.45	38.21	1.75	1.97
7	38.60	1.58	38.05	1.76	38.22	1.71	0.54
8	38.22	1.68	38.48	2.04	38.41	1.94	-0.26
9	38.15	1.91	38.73	2.30	38.55	2.16	-0.58
10	36.89	2.10	37.57	2.06	37.40	2.06	-0.68
11*	38.08	1.11	37.45	1.60	37.68	1.45	0.64
12	39.93	1.15	38.50	1.68	38.91	1.66	1.43
13*	38.22	1.88	38.12	1.68	38.14	1.70	0.10
14*	39.16	1.78	39.14	1.56	39.15	1.62	0.02
15	38.72	1.14	38.33	1.09	38.47	1.12	0.40
16	39.15	1.03	38.68	1.11	38.82	1.10	0.47
17	38.78	1.40	38.42	2.14	38.54	1.91	0.36
18	38.58	2.18	38.31	1.56	38.41	1.78	0.27
19*	37.11	2.27	38.61	1.74	38.12	2.03	-1.50
20	38.53	0.79	37.41	1.31	37.67	1.29	1.12
21*	37.06	2.43	38.29	1.92	38.05	2.07	-1.23
22	39.28	2.94	37.91	1.77	38.09	1.92	1.37
23*	39.46	1.17	38.66	1.77	38.85	1.67	0.81
24	38.60	1.31	38.05	1.41	38.13	1.39	0.54
25	39.31	1.83	38.83	1.22	38.97	1.42	0.48
26	38.68	1.08	37.39	1.46	37.84	1.46	1.29
27	40.43	1.56	37.98	1.33	38.31	1.59	2.45

Table 5.3 Mean and SD of regional MRSI temperature estimates from 27 elderly volunteers from the LBC1936. *indicates male volunteers (for summary see Table 5.4).

	Core Temperature		Outer Temperature		Global Temperature		Temperature Difference		
Subject	Mean (^{0}C)	SD (^{0}C)	Mean (^{0}C)	SD (^{0}C)	Mean (^{0}C)	SD (^{0}C)	Mean (^{0}C)	SD (^{0}C)	P
Group A (N=27)	38.57	1.64	38.22	1.65	38.31	1.68	0.35	0.90	0.051
Males (N=11)	38.27	0.88	38.21	0.52	38.25	0.46	0.06	0.95	0.831
Females (N=16)	38.77	0.78	38.22	0.48	38.35	0.44	0.55	0.83	0.018

Table 5.4 Mean and SD of the temperature estimates reported in Table 5.3, also see Figure 5.3.

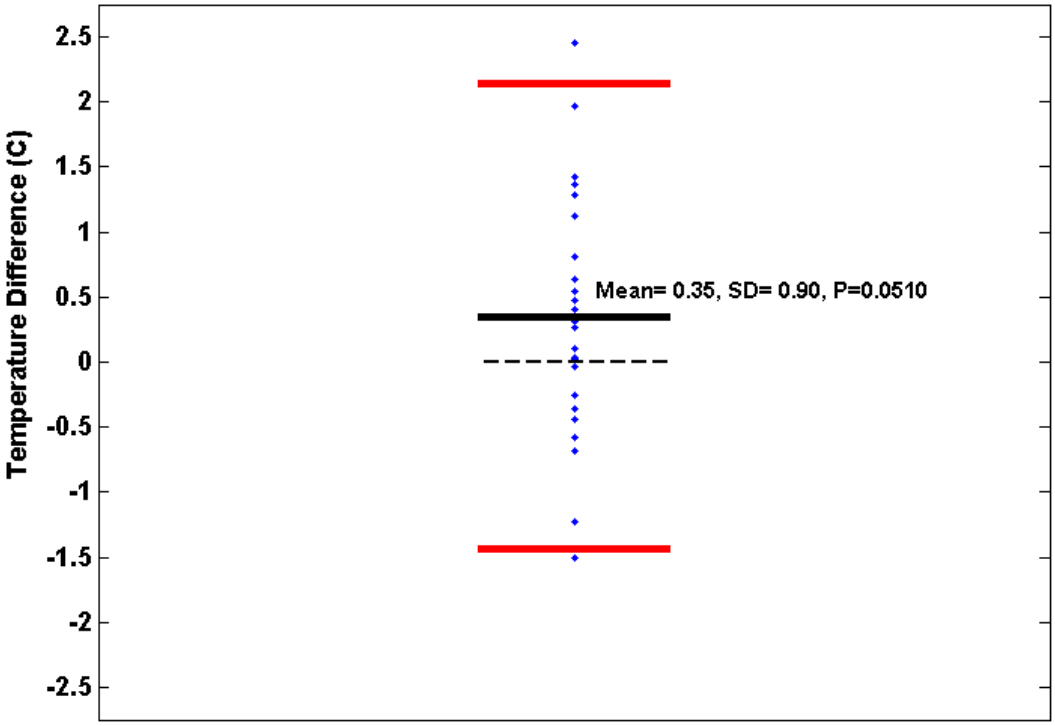

Figure 5.3 Plot of regional temperature difference (core-outer) for each of the 27 subjects reported in Table 5.3. Also shown are mean and (mean ± 2*SD).

The average values of the aural and sublingual temperature measured for these 27 subjects before and after scan are shown in Table 5.5. A slight (~0.2^{0}C) reduction in the aural and oral temperatures is observed during the scans. The temperature estimates for different levels of atrophy and white matter ratings are shown in Tables 5.6 and 5.7 respectively. It is seen that the temperature difference varies with the white matter rating (determined using

the Fazekas scale, for information on Fazekas scale see reference ((86)) and brain atrophy scores, but they were not significantly different from zero (P>0.05) as the spread of the temperature estimates was large.

Number of Subject=27	Aural Temperature (^{0}C)		Oral Temperature (^{0}C)	
	Before Scans	After Scans	Before Scans	After Scans
Mean	36.40	36.17	36.29	36.07
SD	0.35	0.26	0.23	0.37

Table 5.5 The mean and SD of the aural and sub-lingual (oral) temperatures measured before and after the scans for the 27 volunteers.

WM rating (Fazekas Scoring)	Subjects	Global Temperature (^{0}C)	Temperature difference (^{0}C)
1	20	38.31 (0.44)	0.35 (0.89)*
2	7	38.32 (0.45)	0.21 (0.85)*

Table 5.6 Mean (SD) of MRSI temperature estimate and the temperature differences between core and outer regions of the brain at different level of white matter rating (based on Fazekas scores) * P>0.05

Atrophy Rating	Subjects	Global Temperature (^{0}C)	Temperature difference (^{0}C)
1	3	38.32 (0.47)	0.38 (0.94)*
2	8	38.31 (0.45)	0.27 (0.81)*
3	15	38.34 (0.45)	0.24 (0.81)*

Table 5.7 Mean (SD) of MRSI temperature estimate and the temperature differences between core and outer regions of the brain Mean (SD) of MRSI temperature estimate at different level of brain atrophy ratings (Brain atrophy increases with rating). *P>0.05

	gFactor	gSpeed	gMemory
Mean CORE Temperature	-0.046	-0.017	-0.048
Mean Outer Temperature	-0.160	-0.025	-0.241
Mean Global Temperature	-0.038	0.03	-0.030

Table 5.8 Pearson's correlation (R) for general cognitive scores (gFactor, gSpeed and gMemory) and various brain temperature estimates. There is no evidence of correlation (P>0.05 (non significant) for all cases) of brain temperature with any of the cognitive scores.

5.2.4 Discussion

In this study MRSI data acquired from healthy elderly volunteers was employed to investigate regional brain temperature variations. It was found that the deeper structures of the brain on average were warmer compared to superficial regions. However, the spread of this temperature gradient (per subject) was large as shown in Figure 5.3. Thus it was not possible to add statistical confidence to the regional temperature differences. Rejection of a large proportion of the acquired voxels was the main drawback in this study. Thus the attempt to correlate temperature estimates to structural imaging and cognitive scores was not successful.

MRSI slice location in this study includes the metabolically active region of the basal ganglia to maximize the chances of identifying regional brain temperature differences, as basal ganglia is centrally located in the brain and major cerebral vessels are located at this level. However, at this slice location we are bound to include air cavities from the frontal sinuses. There is also increasing evidence of iron deposits in basal ganglia in these subjects (87). The increased susceptibility effects from the air cavities and iron deposits directly affect shimming and thus the B_o homogeneity. As a result better quality of data were obtained for scans where the spectroscopy VOI (PRESS box) avoids anterior regions of the brain, as shown in Figure 5.4. The average

prescan linewidth obtained after automatic shimming in sub group B of 13 subjects that were excluded from the analysis was higher (16.92 Hz SD (3.96 Hz)) compared to that of the 27 subjects (13.78 Hz SD (3.91 Hz)) retained in the analysis. Other factors such as higher atrophy scores in this elderly cohort and motion during the scans may influence MRSI data quality. In this study the majority of the subjects retained in the analysis had higher brain atrophy scores as shown in Table 5.7, thus atrophy cannot be considered as the primary deterrent while performing MRSI in an elderly cohort. The scan time of 30 minutes was reasonably short compared to 70 minutes for the structural imaging scanning sessions in which these volunteers had previously participated.

The exact cause and the modalities to reduce the systematic error in MRSI temperature maps (as discussed in chapter 3) were not identified from the onset of data collection for this study. Thus MRSI data were acquired using strong water suppression setting (i.e. τ=48ms) with an intention to apply correction for this systematic error during data processing. However the results presented in chapter 3 demonstrate that this systematic error was dependent on the water suppression setting employed to acquire the MRSI data. This error cannot be corrected during data processing, as it is necessary to acquire MRSI data using weak water suppression setting (by increasing τ to 68ms) to reduce this error. Thus the confounding effects from the systematic error in regional temperature estimates cannot be completely ruled out in this study. In this study aural and sub-lingual temperatures varied between 35.0^{0}C and 37.1^{0}C, indicating that the brain temperature may be higher than the core body temperature. However, these differences may be due to calibration/tissue specific effects as discussed in chapter 4 and thus further validation is necessary.

It should also be noted that, although T_1 weighted images are widely used for segmentation, in this study T_2 weighted images were employed for segmentation as it was challenging to obtain a good brain mask using the automated FSL tool (BET) from T_1 images for these volunteers. Due to rejection of higher a proportion of MRSI voxels (based of NAA LW>10 Hz) a

tissue specific temperature analysis was not feasible and thus in this study T_2 weighted images were employed, with the aim of accurately delineate CSF structures.

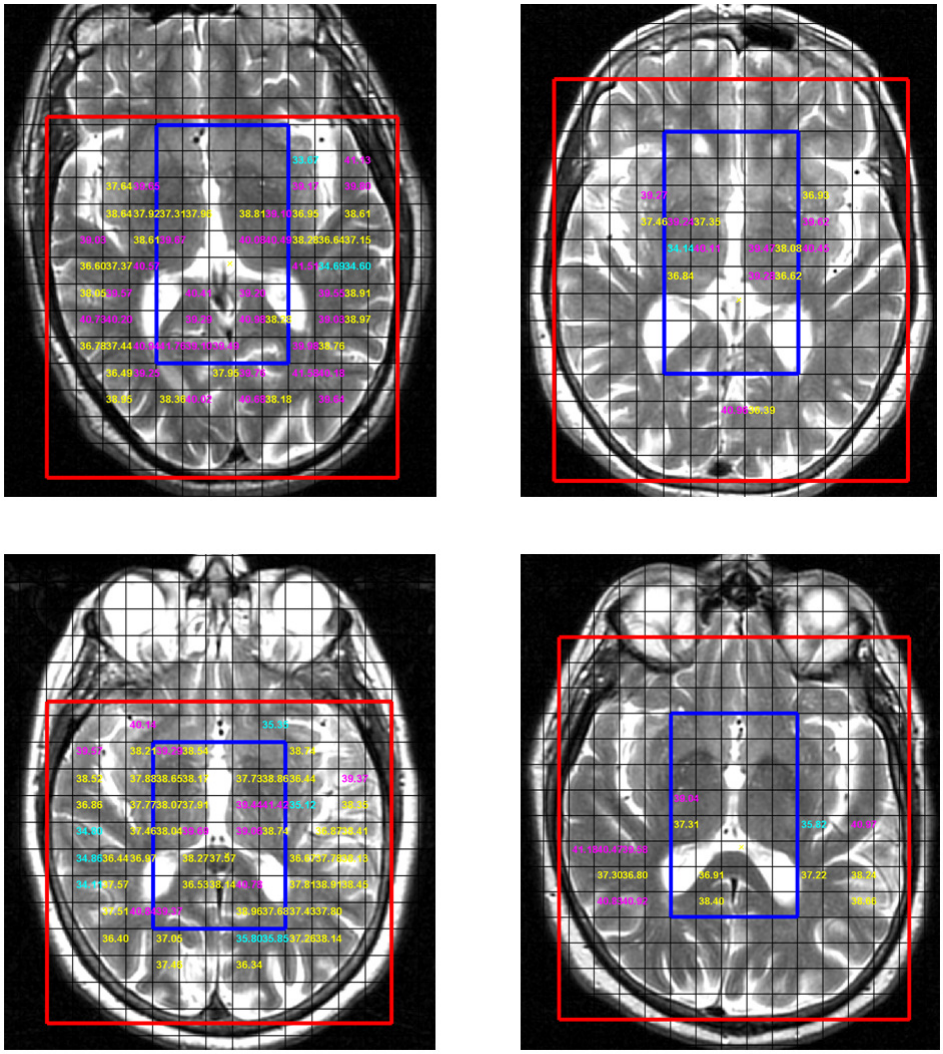

Figure 5.4 Examples of varying the slice location and the PRESS box (VOI shown in red outline) on the MRSI data. The MRSI temperature estimates are overlaid on the T_2 w image. The data sets in the left column contain a relatively large number of valid voxels (rejected voxels are not shown) compared to dataset shown in right column as the anterior edge of the VOI is limited to exclude sinuses.

5.3 Optimization of the MRSI data quality

5.3.1 Introduction

Acquiring good quality MRSI data is central to identify regional brain temperature variations. The main problem in obtaining good quality MRSI data is shimming. In the previous study automatic first order shimming was used to minimize B_o field homogeneities in the x, y and z direction. The increasing usage of higher field strength scanners (3T or higher) leads to a number of advanced shimming techniques have being reported (29;74;75;88). These advanced approaches require additional hardware (i.e. shim coils, amplifiers etc.) and cannot be readily implemented in the current set-up. Thus in order to improve MRSI data quality, optimising MRSI slice positioning to reduce susceptibility difference between air and brain tissue was investigated and is discussed in the following paragraphs.

5.3.2 Methods and results

MRSI data were acquired at different axial slices levels (of the basal ganglia (BG) and corpus callosum (CC)) as shown in Figure 5.5 from two healthy young (aged 33 and 26 years) volunteers using the same acquisition protocol as discussed in section 5.2.2. MRSI data processing to obtain temperature maps was similar to that previously discussed in section 2.5. Voxels were rejected only if NAA linewidth was greater than 10 Hz. Examples of temperature maps (from one volunteer) at the levels of the basal ganglia and corpus callosum are shown in Figure 5.6. The prescan linewidths obtained were smaller (6 and 5 Hz) at the level of corpus callosum compared to that obtained at the level of basal ganglia (12 and 14 Hz). The mean (SD) of the temperature and metabolite (NAA) linewidth estimates and number of voxel rejected from analysis are reported in the Table 5.9. The NAA linewidths at the level of corpus callosum were low compared to those obtained at the level of basal ganglia due to improved shimming and thus a lower proportion of voxels were rejected form the analysis. As result of lower NAA linewidths, the variation in the MRSI temperature estimates reduces at the level of the corpus callosum.

Volunteer	Slice location	Temperature (^{0}C)	NAA LW (Hz)	Voxels rejected (%)
1	BG	37.95 (1.0)	6.18 (1.81)	47
1	CC	37. 68 (0.83)	4.03 (1.0)	25
2	BG	37.6 (1.3)	7.2 (1.97)	49
2	CC	37.38 (0.93)	5.01 (1.1)	23

Table 5.9 MRSI temperature estimates (Mean (SD)), NAA linewidth and percentage of voxels rejected based on quality assurance criteria (NAA Linewidth>10Hz) at the two slice levels (BG- Basal Ganglia, CC- Corpus callosum).

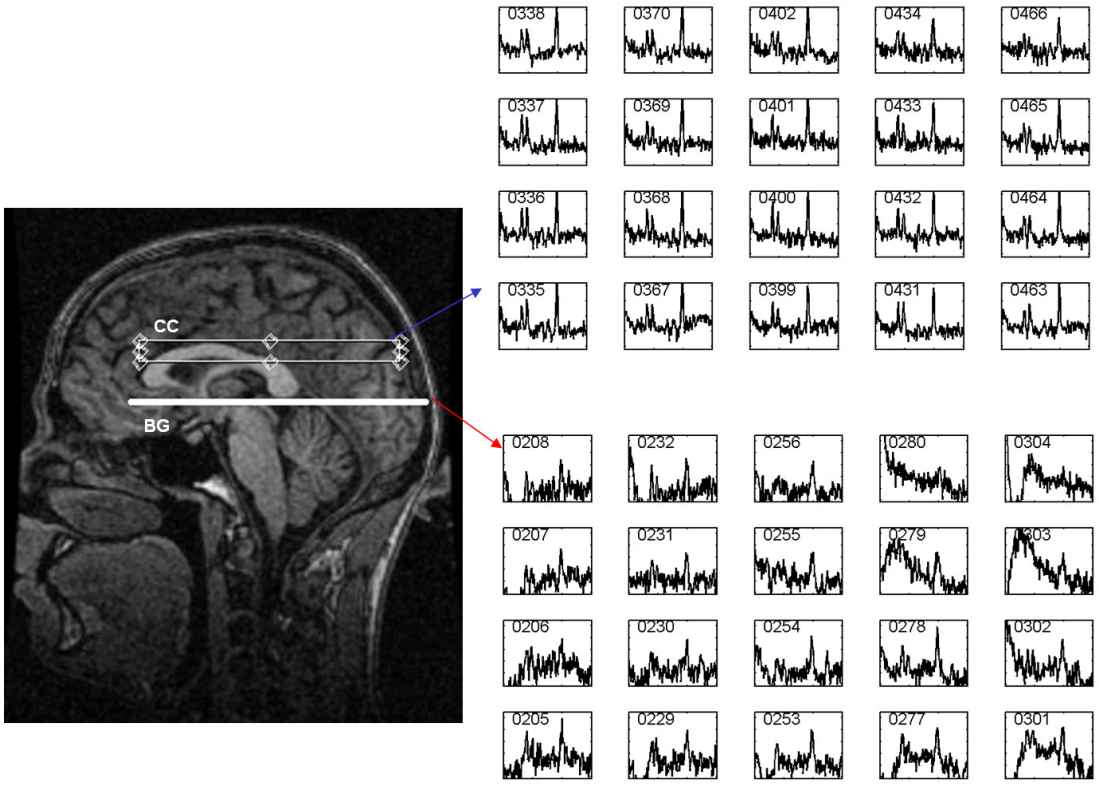

Figure 5.5 Demonstration of the axial slice locations used to obtain MRSI data, also shown are array of MRSI data at two (CC and BG) slice levels from a healthy male volunteer. A marked improvement can be observed in spectral quality in the data acquired from CC.

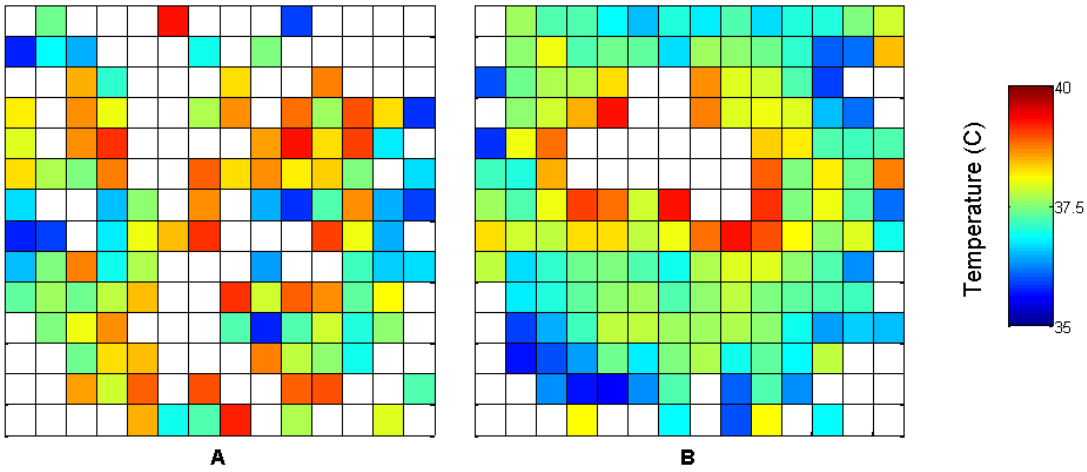

Figure 5.6 Illustrative temperature maps from one healthy volunteer acquired at the level of Basal Ganglia (A) and Corpus Callosum (B) (shown in white are the voxels rejected as the NAA linewidth >10Hz).

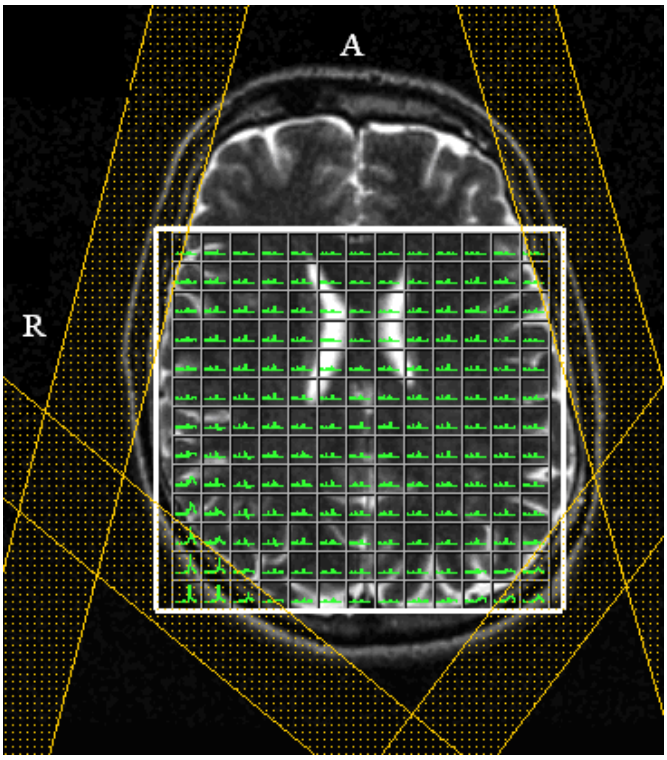

Figure 5.7 MRSI VOI positioning at the slice location of Corpus Callosum.

5.3.3 Discussion

The effect of optimization of slice positioning on the MRSI data quality was investigated. Using a higher slice location (CC) results in improved shimming and MRSI data quality and increases the number of voxels available for regional temperature analysis by 25%. In this study the VOI at the level of corpus callosum was defined by limiting anterior boundary to the genu of corpus callosum and the other (posterior, right and left) boundaries to the edge of the brain as shown in Figure 5.7. Thus anatomical landmarks can be used for consistent slice positioning and to avoid frontal sinuses being included in the MRSI VOI, which may compromise shimming due to increased susceptibility difference. Again the corpus callosum is located centrally in the brain and is close to the highly per fused metabolically active region of the basal ganglia and thus can be used to determine brain temperature variations.

5.4 Healthy young male volunteers

5.4.1 Introduction and methods

In this section the optimized MRSI protocol will be employed to assess regional brain temperature variations. MRSI data at the slice location of the corpus callosum were acquired as discussed using a protocol as discussed in the previous section from 12 healthy young male volunteers (mean age 32 years SD 5 years, range 24-41 years). The MRSI slice positioning was determined using the additional T_2 and T_1 weighted scans, the PRESS box was limited to include the edges of left, right and posterior regions of the brain as shown in Figure 5.7, while the anterior edge was limited to genus of the corpus callosum as shown in Figure 5.5. The detailed MR imaging protocol is as shown in Table 5.10. Four MRSI scans were acquired for each subject to assess the within session repeatability of MRSI temperature mapping. Water suppression was weakened by increasing the delay τ from the default value of 48 ms to 68 ms to reduce systematic errors in temperature maps as previously discussed. The 12 volunteers were recruited by Dr Michael Thrippleton as a part of a larger study to validate MRSI temperature mapping funded by the Chief Scientist Office, Scotland. The author assisted Dr Thrippleton in MRSI data collection and setting up the MRSI protocol. The author performed the analysis presented in this section.

Coil	Quadrature coil			
Scan number	1	2	3/4/5/6	7
Sequence	T_1^+	T_2 (FSE)	MRSI	T_2* (GRE)
Orientation	Coronal	Axial	Axial	Axial
TE (ms)	4	102	145	15
TR (ms)	10	11320	1000	940
TI (ms)	500			
FOV (mm^2)	256	256	300	256
Slice thickness (mm)	1.3	2	10	2
Voxel Volume (mm^3)	1.3	21	0.85 (cm^3)	1
Slice gap (mm)	0	0	NA	0
Matrix	192 x 192	256 x 256	24 x 24 Interpolated to 32 x 32	256 x192
Number of slices	160	78	1	78
Options			τ=68ms (weak WS) Spectral width 1000Hz No. of Sample 512	
Acquisition time (minutes.seconds)	8.08	5.06	9.40	6.09

Table 5.10 Data acquisition protocol to identify regional brain temperature variation from young healthy volunteers. $^+$3D IR-GRE.

MRSI data processing for all the 4 scans was similar to that described in section 5.2.2. The additional T_2* images were used to obtain accurate brain masks using automated FSL tool (BET) (FMRIB, Oxford, UK; *http://www.fmrib.ox.ac.uk*) and brain masks were then used to extract the brain from the T_1 weighted images. The brain extracted T_1 weighted images were segmented using the FSL algorithm FAST as shown in Figure 5.8.

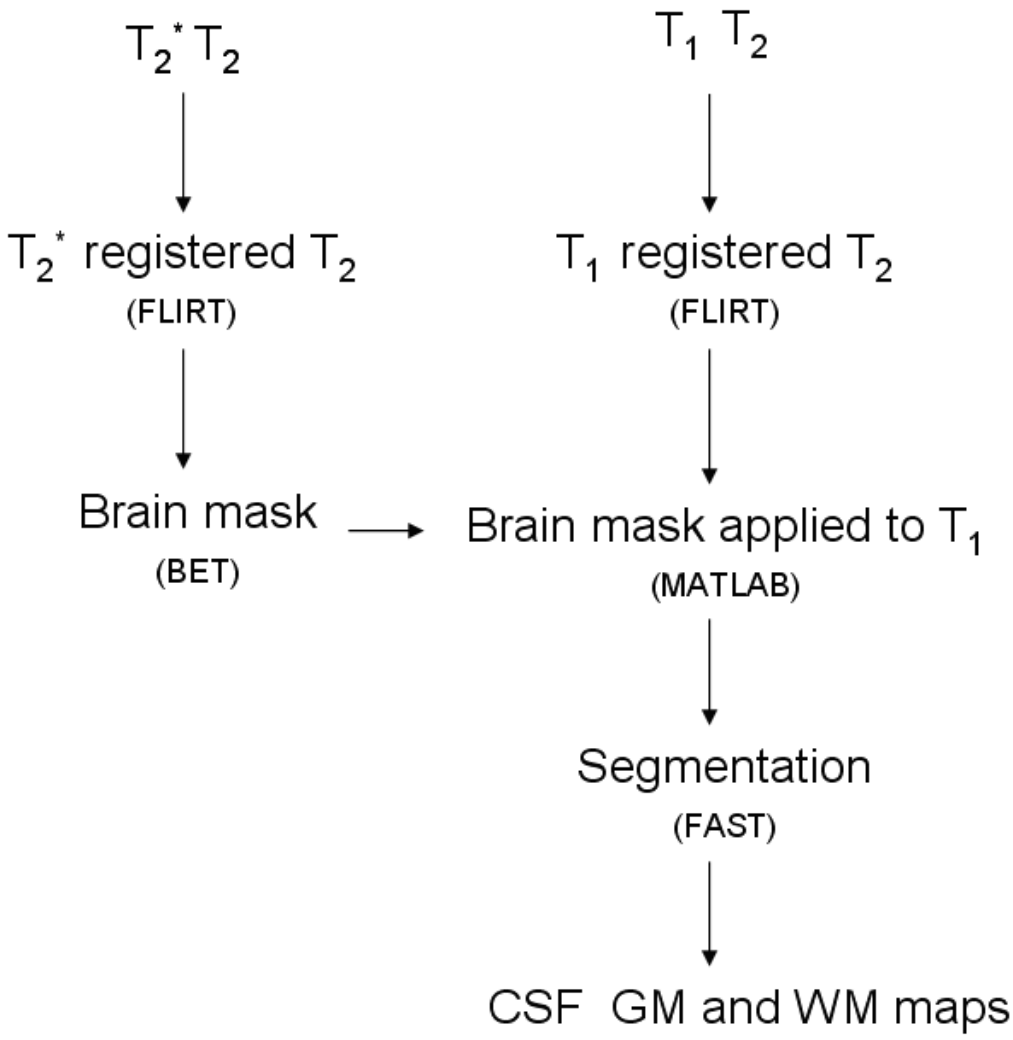

Figure 5.8 Flowchart illustrating steps for segmenting brain from structural imaging scans using FSL libraries.

The CSF, grey matter (GM) and white matter (WM) maps obtained using segmentation, and the temperature maps were then overlaid on the T_2 weighted image as shown in Figure 5.9. For each spectroscopy voxel, percentage CSF, grey matter and white matter content were calculated and a final classification based on the majority tissue type (i.e. CSF, GM or WM) was assigned as shown in Figure 5.9. The spectra were visually assessed for spectral quality and poor spectra were rejected from the analysis. Core and outer regions of the brain were determined as shown in Figure 5.9 to perform regional analysis. Two analyses were performed with different filters based on tissue composition. For the first analysis, in addition to spectral quality, spectra were rejected if the NAA linewidths were greater than 10 Hz or if the voxel contained more than 20% CSF. For the second analysis, in addition to

spectral quality and NAA linewidth, voxels containing more than 10% CSF and less than 85% WM were rejected to avoid any tissue specific or calibration effects as discussed in section 4.4. The analyses reported in this section were performed using the first MRSI scan. The subsequent MRSI scans (scans 2, 3 and 4) were processed using the same processing pipeline, in order to assess repeatability of MRSI based temperature mapping and will be discussed in section 5.5.

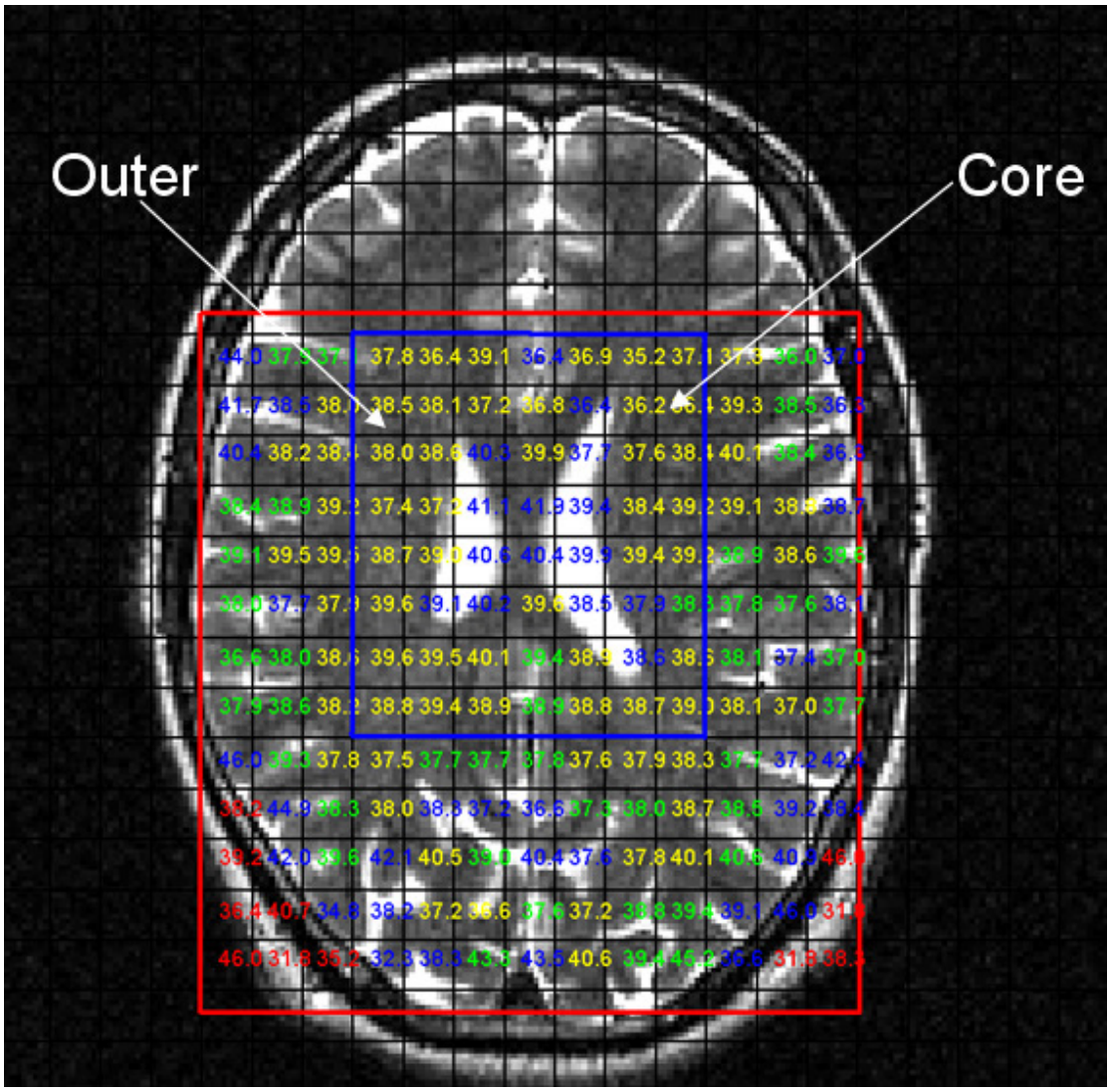

Figure 5.9 Temperature map and the tissue segmentation maps for a young healthy male volunteer overlaid on the T_2 weighed image. The voxels are colour coded based on the majority tissue type, (yellow=GM, green=WM, blue=CSF, red=background).

5.4.2 Results

5.4.2.1 Analysis 1 (CSF < 20% and NAA Linewidth < 10Hz)

The percentage of MRSI voxels rejected based on spectral quality is shown in Table 5.11, while the regional temperature estimates are reported in Table 5.12 The average prescan linewidh after shimming for these volunteers was 10 Hz (SD 2.2 Hz) and was lower compared to 13.78Hz SD (3.91 Hz) obtained for the LBC study presented in section 5.2. The mean temperature difference between the core and outer regions of the brain for these 12 volunteers was 0.32 ^{0}C (SD 0.28 ^{0}C), P=0.002 (paired t-test), and indicates that the core brain temperature is higher compared to the temperature of the exterior brain regions.

Percentage Loss of Voxels			
	Spectral Quality	CSF>20%	Total
12 Subjects	34.8	11.8	46.62

Table 5.11 Voxels rejected from the analysis based on the spectral quality and the CSF content.

Subject	Core Temperature (^{0}C) Mean	SD	Outer Temperature (^{0}C) Mean	SD	Global Temperature (^{0}C) Mean	SD	Temperature Difference (^{0}C) (core-outer)
1	38.19	1.51	37.91	0.69	38.01	1.05	0.28
2	38.23	1.02	37.96	0.73	38.05	0.84	0.27
3	38.67	1.00	38.01	0.61	38.18	0.78	0.66
4	38.25	0.74	37.76	0.69	37.91	0.74	0.49
5	38.18	0.92	37.46	0.76	37.78	0.90	0.72
6	38.03	1.10	37.89	0.92	37.93	0.98	0.14
7	38.54	0.84	38.08	0.68	38.25	0.77	0.46
8	38.55	0.99	38.27	0.84	38.38	0.91	0.28
9	37.62	0.80	37.63	0.68	37.63	0.71	-0.01
10	37.71	0.82	37.95	1.49	37.88	1.33	-0.24
11	38.54	1.21	38.36	1.00	38.41	1.06	0.19
12	38.32	0.94	37.70	0.66	37.86	0.78	0.62

Table 5.12 The regional MRSI temperature estimates on subject by subject basis for 12 healthy volunteers for Analysis 1 (i.e. voxels with CSF < 20% and NAA Linewidth < 10Hz)

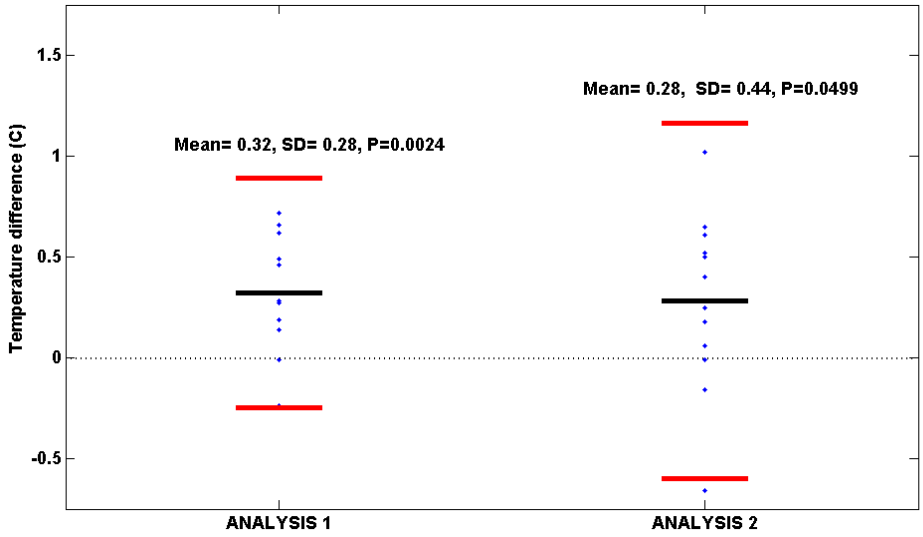

Figure 5.10 The distribution of the temperature difference (core-outer) for 12 healthy young male volunteers for the two analyses, also shown is mean (in black) and mean ± 2*SD (in red).

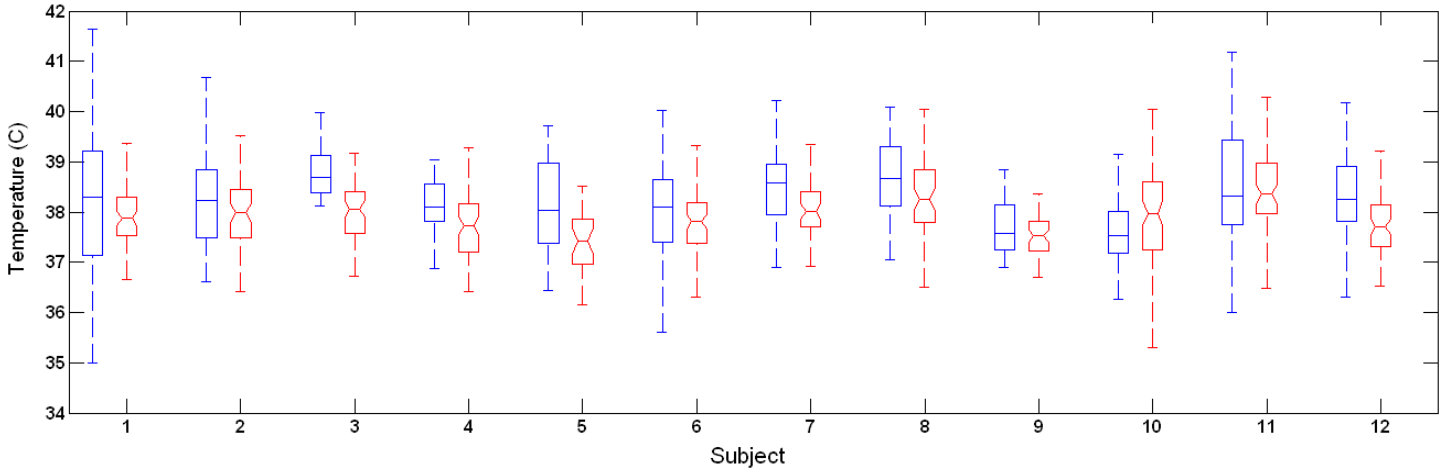

Figure 5.11 Box plots of the Core (shown in blue) and Outer (shown in red) temperature estimates for 12 volunteers for Analysis 1.

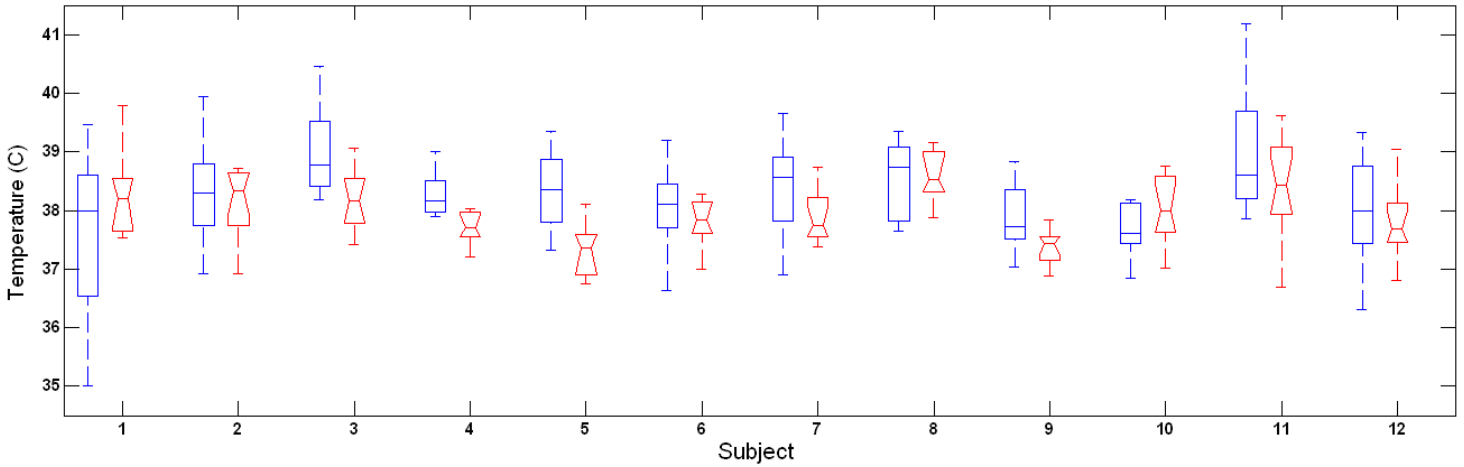

Figure 5.12 Box plots of the Core (shown in blue) and Outer (shown in red) temperature estimates for 12 volunteers for Analysis 2.

5.4.2.2 Analysis 2 (WM>85% CSF <10% and NAA linewidth <10Hz)

Regional Temperature estimates for second analysis are reported in Table 5.13 and the box plots for the temperature estimates of the two regions (core and outer) for these 12 subjects are shown in Figure 5.12. For this analysis the mean core temperature was 38.26 ^{0}C (SD 0.40 ^{0}C), while the mean outer temperature was 37.97 ^{0}C (SD 0.38 ^{0}C), producing a mean temperature difference of 0.28 ^{0}C (SD 0.44 ^{0}C), P=0.050 (paired t-test). The average percentage of voxels included for each subject in this analysis was 13% (SD 1.6%), this included 7.4 % (SD 1.4%) for the core region and 5.5% (SD 1.8%) for the outer regions of the brain and this percentage of voxels retained in this analysis is lower compared to 54% of the voxels retained for the Analysis 1.

	Core Temperature (^{0}C)		Outer Temperature (^{0}C)		Global Temperature (^{0}C)		Temperature Difference (^{0}C)
Subject	Mean	SD	Mean	SD	Mean	SD	(core-outer)
1	37.60	1.39	38.26	0.75	37.81	1.25	-0.66
2	38.33	0.79	38.15	0.59	38.25	0.70	0.18
3	38.83	1.02	38.18	0.50	38.56	0.89	0.65
4	38.26	0.38	37.86	0.62	38.10	0.52	0.40
5	38.33	0.70	37.32	0.52	37.91	0.80	1.02
6	38.08	1.10	38.02	0.88	38.06	1.01	0.06
7	38.38	0.71	37.88	0.44	38.19	0.66	0.50
8	38.42	0.97	38.58	0.46	38.47	0.83	-0.16
9	37.89	0.58	37.37	0.31	37.67	0.55	0.52
10	37.91	0.88	37.92	0.78	37.92	0.81	-0.01
11	39.03	1.12	38.41	0.77	38.67	0.96	0.61
12	38.00	0.88	37.75	0.57	37.87	0.74	0.25

Table 5.13 The regional temperature estimates for the 12 healthy volunteers for Analysis 2 (i.e. Voxels with WM>85% CSF <10% and NAA linewidth <10Hz), (Also see Figure 5.10).

5.4.3 Discussion

Optimizing the slice positioning improved shimming and thus improved the MRSI data quality in this study. The average percentage of the voxels rejected based on the spectral quality was lower compared to that for the elderly volunteers from the LBC 1936 (34.8% versus 55.8%) as shown in Table 5.11 and 5.2 respectively. The improved data quality increases the confidence for determining regional brain temperature variations and suggests that the central regions of the brain are at a higher temperature compared to the peripheral structures by ~0.32^0C. These observations are similar to the surface to deeper brain temperature gradients of 0.3^0C reported by Shiloh et al. (8) and 0.25^0C reported by Childs et al. (46) using single voxel spectroscopy.

In this study the scope of systematic errors in temperature maps was reduced by employing weak water suppression (τ=68ms) as previously discussed in chapter 3. However recent report by Chadzynski et al. (66) suggests frequency difference between metabolite internal reference (NAA and water peak (i.e. $\Delta_{water\text{-}NAA}$) is different for grey and white matter, thus this difference may influence MRSI temperature mapping. A plot of MRSI temperature estimates versus white matter content for each voxel is shown in Figure 5.13. It was observed that at this slice location (corpus callosum) relatively few GM voxels are available; as a result it was not possible to verify tissue specific metabolite frequency differences which may affect temperature mapping. Vescovo (51) suggest to account for tissue specific differences by employing correction factors based on percentage basis of the tissue type composition for each voxel obtained from the segmentation data.

However, this approach requires the precise metabolite frequency at various proportions white and grey matter to be known. These are not readily available. Thus the use of correction factors for different tissue types was not explored in this study. Instead, a second analysis was performed, by retaining primarily white matter voxels in the analysis (analysis 2). The results of the second analysis indicate a regional core to superficial brain temperature gradient. However with this higher level of filtering only 13% of the acquired

data was retained for the analysis. As a result of this filtering the statistical power was significantly reduced; however, these results provide a promising start for larger studies, necessary to validate these findings.

For future studies is it prudent to reduce MRSI voxel size to reduce the contributions from different tissue types. However, reducing the voxel size also reduces SNR. In this study MRSI data were acquired to produce 0.85 cm^3 voxels in order to obtain MRSI spectra with similar SNR, as obtained for in vitro (phantom) studies (in chapters 3 and 4) which employed metabolite solutions containing NAA at physiological concentrations. However the voxel size can be further reduced and SNR can be maintained at the same time by employing 3T scanner and/or multi-channel receiver coils, provided that excellent can be shimming be obtained. However the increased magnetic field inhomogeneity (at 3T) may outweigh this theoretical gain in SNR. Thus the use of higher field strength (3T) scanners for MRSI temperature mapping is currently under investigation and forms part of a larger validation study (in collaboration with Dr Michael Thrippleton, PI Prof Ian Marshall).

The use of fast echo planar spectroscopic imaging techniques also offers to increase the spatial resolution and speeds up MRSI acquisition (89;90) and these methods have comparable SNR to standard MRSI technique (89). This makes them a promising candidate for temperature mapping. A study to assess feasibility of employing fast echo planar spectroscopic imaging for temperature mapping is presented in Chapter 6. The following section in this chapter will focus on the repeatability of the MRSI temperature estimates presented in this section.

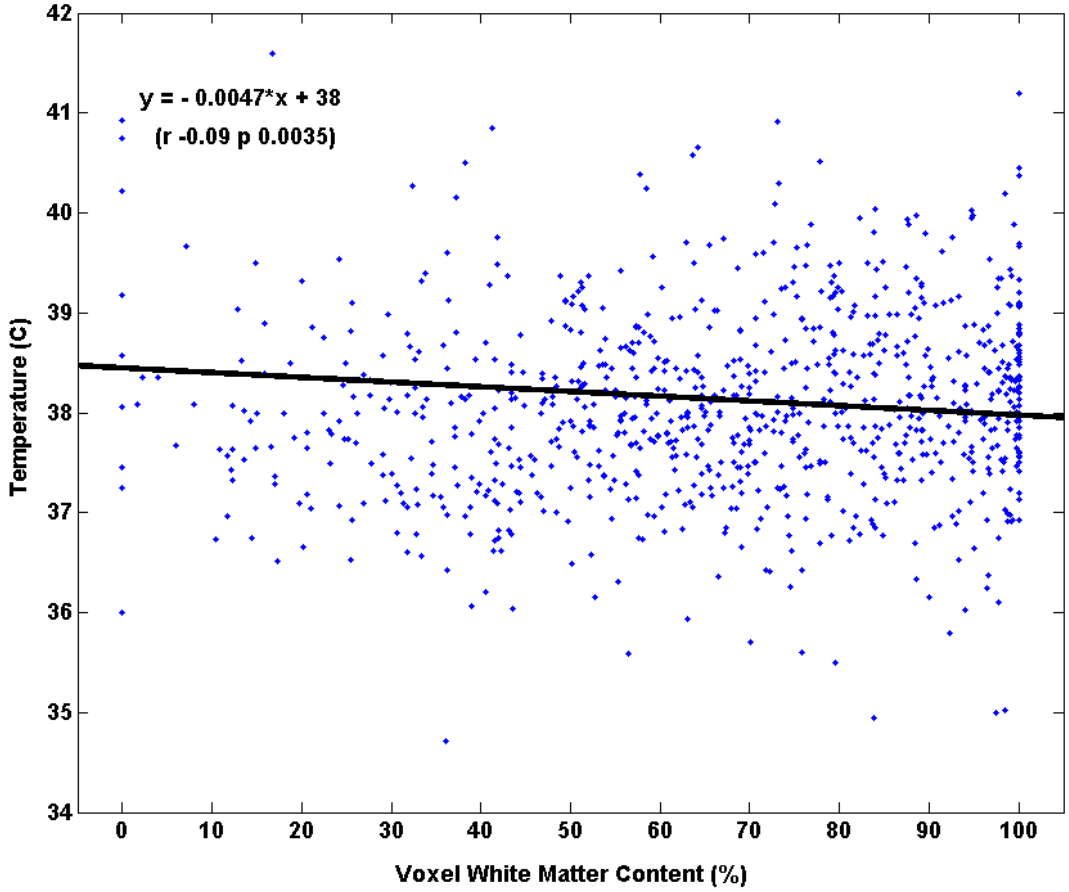

Figure 5.13 Plot showing MRSI temperature estimates versus white matter content for all the voxels for the 12 healthy male subjects, included are the voxels containing CSF<10% and NAA linewidth <10Hz.

5.5 In-vivo repeatability

5.5.1 Introduction

The results reported in chapter 4 indicate excellent in-vitro repeatability of MRSI temperature estimates. In addition to NAA amplitude variation and differences in the scan set up (field strength, shimming, pulse sequence), a number of factors such as subject motion and physiological variations may influence temperature estimates. Thus it is important to assess in-vivo repeatability (within session and between sessions) of MRSI temperature mapping. A larger study investigating between session repeatability of MRSI temperature estimated obtained using 2 different scanners (1.5T and 3T) is currently being pursed in collaboration with Dr Michael Thrippleton (PI Professor Ian Marshall). A comprehensive statistical analysis using general linear modelling will be employed in this study to determine the relationship of MRSI temperature estimates on a number of the factors such (regional difference, scanner effects, NAA amplitude, tissue specific differences) as discussed in previous sections. The aim of the following paragraphs is to provide a preliminary built up to this larger study by performing a simpler (with in session) repeatability analysis.

5.5.2 Methods

Four back to back MRSI scans were acquired and processed from 12 healthy young male volunteers as discussed in section 5.4. In order to determine the repeatability of the MRSI temperature estimates obtained from for these scans were used. The temperature estimates from the first scan were considered as the reference and a list of valid voxels (i.e. NAA linewidth <10Hz and CSF content <20%) to be retained for the analysis was determined. The variation of MRSI temperature estimates for these valid voxels in subsequent scans was assessed by performing regression and Bland Altman analyses between the three scan pairs (Scan 2- Scan 1, Scan 3 - Scan 1 and Scan 4 - Scan 1).

5.5.3 Results and discussion

The mean and SD of the MRSI temperature estimates and NAA amplitude for the valid voxels (obtained from the first scan) for 12 volunteers for the 4 scans is shown in Tables 5.14 and 5.15. The plots for regression and Bland-Altman analyses for the MRSI Temperature estimates for the three scans pairs (scan 2- scan 1, scan 3 - scan 1 and scan 4 - scan 1) are shown in Figures 5.14 and 5.15 respectively. The subject wise distribution of the temperature difference between scans is shown Figure 5.16. It is seen on an average the brain temperature for these volunteers reduces by ~0.4 ^{0}C. This temperature reduction is greater than that 0.09^{0}C that previously reported by Marshall et al. (44) for four healthy male volunteers. Marshall et al. (44) repositioned the subjects between the scans, while in this study all the MRSI scans were acquired back to back with out any repositioning. This difference in set up may be one of the factors for the different results between these two studies.

In this study volunteers were requested to be idle during the scan session thus it may be speculated that this temperature reduction may be due to reduced metabolic activity. However as these volunteers have already been scanned for additional 5 sessions, (2 sessions using the same set up discussed here and other 3 sessions using a 3T scanner) to assess day to day repeatability as part of the larger study. It is prudent to further investigate the consistency of this finding to rule out a number instrumental and scan related factors before attempting to relate the temperature reductions during the scans to physiological variables.

Volunteer	Temperature (^{0}C)							
	Scan 1		Scan 2		Scan 3		Scan 4	
	Mean	SD	Mean	SD	Mean	SD	Mean	SD
1	38.02	1.04	37.53	1.07	37.58	1.04	37.60	0.88
2	38.03	0.81	37.87	0.82	37.84	0.77	37.77	0.93
3	38.19	0.78	37.60	0.90	37.32	1.10	37.76	0.80
4	37.93	0.73	37.76	0.93	37.71	0.83	37.80	1.00
5	37.79	0.90	37.77	1.16	37.67	1.01	37.74	0.87
6	37.92	0.98	37.59	1.11	37.57	0.98	37.88	1.08
7	38.26	0.77	38.45	0.85	37.81	0.89	37.90	0.77
8	38.38	0.91	38.13	0.95	37.96	0.85	37.99	0.92
9	37.62	0.71	37.28	1.04	37.20	0.58	37.09	1.14
10	37.85	1.09	37.36	1.02	37.08	0.90	37.10	0.81
11	38.41	1.06	37.82	1.18	37.54	1.21	37.55	1.26
12	37.87	0.78	37.70	1.03	37.49	0.88	37.51	0.92
Mean	38.02	0.88	37.74	1.00	37.56	0.92	37.64	0.95
SD	0.24	0.14	0.32	0.12	0.26	0.16	0.29	0.15

Table 5.14 Mean and SD of MRSI temperature estimates for different scans for 12 young male volunteers.

	NAA Amplitude (I.U.)							
	Scan 1		Scan 2		Scan 3		Scan 4	
Volunteer	Mean	SD	Mean	SD	Mean	SD	Mean	SD
1	119.5	22.8	118.1	21.8	117.3	22.7	116.2	20.6
2	122.8	18.8	118.5	17.1	122.3	17.3	119.1	15.2
3	111.4	20.5	110.4	18.6	108.8	22.1	112.2	18.5
4	117.3	17.9	116.0	18.9	111.8	17.3	113.2	17.2
5	209.4	39.7	203.2	41.7	205.3	39.9	202.7	40.9
6	120.9	19.9	120.0	20.8	113.9	19.8	118.7	21.2
7	122.4	20.7	123.9	15.0	121.8	15.8	124.8	21.9
8	123.0	24.8	117.9	24.3	118.4	23.4	115.4	22.1
9	123.4	17.5	122.0	15.7	120.1	24.1	132.0	22.1
10	116.6	21.1	120.8	20.2	119.4	19.2	115.8	20.1
11	135.6	19.4	135.1	18.0	133.2	20.8	134.8	18.8
12	115.5	17.1	116.8	18.8	116.9	17.4	115.8	16.0
Mean	128.15	21.69	126.89	20.90	125.77	21.65	126.73	21.22
SD	26.28	6.09	24.72	7.02	25.78	6.36	24.99	6.64

Table 5.15 Mean and SD of NAA amplitudes for different scans for 12 young male volunteers.

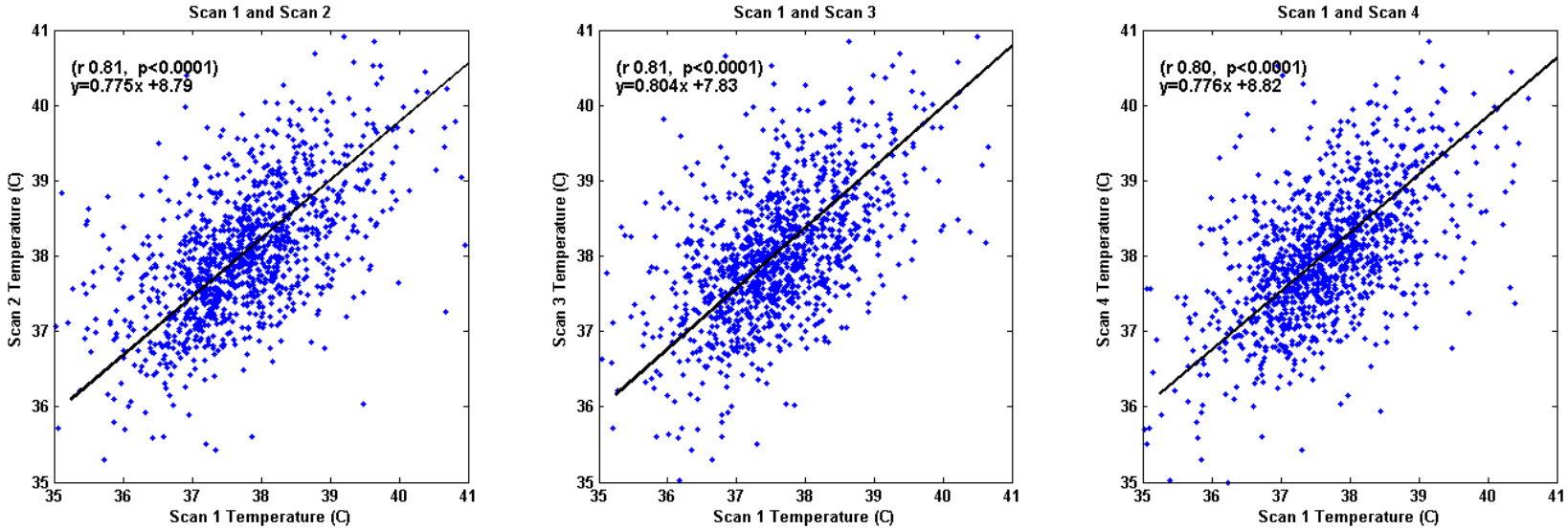

Figure 5.14 Linear regression analysis of temperature estimates for scan pairs (Scan 2 and Scan 1, Scan 3 and Scan 1, Scan 4 and Scan 1) using all valid voxels for the 12 volunteers. Excellent agreement between the temperature estimates is observed.

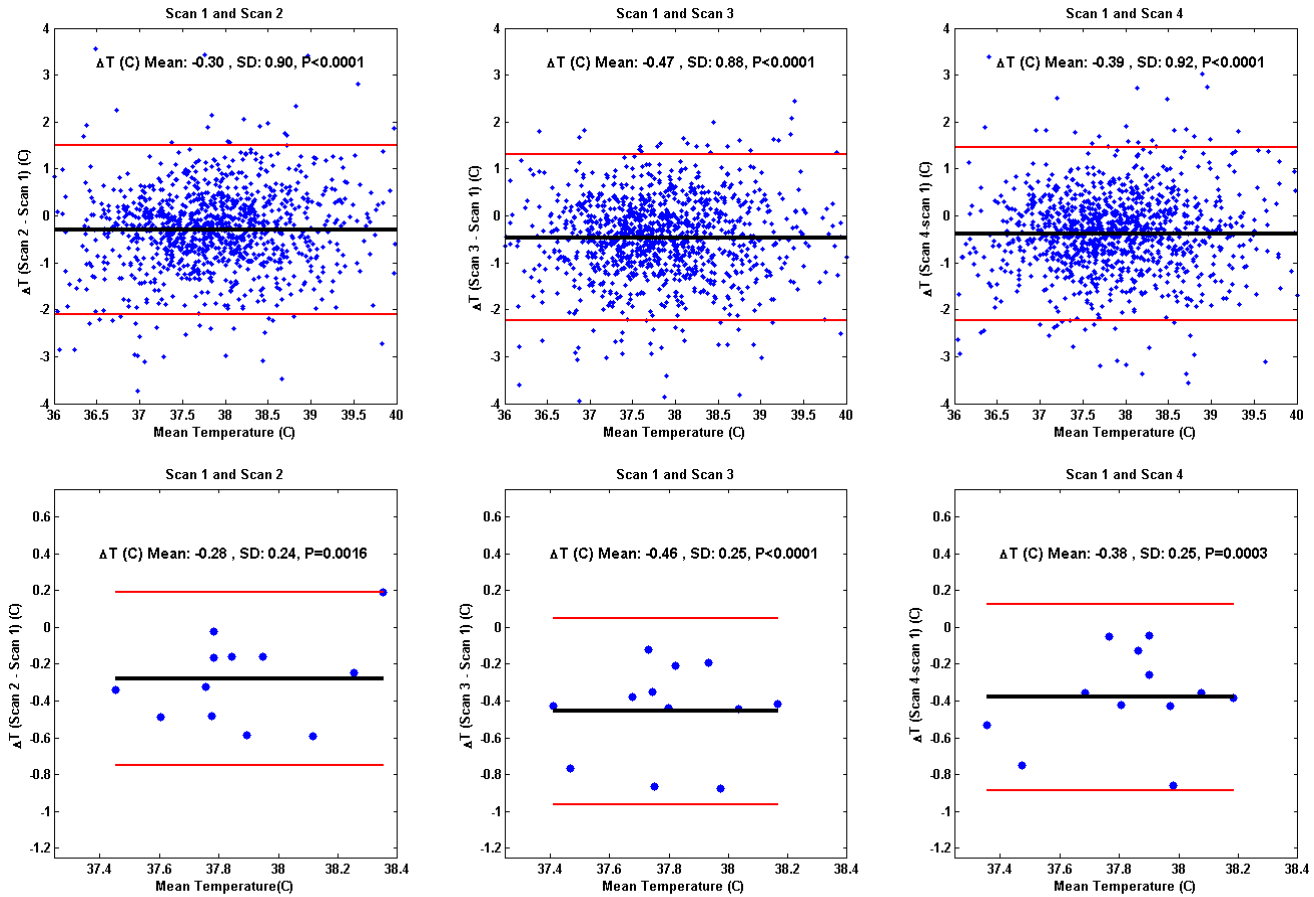

Figure 5.15 Bland-Altman analysis between the 3 scan pairs (Scan 2 and Scan 1, Scan 3 and Scan 1, Scan 4 and Scan 1) using temperature estimates from all valid voxels for the 12 subjects (top row) and using the average temperature estimates reported in Table 5.14 (bottom row). These results indicate that brain temperature reduces with scans.

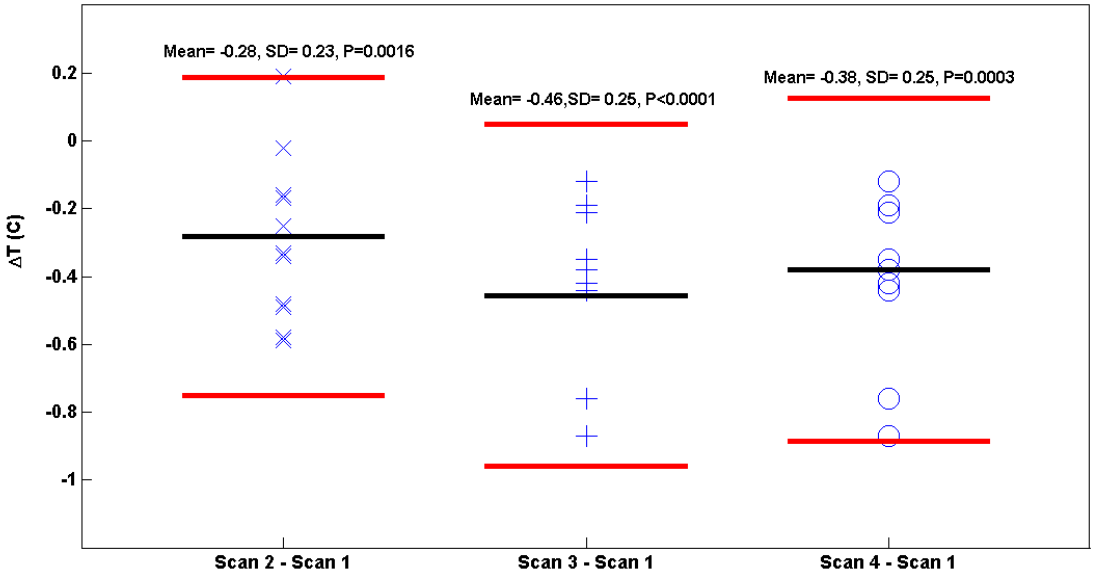

Figure 5.16 Plot showing the spread of temperature difference between the first and the other scans (2/3/4) for 12 young male volunteers, temperature difference were obtained using mean MRS temperature estimates reported in Table 5.14. Also shown is the mean (in black) and mean ± 2*SD (in red).

5.6 Summary

After a thorough in-vitro validation, the MRSI data acquired from healthy elderly and younger volunteers were employed to assess temperature variations between core (central) and cortical (peripheral) brain structures. The analysis of MRSI temperature maps from healthy elderly volunteers suggests the core regions of the brain to be warmer compared to peripheral regions by 0.3^0C. However this analysis did not reach statistical significance as the spread of data was large and thus it was not possible to relate this temperature gradient with the structure ratings or cognitive scores. The main reasons were rejection of a large proportion of the data due to larger linewidths (>10Hz) of the internal reference metabolite peak (NAA). The quality of MRSI data improved after optimising MRSI slice positioning (to improve shimming). A regional analysis of MRSI data acquired from 12 young healthy volunteers suggests a temperature gradient of 0.3^0C between core and outer regions of the brain. However further validation is required to verify whether the frequency difference between water and metabolites peaks are different between grey and white matter and whether they influence regional MRSI temperature estimates. Furthermore the analysis of the repeatability (within session) of the in-vivo MRSI temperature estimates indicate a reduction of the temperature during the scans and provide a promising start for future analysis. It is important to mention that a single MRSI scan can be employed to measure small temperature differences (of upto 0.2^0C) on a scan-by-scan basis as shown in section 4.3, provided short metabolite linewidths (typically 1-2 Hz) are obtained. The NAA linewidths obtained in vivo typically vary between 5-10 Hz due to the limitations/effectiveness of the shimming procedure. Thus the random uncertainty in frequency estimation due to larger linewidths limits the application of MRSI temperature mapping to identify regional temperature variations, which are greater than 0.5^0C on per patient/subject basis. And a study with a larger sample size is necessary to identify regional brain temperature differences of lower magnitude (i.e. less than 0.5^0C).

6 Echo Planar Spectroscopic Imaging

6.1 Introduction

Extensive validation of MRSI based temperature mapping has been discussed in previous chapters. The typical MRSI acquisition times using conventional PRESS with useful matrix sizes (such as 24*24 or 32*32) are long (10-15 minutes) and thus limits MRSI (and temperature) measurements to single slices. The use of echo planar spectroscopic imaging (ESPI) technique reduces the acquisition time and permits volumetric MRSI acquisition within clinically feasible exam times. In addition using the EPSI sequence as described by Ebel et al.(89;91) both water suppressed metabolite and non water suppressed reference scans can be acquired simultaneously (reference scans are acquired in an interleaved manner). Thus it may be possible to completely avoid the systematic error due to water suppression as discussed in chapter 3. However, these sequences have not been employed to measure brain temperature.

In this chapter the feasibility of EPSI for temperature mapping will be assessed. In section 6.2, a brief overview of EPSI and automated MRSI data processing for temperature mapping will be presented. Temperature maps obtained from the EPSI data acquired using a room temperature phantom and healthy volunteers will be presented in sections 6.3 and 6.4 respectively

6.2 Echo Planar Spectroscopic Imaging and automated data processing

The acquisition time for traditional spin echo based imaging sequences depends on the repetition time (TR) and the number excitations. In-contrast, echo planar imaging (EPI) as first proposed by Nobel laureate Sir Peter Mansfield and co-workers, acquires multiple lines of k-space per excitation by using oscillating read out gradients (92). As a result, fewer excitations are necessary to collect the entire k-space, which decreases the scan time (to milliseconds). This method is widely used in MR imaging and a review by Mehdi. et al. (93) provides an interested reader with a basic overview of principles and applications of EPI. Reducing the acquisition time by using fast EPI based spectroscopic imaging techniques was proposed by Mansfield (94) however the first implementation echo planar spectroscopic imaging (EPSI) on a clinical scanner was performed by Posse et al. (95). The feasibility of 3D volumetric EPSI and automatic MRSI data processing for whole brain metabolite mapping was then reported by Ebel et al. (91)

In this work the MRSI data acquired using a volumetric EPSI based sequence as discussed by Ebel et al. (89;91) will be employed to assess the feasibility of EPSI based brain temperature mapping. This EPSI pulse sequence is shown in Figure 6.1 and was used to acquire the EPSI data. Briefly this pulse sequence consists of optimized slice selective RF pulses to excite a thick slab covering the entire brain volume with lipid and water suppression (CHESS based) pulses being applied prior to EPSI acquisition. Slice selection and phase encoding (using gradients G_z and G_y) were conventional and the data was sampled under an oscillating readout gradient (G_x) to encode both the third spatial and the spectral (i.e. chemical shift) information. Additional non-water suppressed reference scans were also acquired using a low flip angle excitation in an interleaved manner. The spatial-spectral information, which was encoded simultaneously, was then obtained by applying 2 stage Fourier transforms (FT) during reconstruction process. Firstly, a spatial FT was employed to obtain the spatial location of each spectrum and then a second FT was employed to obtain spectra (containing chemical shift information) at every spatial coordinate. In order to reduce artifacts due to chemical shift

misregistration, spatial-spectral oversampling was applied during the readout phase (by increasing the bandwidth of the readout gradient) and editing of odd/even echoes (i.e. echoes acquired with positive/negative readout gradients) was performed prior to the application of spatial-spectral FT. For a comprehensive overview of spatial-spectral encoding using echo planar readout the reader is referred to the original paper by Posse et al. (95).

For this study EPSI data were acquired using a 3T Siemens scanner and were provided by Professor Andrew Maudsley and Dr Govindaraju Varanavasi, Department of Radiology, University of Miami under a research agreement. EPSI acquisition parameters were TR/TE = 1710 ms/70 ms, FOV: 280 × 280 × 180 mm^3, 50 × 50 × 18 spatial samples over a 135mm slab, and acquisition time of 26 minutes with a spectral width of 2500Hz (number of points/samples=1000) . CHESS based water suppression, and inversion-recovery pulses (TI = 198 ms) for nulling of the lipid signal were employed before acquiring EPSI data as shown in Figure 6.1. The EPSI datasets were interpolated to 64 × 64 × 32 voxels during reconstruction. Additional structural scans (for in-vivo acquisitions) included, T_2-weighted gradient-echo imaging (TE/TR: 87 /6400 ms, 33 slices, slice thickness 4mm, FOV: 220 × 220 mm^2, and acquisition time ~5 minutes), and T_1-weighted imaging (MPRAGE; TE/TR/TI: 2.38 /2300/900 ms, 160 slices, 1mm slice thickness, FOV: 256 × 256 mm^2, and acquisition time ~5 minutes). For in-vivo acquisitions, in addition to automatic second order shimming, the EPSI and structural scans were acquired at an angle of 15^0 to anterior commissure -posterior commissure (AC-PC) line to improve the B_o homogeneity over the volume by avoiding the air-tissue interfaces encountered at the frontal sinuses. The EPSI acquisition mentioned in this section was designed to obtain spectroscopy data from entire brain volume (i.e. 18 slices with slice thickness: 10mm) and thus has a long acquisition time of 26 minutes. However a single slice EPSI scan (including non water suppressed referenced scans) can be acquired in less than 2 minutes. Thus this acquisition scheme is ~10 times quicker compared to standard PRESS MRSI, as 20 minutes will be required to collect the same data using standard PRESS MRSI (10 minutes for water suppressed scan and 10 minutes for non water suppressed reference).

A typical volumetric EPSI scan acquires a large number of spectra (typically ~7000-8000 per scan) thus an automated tool (MIDAS) was developed by the group to process the MRSI data (96). A flow chart of the various data processing steps in MIDAS is shown in Figure 6.2 and a comprehensive overview can be obtained from the original paper by Maudsley et al. (96). The author (of this thesis) processed the EPSI data using MIDAS to estimate temperature maps; all the changes performed to obtain temperature maps were performed by the author as described in the following paragraphs.

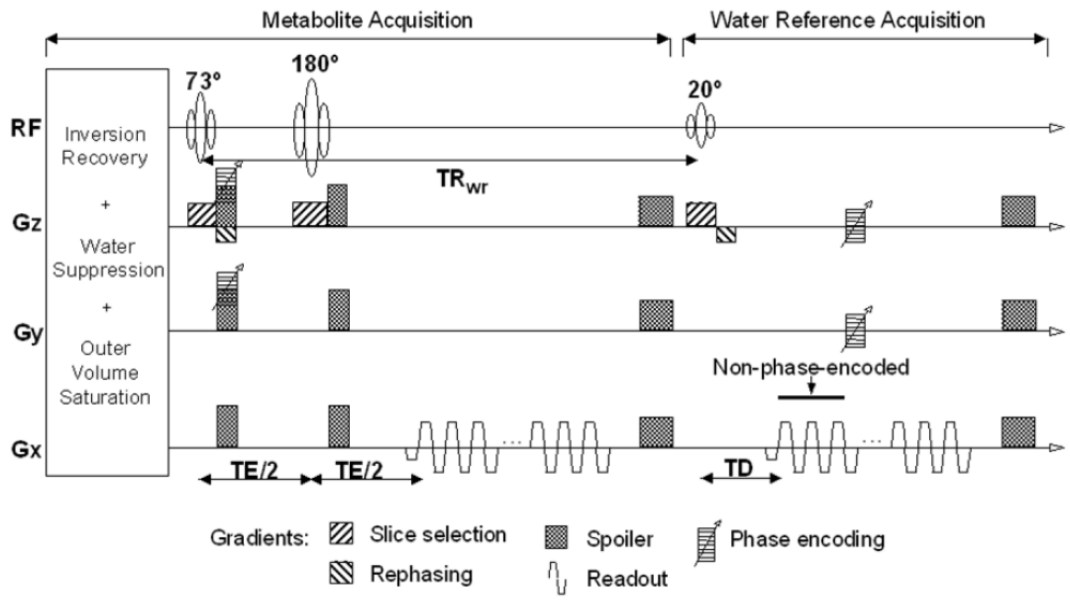

Figure 6.1 EPSI pulse sequence with interleaved water reference scan as described by Ebel et al. (91).

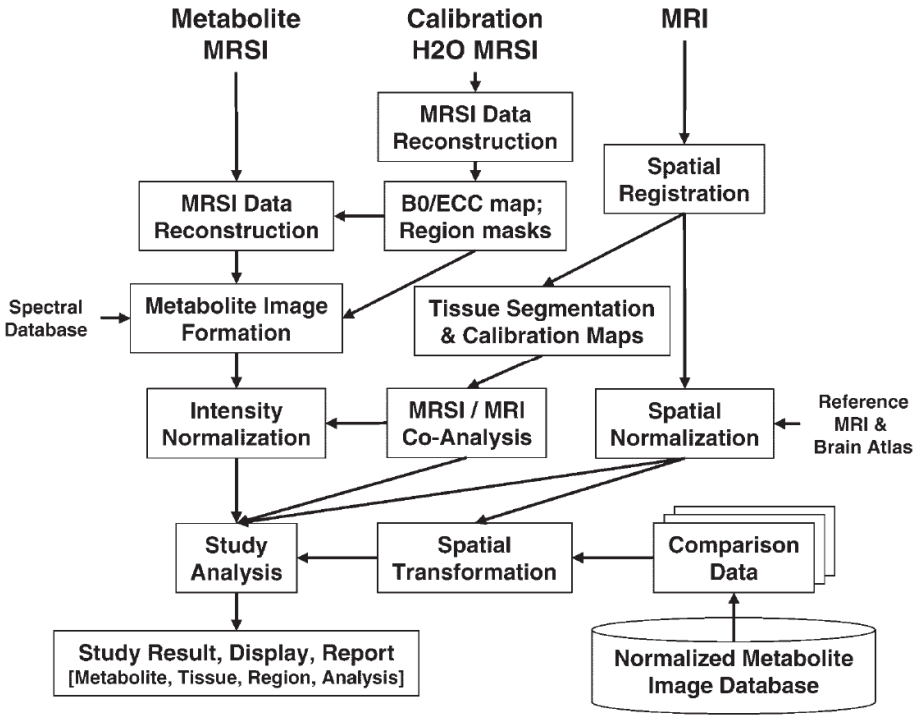

Figure 6.2 Overview of MRSI data processing using MIDAS (from Maudsley et al. (96)).

6.2.1 Temperature estimation using MIDAS

MIDAS is an automated spectroscopy data processing and analysis tool based on IDL (version 8). A comprehensive overview of MRSI data processing using various MIDAS modules can be obtained from the MIDAS user manual and the basic processing steps are highlighted in Figures 6.2 and 6.3. The following paragraphs briefly summarise the steps required to generate temperature maps using EPSI data and MIDAS.

Spectral fitting (using the FITT module) was employed to estimate the frequency, amplitude and linewidth of the metabolite internal reference (NAA) from water suppressed metabolites data (SI) and of the water peak from the interleaved non water suppressed reference scan (SI-REF or Water-SI). Different prior knowledge files (for metabolite and water fitting) were generated. Eddy current correction (ECC) and corrections for B_o shift were applied before the spectral fitting (for both SI and SI-REF data) in order to phase the spectra and to account for shifts due to the B_o field inhomogeneity. The ECC and B_o maps were generated using the SI-REF (non water suppressed) data and the REFDAT algorithm before spectral fitting. For in-vivo datasets tissue segmentation maps (from T_1w obtained using FAST)

were used to determine the percentage tissue type composition of each spectroscopy voxels (results outputted as maps of fractional tissue content for the each spectroscopy voxel). The processed data (i.e. maps of metabolites and water amplitude frequency, linewidth, voxel tissue composition etc) were exported out of the MIDAS platform in comma separated value (CSV) format. The processed data were then imported into MATLAB to determine temperature maps by computing the frequency difference between the water and metabolite internal reference (NAA) peaks on a voxel by voxel basis using equation 2.7. As a quality assurance measure voxels with NAA linewidth greater than 12 Hz or CSF content greater than 10% (for in-vivo data) were excluded from the analysis.

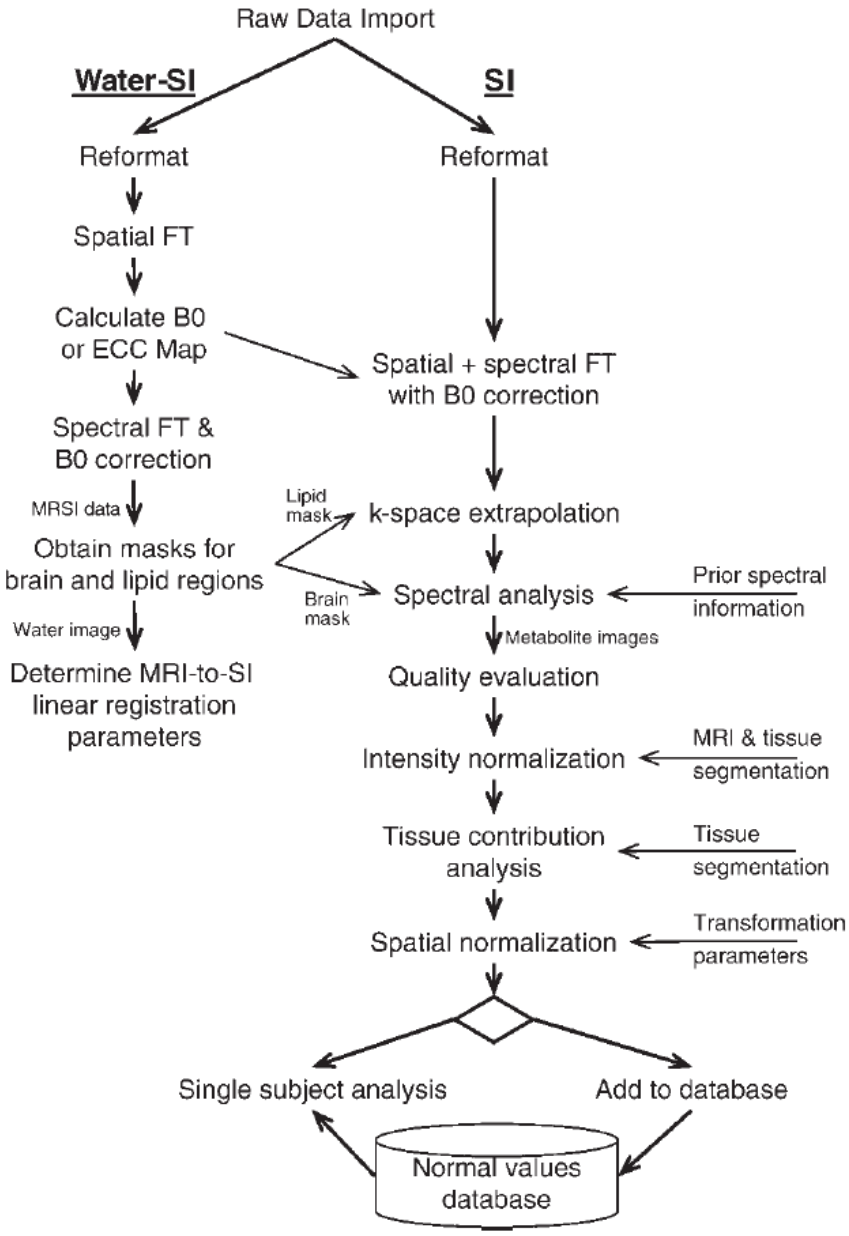

Figure 6.3 Spectroscopy processing pipeline (in MIDAS) as described by Maudsley et al. (96)

6.3 In-vitro study

6.3.1 Introduction and methods

In order to assess the feasibility of the temperature mapping, ESPI dataset acquired using room temperature (~22^{0}C) phantom was employed to estimate temperature maps. The phantom contained brain metabolites (NAA, Creatine and Choline) at physiological concentrations. EPSI data acquisition parameters and data processing to obtain temperature maps using MIDAS were the same as previously discussed.

6.3.2 Results and Discussion

The volumetric temperature maps obtained from the EPSI data acquired using homogenous room temperature phantom are shown in Figure 6.4 while reference images of the phantom are shown in Figure 6.5. A box plot of the temperature estimates from central slices (slice numbers 12-23) is shown in Figure 6.6. It was seen that the temperature maps obtained in the central slices of the phantom (slice numbers 12-23) were uniform within ±0.5 ^{0}C. The average temperature of the phantom estimated from these central slices was 22.8 ^{0}C (SD 0.3 ^{0}C). However for these central slices, a large variation in temperature estimates was observed at the edge of the phantoms. A large variation in temperature estimates for slices located at the edge of the phantom (slice numbers 6-11 and 23-29) was also observed. The NAA linewidth maps (for selected slices) are shown in Figure 6.7. For the central slice (slice number 17) it is observed that the NAA linewidth increases at the edge. The NAA linewidths are larger for the slices located at the edges of the phantom as shown in Figure 6.7.

For the central slices (slice numbers 12-23) on an average 15% (SD 2%) of the acquired data were rejected based on the quality assurance criteria (NAA LW >12 Hz), while on an average 40 % (SD 7%) of the voxels were rejected from slice numbers 6-11 and 24-29. The average NAA linewidth of all the valid voxels (i.e. voxels with NAA LW <12 Hz) for all central slices (slice numbers 6-29) was 5.1 Hz (SD 0.66 Hz) and is larger compared to 1-2Hz typically obtained in previous chapters for the phantom studies. This is due to

the fact that the rectangular excitation volume for EPSI acquisitions is ~20 times that employed in previous chapters to ensure maximum coverage of the phantom. The difficulty to shim over a larger volume at 3T is the primary reason for the larger linewidths. The increased susceptibility difference between phantom material and air at edges of the phantom is also a plausible explanation for the broader linewidths and thus the increased variability in temperature estimates at the edges of the phantom.

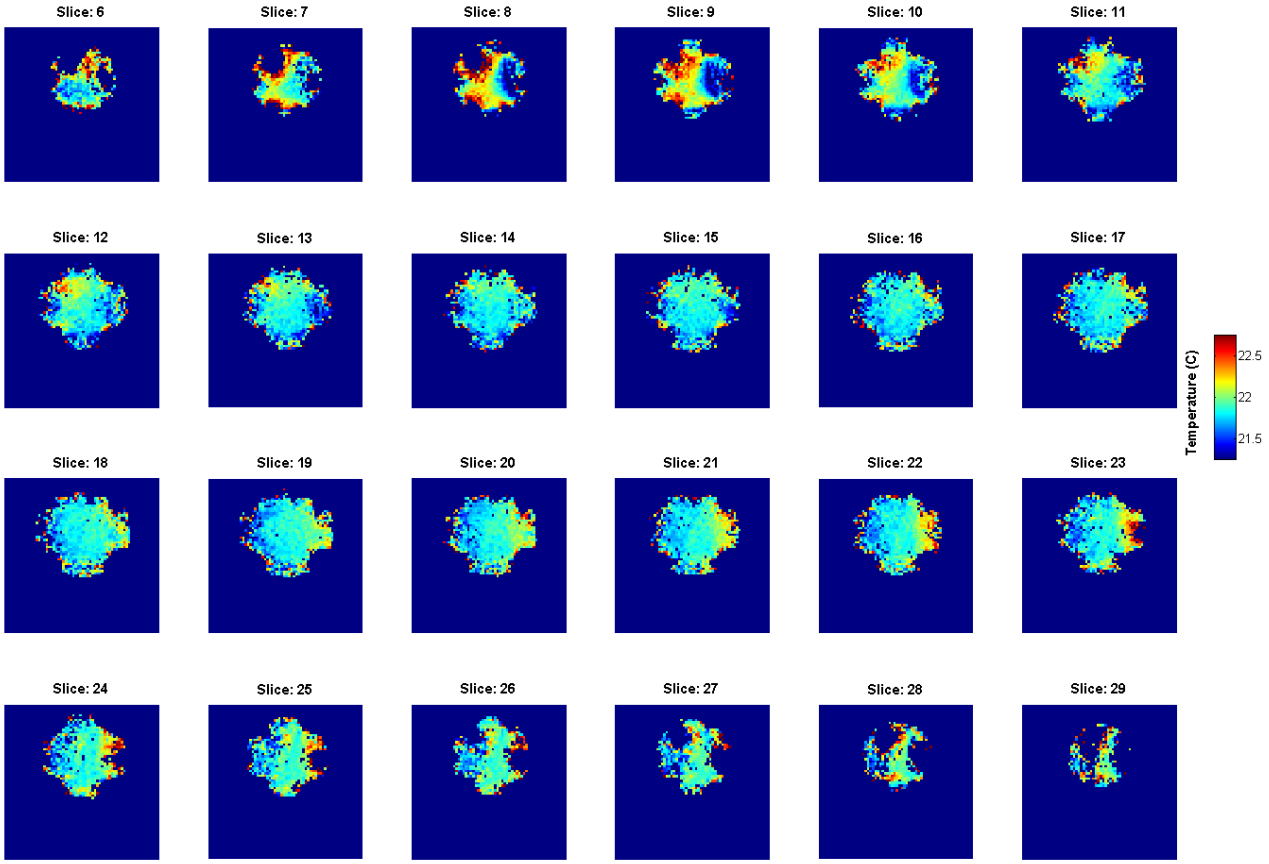

Figure 6.4 Temperature maps computed using high resolution EPSI data acquired using a room temperature phantom, also see Figure 6.5 (rejected voxels shown at lowest temperature)

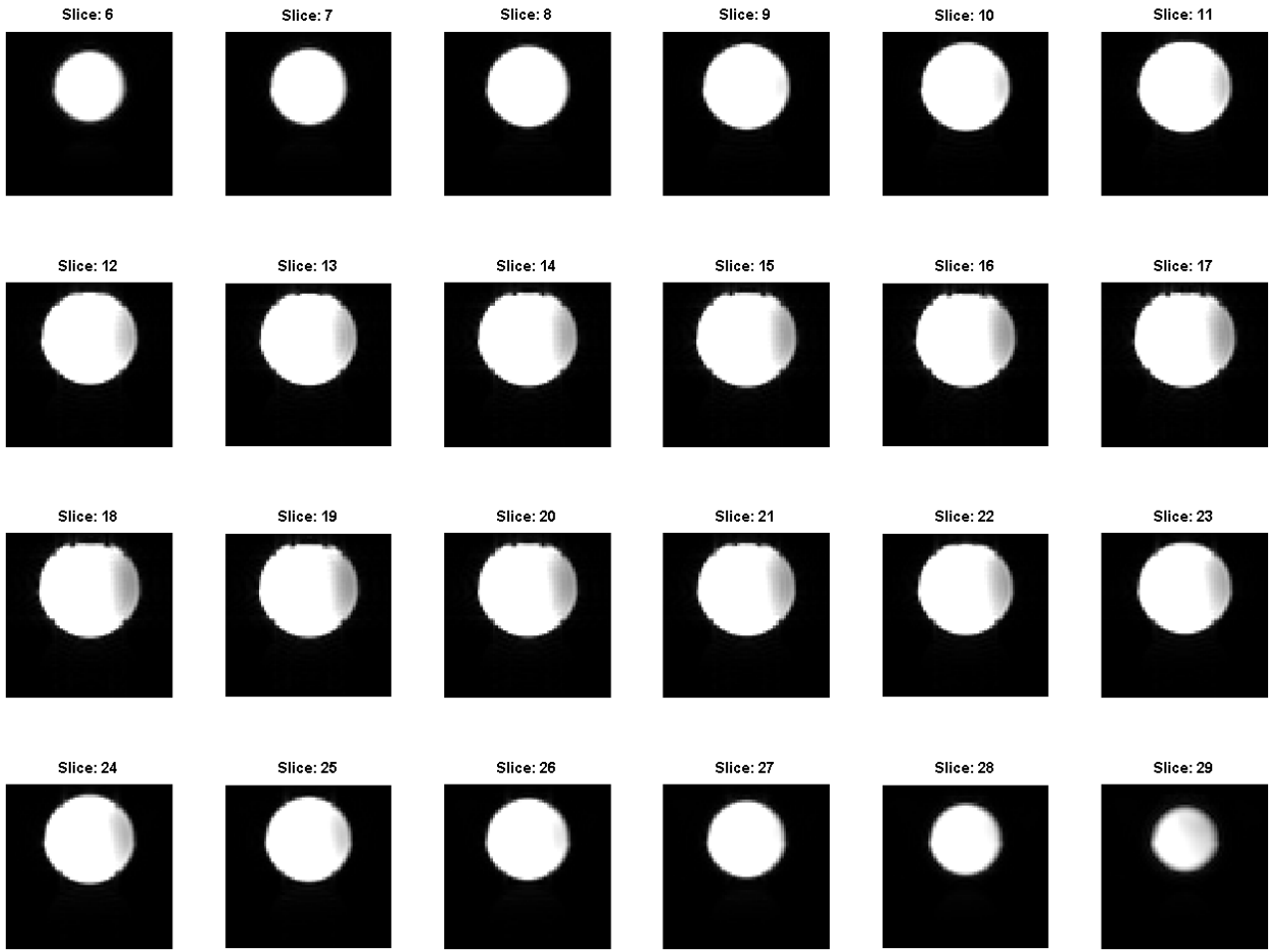

Figure 6.5 Reference images of the phantom for the temperature maps shown in Figure 6.4

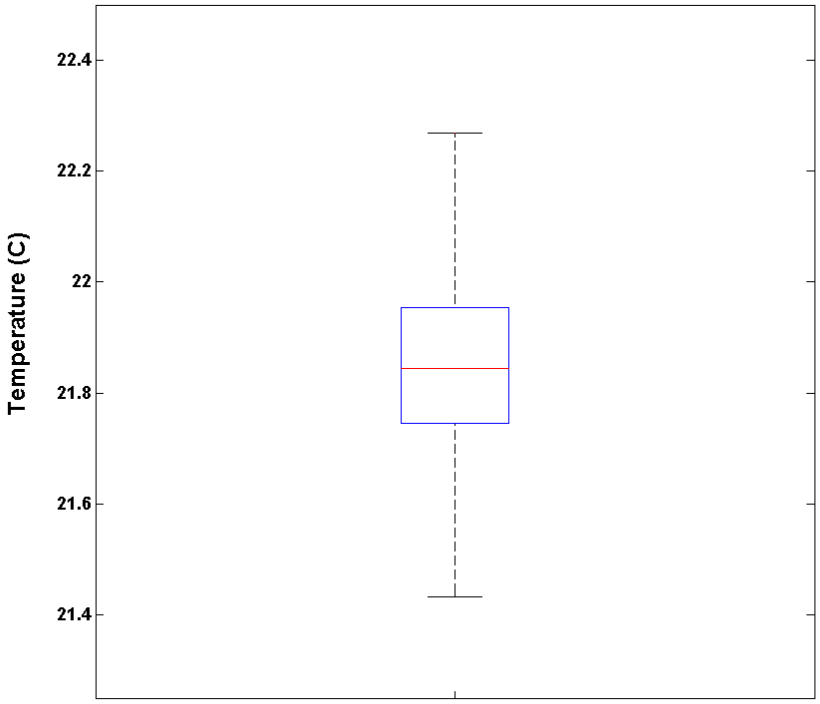

Figure 6.6 Box plot showing the spread of the MRS temperature estimates across the central slices (slice numbers 12-23) for temperature reported in Figure 6.4.

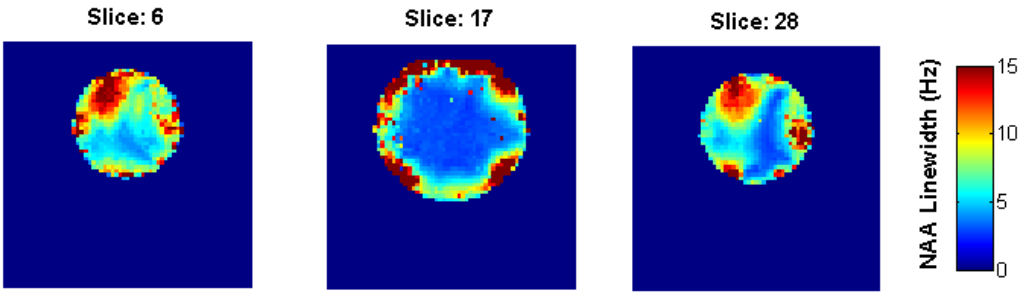

Figure 6.7 NAA linewidth maps for the EPSI data acquired from a phantom used to generate temperature maps shown in Figure 6.4.

6.4 In-vivo study

6.4.1 Introduction

The temperature maps obtained using EPSI data and MIDAS from a room temperature phantom were uniform and no systematic errors could be identified in the temperature maps obtained from the central regions of the phantom, as seen in the previous section. These results suggest EPSI imaging could be employed for brain temperature mapping. In this section, EPSI data collected from 5 healthy volunteers were employed to determine the in-vivo feasibility of brain temperature mapping using ESPI. Recently the frequency difference ($\Delta_{water\text{-}naa}$) used to estimate temperature was reported to be different for the two main brain tissues types (GM and WM) (66), thus if unaccounted for the tissue specific frequency differences may introduce errors (of up to 1 ^{0}C) in in-vivo brain temperature estimates. Thus the second aim of this study was to employ EPSI to verify these findings and to assess whether correction factors can be obtained to account for these tissue specific frequency differences.

6.4.2 Methods

In order to determine feasibility of brain temperature mapping using EPSI, EPSI and MR imaging data acquired from 5 healthy volunteers at the University of Miami were processed using MIDAS to obtain whole brain temperature maps as discussed in the previous section 6.2. In order to retain a larger proportion of the voxels in the study the analysis was limited to five central slices for each volunteer thereby avoiding slices at edges of the field of view. For each subject in the analysis the slices start at the level of basal ganalia and end at the level of centrum semiovale as shown in Figures 6.8 and 6.9, In order to assess tissue specific metabolite frequency differences, segmentation maps showing the relative tissue fraction (of grey matter, white matter and CSF) for each spectroscopy voxel was obtained for the central slice for these 5 volunteers. The temperature estimates were normalized by subtracting the median brain temperature on a subject by subject basis and a regression analysis was performed between normalized temperature estimates and voxel white matter content for the five central brain slices for

these five volunteers. For quality assurance spectroscopy voxels containing more than 10% CSF or with NAA line widths greater than 12 Hz were rejected from the analysis.

6.4.3 Results

Example of temperature maps at five central slice locations estimated using EPSI data acquired from a healthy volunteer are shown in Figure 6.8. The temperature estimates averaged from same five central brain slices (i.e. from basal ganglia to centrum semiovale) for these 5 healthy volunteers is shown in Table 6.1. On average, for each subject 47% (SD 4%) of the acquired voxels were rejected based on the quality assurance criteria (NAA >12 Hz and voxel CSF content >10%). Examples of the unedited temperature maps are also shown in the Figure 6.8. The corresponding tissue segmentation maps for grey and white matter are shown in Figure 6.9. The spread of the temperature estimates plotted as a function of the white matter content of the MRS voxels for each volunteer are shown in Figure 6.10. Boxplots of the temperature estimates from these 5 volunteers at different level of white matter fraction are shown in Figure 6.11 and average values are reported in Table 6.2.

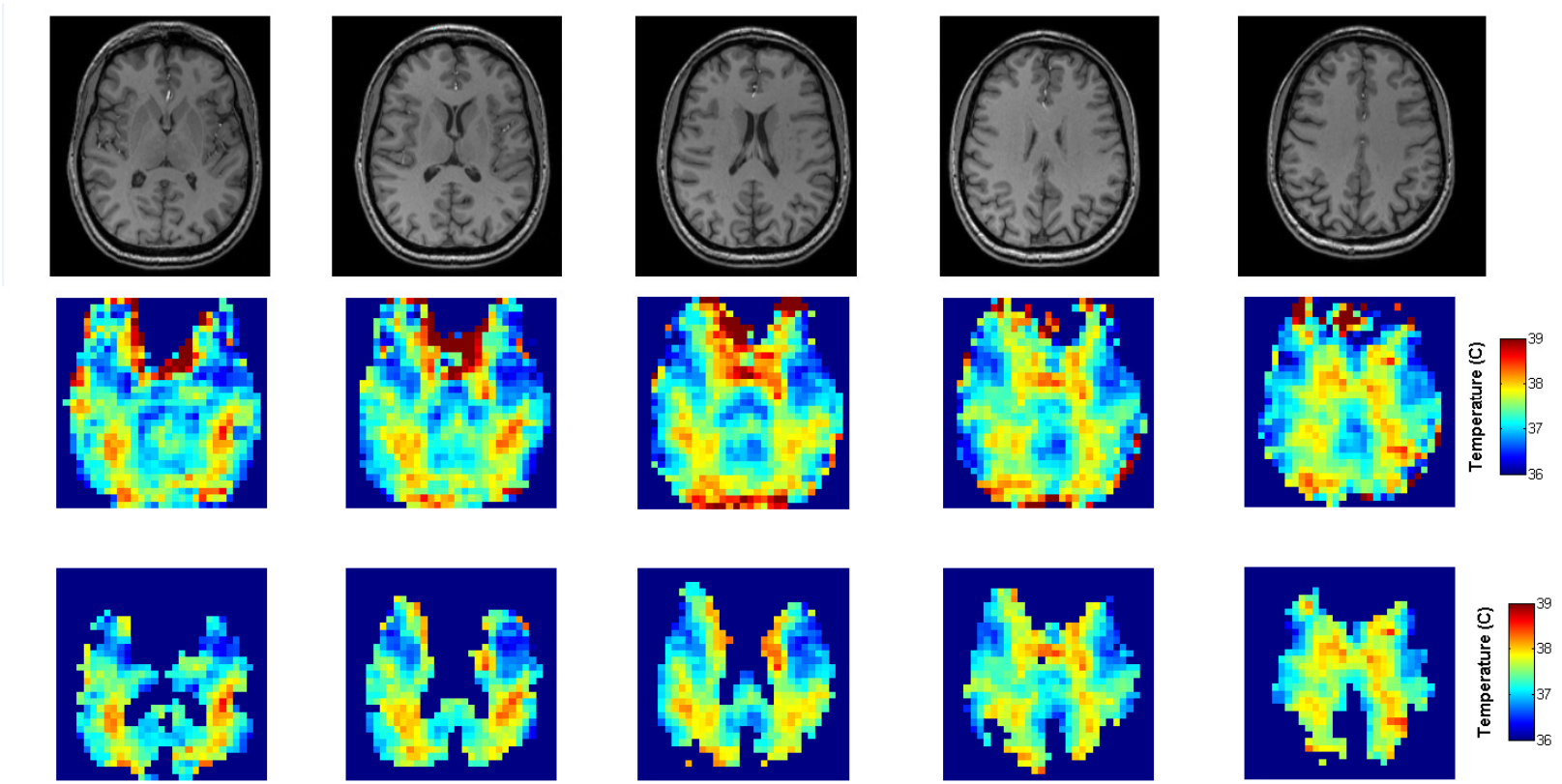

Figure 6.8 Examples of temperature maps from 5 central brain slices (MRI images shown in top row) obtained using EPSI data acquired from a healthy volunteer. The middle row shows unedited temperature maps while the bottom row shows the temperature maps obtained after rejecting voxels with more than 10% CSF or NAA linewidths >12 Hz (rejected voxels show at a lower temperature).

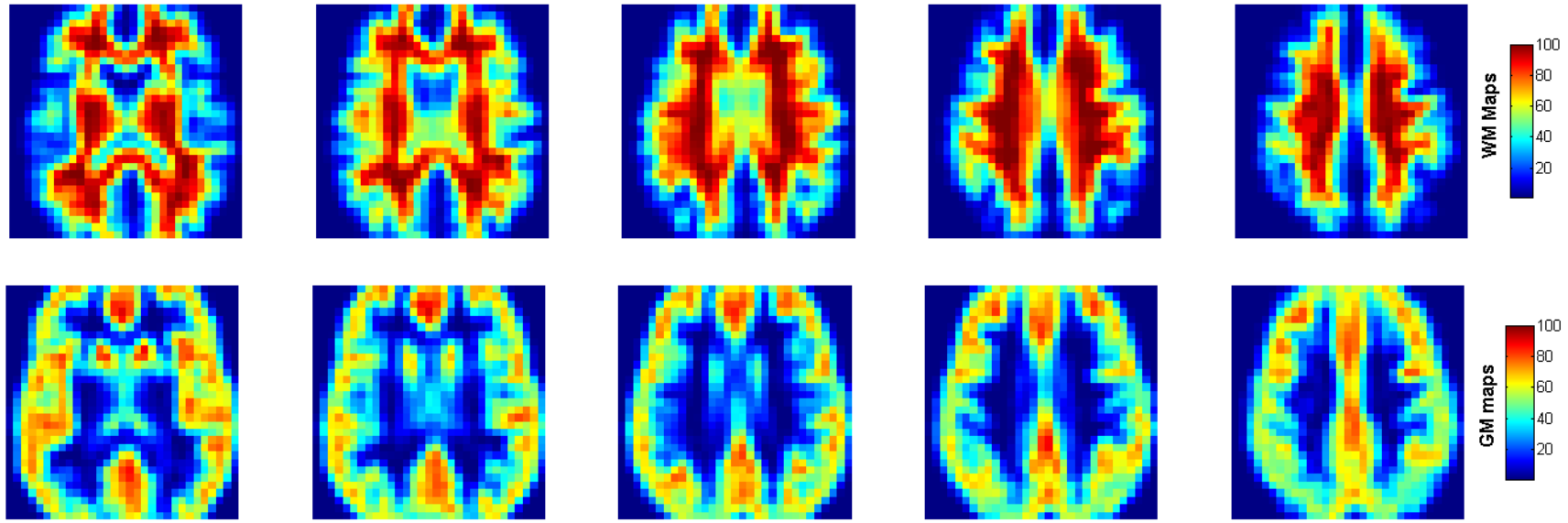

Figure 6.9 Tissue segmentation maps showing the white (top row) and grey matter (bottom row) fractions for each voxel for the temperature maps shown in Figure 6.8.

Volunteers	Temperature (^{0}C)		NAA linewidth (Hz)		Voxels rejected (%)
	Mean	SD	Mean	SD	
1	40.96	1.08	8.79	1.34	44
2	40.49	0.90	8.69	1.37	54
3	39.81	0.93	9.91	0.94	49
4	38.06	0.55	9.65	1.08	45
5	37.39	0.46	8.57	1.26	43

Table 6.1 MRS brain temperature estimates for 5 healthy volunteers obtained using EPSI. The temperature estimates were averaged from five central slices as shown in Figure 6.8, also reported is the average linewidth of the NAA peak and percentage of the voxels excluded from the analysis based on quality assurance criteria (voxel CSF content >10% or NAA linewidth >12 Hz).

It is seen that estimated temperature increases linearly with white matter fraction for these five volunteers. Thus a second analysis was performed in which primarily white matter voxels (i.e. voxels with white matter fraction greater than 80%) were retained. On average, per subject, 18.5% (SD 2.8%) of the acquired voxels were included in this analysis. The average temperature at 5 different slices from five volunteers for this analysis is shown in Table 6.2 and the boxplots of the normalised temperature estimates from this analysis are shown in Figure 6.12. These results indicate a brain temperature gradient of ~0.5^{0}C between the slice number 1 (i.e. axial slice at the central level of Basal Ganglia) and slice number 5 (at the level of centrum semiovale).

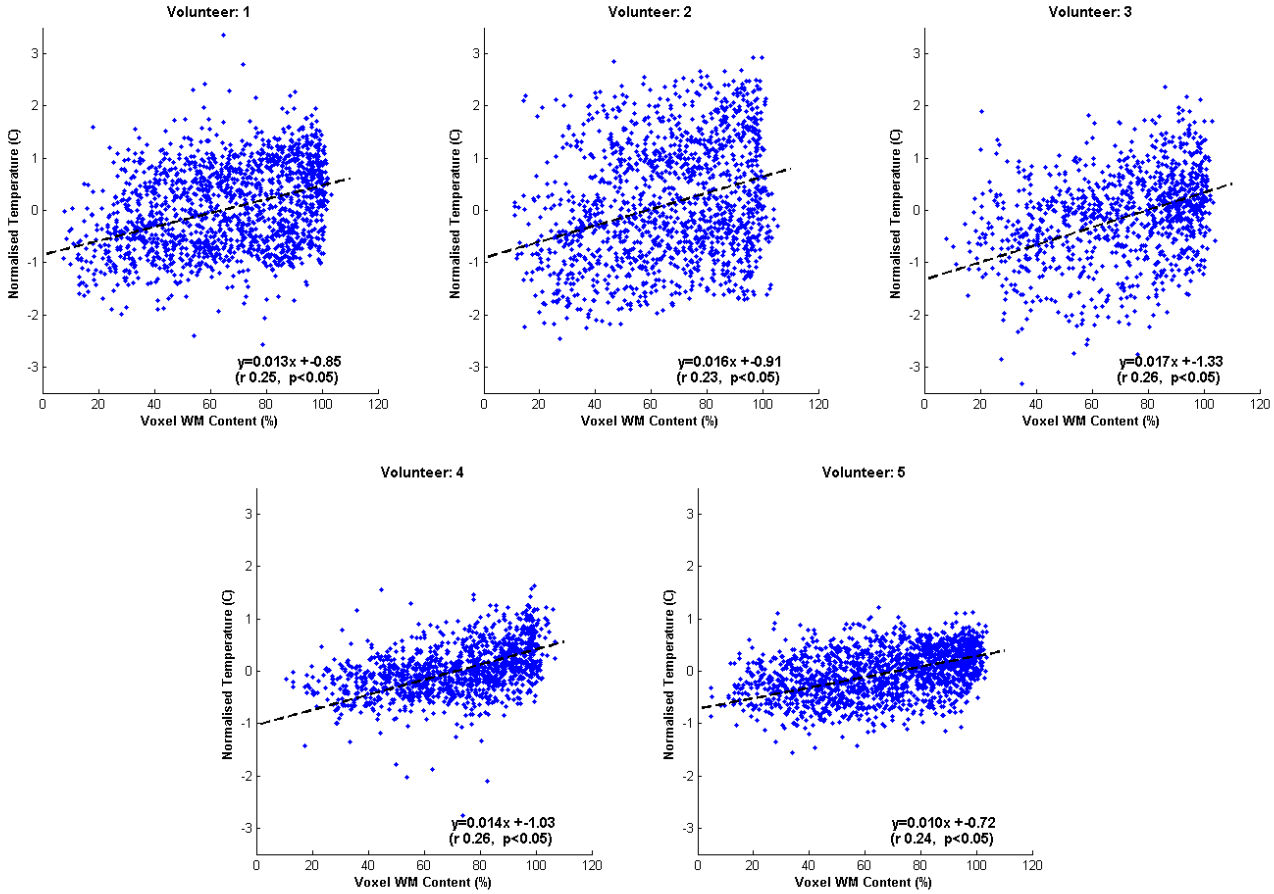

Figure 6.10 Normalized temperature estimates plotted against the white matter content for the 5 healthy volunteers. Temperature estimates were normalized by subtracting the median temperature for each volunteer.

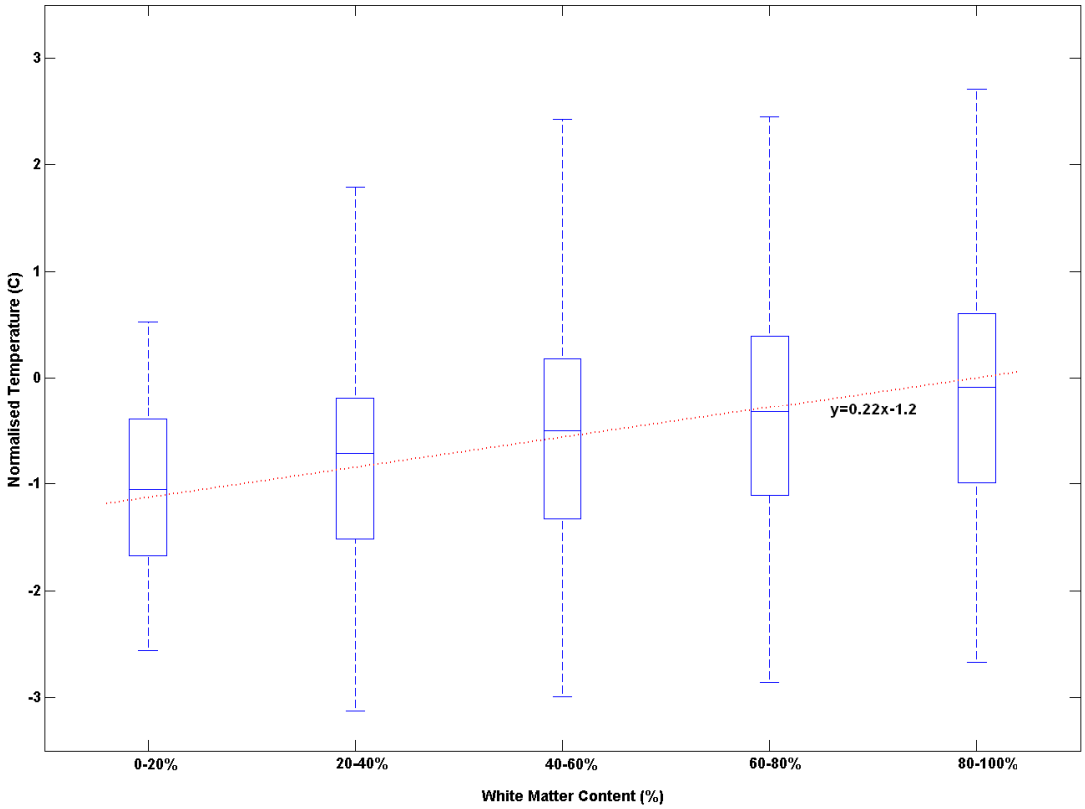

Figure 6.11 Box plots for normalized temperature estimates plotted as function of the white matter content for the 5 volunteers, the least square fit (R=0.23, P<0.0001) to the mean normalised temperature at the various white matter levels is also shown (see also Table 6.2)

White matter content	Normalised Temperature (^{0}C)	
	Mean	SD
0-20%	-1.05	0.87
20-40%	-0.71	0.95
40-60%	-0.50	1.02
60-80%	-0.32	1.02
80-100%	-0.09	1.02

Table 6.2 Normalized temperature estimates (mean, SD) at different proportions of white matter obtained from 5 healthy volunteers using EPSI.

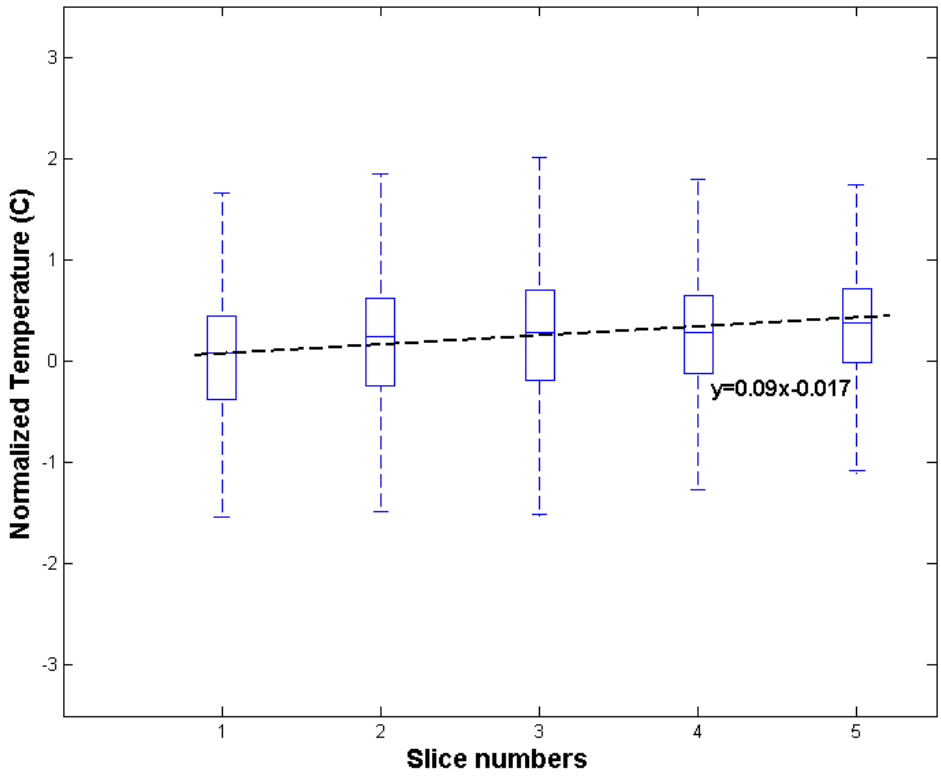

Figure 6.12 Box plots for normalized temperature estimates averaged from 5 volunteers at various slices by retaining white matter voxels (i.e. MRS voxel white matter fraction >80%). The least square fit (R=0.16, P<0.0001) is also shown (also see Table 6.3).

Slice Number	Temperature (C^0)		White matter content (%)	
	Mean	SD	Mean	SD
1	39.70	0.83	90.8	6.2
2	39.88	0.86	90.8	5.8
3	40.00	0.78	90.7	6.0
4	40.09	0.67	92.0	6.4
5	40.22	0.59	91.7	6.2

Table 6.3 Brain temperature estimates at central slices levels (starting at basal ganglia ending at centrum semiovale). The temperature estimates report the mean and SD of voxels containing 80% or more white matter for 5 healthy volunteers at each slice level. The average white matter content is also reported.

6.4.4 Discussion

In this study EPSI data acquired from five healthy volunteers was employed to assess the feasibility of EPSI for brain temperature mapping. The average MRS temperature estimates from 5 central slice for three volunteers (volunteers 1, 2 and 3) was ~40^{0}C and large spread of temperature variation was observed for these volunteers as seen in Figure 6.10 and Table 6.1. For the other two volunteers (volunteers 4 and 5) MRS temperature estimates were realistic (~38^{0}C) and the spread of the temperature was lower as seen in Figure 6.10. As previously discussed, SD in the temperature estimates obtained using MRS increases with increase in NAA linewidth, however NAA linewidths were similar for these five volunteers and as a result similar proportions of the voxels were rejected from the analysis for these volunteers. Thus it was not possible to establish the cause for this large variation in average temperature estimates between subjects. For this study the EPSI datasets were retrospectively selected and were not tightly controlled for a number of factors (medication, daily temperature variation etc) that may influence temperature. Thus the possibility of genuine temperature variations cannot be ruled out. The calibration constants employed to obtain temperature estimates using MRS were also suspected. Thus for the rest of the analysis temperature estimates were normalised by subtraction the median brain temperature of the central five slices on a subject by subject basis.

Analysis of the MRS temperature estimates as a function of the tissue composition indicate a ~1^{0}C apparent temperature difference between grey matter (GM) and white matter (WM) (T_{WM}>T_{GM}) which is equivalent to a frequency difference ($\Delta_{water\text{-}naa}$) of ~ 0.01 ppm between 100% GM and 100% WM. This frequency difference is slightly lower than that (0.015ppm) reported by Chadzynski et al. (66). A possible explanation for this difference is that, in contrast to Chandzynski et al. (66) segmentation maps were employed in this study to reject voxels containing more than 10% CSF in order to limit the analysis between GM and WM voxels. However the similarity of the results reported in this study to those reported by Chadzynski et al. (66) confirms that the frequency difference ($\Delta_{water\text{-}naa}$) is sensitive to tissue composition and it is

necessary to correct for this effect inorder to obtain accurate brain temperature estimates using MRS.

The mean temperatures as reported in Table 6.2 can potentially serve as correction factors to account for the tissue specific frequency differences. However one of the confounders in this study is the true physical brain temperature variations. It can be argued as brain temperature is highly regulated under normal conditions, it is unrealistic to expect large brain temperature brain gradients (of ~1^0C) as discussed by Chadzynski et al. (66). Thus Chadzynski et al. (66), suggest the susceptibility differences due to different tissue architecture and chemical exchange of proton between water and proteins to be the cause of this tissue specific frequency difference between water and NAA. However, the analyses on primarily white matter voxels in this and the previous chapter indicate the possibility smaller brain temperature gradients of ~0.3-0.5^{0}C cannot be completely ruled out. Another potential limitation of this study and that reported by Chadzynski et al. (66) is the low number of subjects. Thus careful validation using a large number of subjects is necessary in order to obtain accurate correction factors to account for tissue specific frequency differences in order to obtain accurate temperature estimates (for healthy volunteers) using internal reference MRS thermometry.

MRSI (including EPSI) data reported in this study was so far acquired using phantoms or healthy volunteers. It was seen that a number of factors such as water suppression, ionic strength of the sample and tissue specific frequency differences affect measurement of regional brain temperature using MRS. Thus further validation is necessary to obtain accurate brain temperature estimates from healthy volunteers using MRS. It can be argued that the ionic and macromolecular content of the sample (brain tissues) which is considered to be primary sources of errors in MRS temperature estimation may vary in different brain pathologies. These changes may lead to apparent (and not real) temperature differences in MRS temperatures estimates which may be different to that reported in this PhD study. Thus the benefits of employing MRS brain temperature mapping in the study of brain thermoregulation in patient populations is currently not clear.

6.5 Summary

In this chapter the feasibility of relatively high resolution echo planar spectroscopic imaging with automated data processing was evaluated. Using EPSI data, the frequency of the water peak was measured from interleaved non water suppression scans and water suppressed EPSI data was used to measure the frequency of the internal reference (NAA), to obtain temperature maps; thus the error due to water suppression was completely avoided. Poor shimming over a larger volume in EPSI acquisitions leads to increased NAA linewidths for both phantom and in-vivo studies than previously obtained; however the SD of temperature estimates were similar. Increased spatial resolution combined with segmentation data allows us to verify the influence of tissue specific frequency difference between NAA and water, the results presented in this chapter provide a promising start to obtain accurate correction factors to account for these differences in order to obtain absolute brain temperature estimates in-vivo using internal reference MRS. Thus it is valuable to employ EPSI in the study of brain temperature regulation. While the focus of this study was to identify regional brain temperature gradients in healthy volunteers using EPSI, it should be noted that this method can be

directly employed to measure temperature changes (of 1^0C or higher) and thus this method is of particular importance in brain cooling studies.

7 Conclusion and future work

7.1 Introduction

Temperature mapping using internal reference MRS is challenging due to the low sensitivity of the proton frequency shift to temperature changes. In contrast to single voxel MRS, MRSI is technically demanding. As a result it has been argued that precision of the MRSI temperature estimates is poor compared to temperature estimates obtained using single voxel MRS (46). The main aim of this PhD study was to investigate and develop a reliable method to obtain brain temperature maps in order to identify regional brain temperature variation using MRSI. For this purpose a number of in-vitro (phantom based) and healthy volunteer studies were performed, as presented in previous chapters of this thesis. In this chapter a summary of the major findings of this PhD study are presented and recommendations for future work are discussed.

7.2 Conclusions

The first and foremost requirement to obtain accurate temperature maps is to improve the quality of MRSI data. A number of technical issues as discussed in section 2.3, influences MRSI data acquisition and thus MRSI based temperature mapping. In chapter 3 it was seen that systematic error is present in based temperature maps. This error is strongly dependent on CHESS based water suppression (which is dependent on the B_o homogeneity across the field of view). It was shown in chapter 3 that this systematic error can be reduced by weakening the water suppression. It was seen that systematic error varies between different scanners and that the temperature maps obtained from a Siemens 3T scanner, acquired using optimised CHESS based water suppression (i.e. WET method), a semi-LASER MRSI pulse sequence to improve localisation profile and sensitivity to B_1 inhomogeneity, and higher (second) order shimming exhibited the smallest temperature variation.

The in-vitro experiments (in chapter 4) demonstrate that a temperature difference of as low as 0.2^0C could be measured using MRSI. For accurate

temperature estimation using MRS it is necessary to acquire spectra with the highest SNR and lowest linewidth possible. For the in-vivo studies reported in chapter 5, NAA linewidths were higher than 1-2 Hz obtained for the phantom experiments reported in chapters 3 and 4, thus a larger variation (1-1.5^{0}C) in temperature estimates was obtained in-vivo. The NAA linewidths obtained in-vivo primarily depend on effectiveness of the shimming across the scan volume. For the majority of experiments reported in this thesis first order shimming was employed due to hardware limitations and the MRSI data quality was optimized by careful selection of the MRSI volume of interest. However with the increasing usage of the higher field strength scanners (3T and higher), a number of advanced shimming methods have been proposed (29;75;88). Where feasible the use of these advanced methods to improve MRSI data quality is recommended.

The in-vitro experiments presented in chapter 4 suggests that there is a reduction in the reproducibility of MRS temperature estimates as the concentrations of the metabolite internal reference (NAA) reduces below 75% of normal physiological level. Thus it may be necessary to use an alternate metabolite peak (such as choline) as an internal reference for temperature mapping in clinical conditions where NAA amplitude is significantly reduced as previously discussed by Corbett et al. (52). The in-vitro experiments were also used to verify the recent reports by Vescovo et al. (50;51) that the calibration constants used to obtain absolute temperature estimates are dependent on ionic strength of the solution employed for calibration experiments. This may lead to systematic error in absolute temperature estimates in-vivo as the ionic strength of the solutions used to obtain calibration constants may be different to that in-vivo.

The in-vivo results presented in chapters 5 and 6 suggests regional brain temperature variations of ~0.3^{0}C exist across the brain. However one of the major drawback of MRSI temperature mapping (in-vivo) is the tissue specific differences between metabolite and water peaks as reported by Chadyzknsi et al. (66). If unaccounted these differences may introduce errors (of up to ~1^{0}C) in regional MRS temperature estimates. For standard MRSI

acquisitions reported in chapter 5, it was not possible to delineate these tissue specific frequency differences as the MRSI voxel size was large (~1cm^3). Thus use of high resolution echo planar spectroscopic imaging for temperature mapping was investigated in Chapter 6 to verify that tissue specific differences do affect MRS temperature measurement and an attempt was made to obtain correction factors to account for these tissue specific frequency differences.

The SNR of these EPSI acquisitions is comparable to standard MRSI (for details see Ebel et al. (89)) and EPSI allow multi slice brain temperature measurements. Also using EPSI, interleaved water reference scans are acquired in clinically feasible exam time and thus allow us to avoid the systematic error due to water suppression. However one of the limitations of EPSI is an increase in the NAA linewidths due to poor shimming over the larger acquisition volumes. Thus the use of advanced shimming methods as previously discussed, is recommended to overcome this limitation.

7.3 Future work

The majority of the MRSI data reported in this PhD study were acquired using a GE 1.5T scanner. As previously discussed phantom based MRSI temperature maps acquired using a Siemens 3T scanner were more uniform and the higher SNR at 3T may benefit temperature measurement, however a number of the technicalities differ between 1.5T and 3T MRS acquisitions (for details see reference (97)). Thus a detailed validation study comparing 1.5T and 3T MRSI for brain temperature mapping is being performed in collaboration with Dr Michael Thrippleton (PI Professor Ian Marshall). The aims of this study are to assess the relative merits of 1.5T and 3T scanners for temperature measurement and to ascertain the day to day and scan to scan repeatability. The results presented in sections 4.5, 5.4 and 5.5 of this thesis obtained from MRSI data acquired (in collaboration with Dr Michael Thrippleton) as part of this study. The data acquisition for this larger study is completed and the results should be able in the near future.

It has been confirmed in this PhD study that frequency differences between metabolite internal reference and water peaks are different between brain tissue types (grey and white matter). The differences in ionic strength and chemical exchange of protons between water and macromolecules are argued to be the reasons for these tissue specific differences. In this study an attempt was made to determine correction factor to account for these differences (in chapter 6). However, one of the confounding factors was genuine brain temperature variations. Thus further work is needed to obtain accurate calibration constants at varying fractions of the grey and white matter which can be combined with segmentation data to account for these tissue specific differences. It should be that noted even if such calibration constants are available, the ionic and macromolecular content may be altered in various brain pathologies, leading to different apparent (and not real) temperature gradients. Thus MRSI brain temperature mapping may be of limited use in understanding brain thermoregulation in brain pathology.

Although it is challenging to measure absolute temperature using MRS, MRS can be employed to measure temperature changes and may be useful in brain cooling studies. The combination of EPSI with parallel imaging as demonstrated by Posse et al. (98) reduces the acquisition time to as low as 12 seconds (for single slice measurement), thus further development of such acquisition techniques (to overcome issues with spectral quality) may permit functional metabolite imaging and can potentially allow measurement of regional temperature variations during brain activity, as discussed by Kauppinen et al. (54) using single voxel MRS.

REFERENCE LIST

(1) Kiyatkin EA. Brain temperature fluctuations during physiological and pathological conditions. European journal of applied physiology 2007;101(1):3-17.

(2) Karaszewski B, Wardlaw JM, Marshall I, Cvoro V, Wartolowska K, Haga K, et al. Measurement of brain temperature with magnetic resonance spectroscopy in acute ischemic stroke. Ann Neurol 2006 Oct 1;60(4):438-46.

(3) Kiyatkin EA. Brain temperature homeostasis: physiological fluctuations and pathological shifts. Frontiers in bioscience: a journal and virtual library 2010;15:73.

(4) Karaszewski B, Wardlaw JM, Marshall I, Cvoro V, Wartolowska K, Haga K, et al. Early brain temperature elevation and anaerobic metabolism in human acute ischaemic stroke. Brain 2009 Apr 1;132(Pt 4):955-64.

(5) Childs C. Human brain temperature: regulation, measurement and relationship with cerebral trauma: Part 1. British Journal of Neurosurgery 2008;22(4):486-96.

(6) Azzopardi DV, Strohm B, Edwards AD, Dyet L, Halliday HL, Juszczak E, et al. Moderate hypothermia to treat perinatal asphyxial encephalopathy. New England Journal of Medicine 2009;361(14):1349-58.

(7) Rango M, Arighi A, Bonifati C, Bresolin N. Increased brain temperature in Parkinsons disease. Neuroreport 2012;23(3):129.

(8) Shiloh R, Kushnir T, Gilat Y, Gross-Isseroff R, Hermesh H, Munitz H, et al. In vivo occipital-frontal temperature-gradient in schizophrenia patients and its possible association with psychopathology: a magnetic resonance spectroscopy study. Eur Neuropsychopharmacol 2008 Aug 1;18(8):557-64.

(9) Pennes H. Analysis of tissue and arterial blood temperatures in the resting human forearm. Journal of applied physiology 1948;1(2):93.

(10) Sukstanskii AL, Yablonskiy DA. Theoretical model of temperature regulation in the brain during changes in functional activity. Proceedings of the National Academy of Sciences 2006;103(32):12144-9.

(11) Collins CM, Smith MB, Turner R. Model of local temperature changes in brain upon functional activation. Journal of applied physiology 2004;97(6):2051-5.

(12) Nelson DA, Nunneley SA. Brain temperature and limits on transcranial cooling in humans: quantitative modeling results. European journal of applied physiology and occupational physiology 1998;78(4):353-9.

(13) Faridar A, Bershad EM, Emiru T, Iaizzo PA, Suarez JI, Divani AA. Therapeutic hypothermia in stroke and traumatic brain injury. Frontiers in Neurology 2011;2.

(14) Rieke V, Butts Pauly K. MR thermometry. J Magn Reson Imaging 2008 Feb 1;27(2):376-90.

(15) Bulte DP, Kelly M, Germuska M, Xie J, Chappell MA, Okell TW, et al. Quantitative measurement of cerebral physiology using respiratory-calibrated MRI. NeuroImage 2011.

(16) Bloch F. The Principle of Nuclear Induction. Science 1953 Oct 16;118(3068):425-30.

(17) Purcell EM, Torrey HC, Pound RV. Resonance Absorption by Nuclear Magnetic Moments in a Solid. Phys Rev 1946 Jan 1;69(1-2):37-8.

(18) McRobbie DW, Moore EA, Graves MJ, Prince MR. MRI from Picture to Proton. Cambridge University Press; 2007.

(19) De Graaf RA. In Vivo NMR Spectroscopy. John Wiley & Sons, Ltd; 2007.

(20) Bernstein MA, King KE, Zhou XJ, Fong W. Handbook of MRI pulse sequences. Medical Physics 2005;32:1452.

(21) Govindaraju V, Young K, Maudsley AA. Proton NMR chemical shifts and coupling constants for brain metabolites. NMR Biomed 2000 May 1;13(3):129-53.

(22) Gideon P, Henriksen O, Sperling B, Christiansen P, Olsen TS, Jorgensen HS, et al. Early time course of N-acetylaspartate, creatine and phosphocreatine, and compounds containing choline in the brain after acute stroke. A proton magnetic resonance spectroscopy study. Stroke 1992;23(11):1566-72.

(23) Leblanc R, Oliver A, Pokrupa R, Arnold D. Accurate, noninvasive diagnosis of human brain tumors by using proton magnetic resonance spectroscopy. Nature medicine 1996;2(3).

(24) Larsson HBW, Christiansen P, Jensen M, Frederiksen J, Heltberg A, Olesen J, et al. Localized in vivo proton spectroscopy in the brain of patients with multiple sclerosis. Magnetic resonance in medicine 1991;22(1):23-31.

(25) Bottomley PA. Spatial Localization in NMR Spectroscopy in Vivo. Annals of the New York Academy of Sciences 1987;508(1):333-48.

(26) Frahm J, Bruhn H, Gyngell ML, Merboldt KD, Hanicke W, Sauter R. Localized high-resolution proton NMR spectroscopy using stimulated echoes: Initial applications to human brain in vivo. Magnetic resonance in medicine 1989;9(1):79-93.

(27) Moonen C. Proton spectroscopic imaging of human brain. Journal of Magnetic Resonance 1992 Jul;98(3):556-75.

(28) Kreis R. Issues of spectral quality in clinical 1H-magnetic resonance spectroscopy and a gallery of artifacts. NMR Biomed 2004 Oct;17(6):361-81.

(29) Koch KM, Sacolick LI, Nixon TW, McIntyre S, Rothman DL, de Graaf RA. Dynamically shimmed multivoxel 1H magnetic resonance spectroscopy and multislice magnetic resonance spectroscopic imaging of the human brain. Magn Reson Med 2007 Mar 1;57(3):587-91.

(30) Webb P, Spielman D, Macovski A. Inhomogeneity correction for in vivo spectroscopy by high-resolution water referencing. Magn Reson Med 1992 Jan 1;23(1):1-11.

(31) Chadzynski GL, Klose U. Chemical shift imaging without water suppression at 3 T. Magnetic Resonance Imaging 2010 Jun;28(5):669-75.

(32) Zheng G, Price WS. Solvent signal suppression in NMR. Progress in Nuclear Magnetic Resonance Spectroscopy 2010 Apr;56(3):267-88.

(33) Haase A, Frahm J, Hanicke W, Matthaei D. 1H NMR chemical shift selective (CHESS) imaging. Physics in medicine and biology 1985;30:341.

(34) Moonen CTW, Van Zijl P. Highly effective water suppression for in vivo proton NMR spectroscopy (DRYSTEAM). Journal of Magnetic Resonance 1990;88(1):28-41.

(35) Ogg RJ, Kingsley RB, Taylor JS. WET, a T1-and B1-insensitive water-suppression method for in vivo localized 1H NMR spectroscopy. Journal of Magnetic Resonance, 1994;104(1):1-10.

(36) Quesson B, de Zwart JA, Moonen CTW. Magnetic resonance temperature imaging for guidance of thermotherapy. Journal of Magnetic Resonance Imaging 2000;12(4):525-33.

(37) Rieke V, Butts Pauly K. MR thermometry. J Magn Reson Imaging 2008 Feb;27(2):376-90.

(38) Kuroda K. Non-invasive MR thermography using the water proton chemical shift. International journal of hyperthermia 2005;21(6):547-60.

(39) Hindman JC. Proton resonance shift of water in the gas and liquid states. The Journal of Chemical Physics 1966;44:4582-4592.

(40) Corbett RJ, Laptook AR, Tollefsbol G, Kim B. Validation of a noninvasive method to measure brain temperature in vivo using 1H NMR spectroscopy. Journal of neurochemistry 1995 Mar 1;64(3):1224-30.

(41) Cady EB, D'Souza PC, Penrice J, Lorek A. The Estimation of Local Brain Temperature by in Vivo1H Magnetic Resonance Spectroscopy. Magnetic resonance in medicine 1995;33(6):862-7.

(42) Corbett R, Laptook A, Weatherall P. Non invasive measurements of human brain temperature using volume-localized proton magnetic resonance spectroscopy. J Cereb Blood Flow Metabolism 1997 Apr 1;17(4):363-9.

(43) Jayasundar R, Singh VP. In vivo temperature measurements in brain tumors using proton MR spectroscopy. Neurology India 2002 Dec 1;50(4):436-9.

(44) Marshall I, Karaszewski B, Wardlaw JM, Cvoro V, Wartolowska K, Armitage P, et al. Measurement of regional brain temperature using proton spectroscopic imaging: validation and application to acute ischemic stroke. Magnetic Resonance Imaging 2006 Jul;24(6):699-706.

(45) Karaszewski B, Wardlaw JM, Marshall I, Cvoro V, Wartolowska K, Haga K, et al. Early brain temperature elevation and anaerobic metabolism in human acute ischaemic stroke. Brain 2009 Apr;132(Pt 4):955-64.

(46) Childs C, Hiltunen Y, Vidyasagar R, Kauppinen RA. Determination of regional brain temperature using proton magnetic resonance spectroscopy to assess brain-body temperature differences in healthy human subjects. Magn Reson Med 2007 Jan 1;57(1):59-66.

(47) Cady EB, Penrice J, Robertson NJ. Improved reproducibility of MRS regional brain thermometry by 'amplitude-weighted combination'. NMR Biomed 2011 Aug;24(7):865-72.

(48) Zhu M, Bashir A, Ackerman JJ, Yablonskiy DA. Improved calibration technique for in vivo proton MRS thermometry for brain temperature measurement. Magn Reson Med 2008 Sep 1;60(3):536-41.

(49) Covaciu L, Rubertsson S, Ortiz-Nieto F, Ahlstrom H, Weis J. Human brain MR spectroscopy thermometry using metabolite aqueous-solution calibrations. J Magn Reson Imaging 2010 Apr 1;31(4):807-14.

(50) Vescovo E, Levick AP, Childs C, Zhao S, Machin G, Rainey T, et al. High Precision Calibration of MRS Thermometry. Proceeding of International Society of Magnetic Resonance in Medicine Sweden, Stockholm. 2010.

(51) Vescovo E. Brain Temperature measured by 1H Magnetic Resonance Spectroscopy, 2011, PhD Thesis, The University of Manchester.

(52) Corbett RJ, Purdy PD, Laptook AR, Chaney C, Garcia D. Non invasive measurement of brain temperature after stroke. AJNR Am J Neuroradiol 1999 Jan 1;20(10):1851-7.

(53) Katz-Brull R, Alsop DC, Marquis RP, Lenkinski RE. Limits on activation-induced temperature and metabolic changes in the human primary visual cortex. Magnetic resonance in medicine 2006;56(2):348-55.

(54) Kauppinen RA, Vidyasagar R, Childs C, Balanos GM. Assessment of human brain temperature by 1 H MRS during visual stimulation and hypercapnia. NMR Biomed 2008;(September 2007):388-95.

(55) Harris BA, Andrews PJ, Marshall I, Robinson TM, Murray GD. Forced convective head cooling device reduces human cross-sectional brain temperature measured by magnetic resonance: a non-randomized healthy volunteer pilot study. Br J Anaesth 2008 Mar 1;100(3):365-72.

(56) Jiru F. Introduction to post-processing techniques. European Journal of Radiology 2008 Aug;67(2):202-17.

(57) Young K, Soher BJ, Maudsley AA. Automated spectral analysis II: application of wavelet shrinkage for characterization of non-parameterized signals. Magn Reson Med 1998 Dec 1;40(6):816-21.

(58) Soher BJ, Young K, Govindaraju V, Maudsley AA. Automated spectral analysis III: application to in vivo proton MR spectroscopy and spectroscopic imaging. Magn Reson Med 1998 Dec 1;40(6):822-31.

(59) Young K, Govindaraju V, Soher BJ, Maudsley AA. Automated spectral analysis I: formation of a priori information by spectral simulation. Magn Reson Med 1998 Dec;40(6):812-5.

(60) Ordidge RJ, Cresshull ID. The correction of transient Bo field shiefts following the application of pulse gradients by phase correction in the time domain. Journal of Magnetic Resonance 1986;69(1):151-5.

(61) Johnson G, Jung KJ, Wu EX, Hilal SK. Self correction of proton spectroscopic images for gradient eddy current distortions and static field inhomogeneities. Magnetic resonance in medicine 1993;30(2):255-61.

(62) Naressi A, Couturier C, Castang I, De Beer R, Graveron-Demilly D. Java-based graphical user interface for MRUI, a software package for quantitation of in vivo/medical magnetic resonance spectroscopy signals. Computers in biology and medicine 2001;31(4):269-86.

(63) Vanhamme L, van den Boogaart A, Van Huffel S. Improved method for accurate and efficient quantification of MRS data with use of prior knowledge. Journal of Magnetic Resonance 1997;129(1):35-43.

(64) Scheenen TWJ, Klomp DWJ, Wijnen JP, Heerschap A. Short echo time 1H-MRSI of the human brain at 3T with minimal chemical shift displacement errors using adiabatic refocusing pulses. Magnetic resonance in medicine 2008;59(1):1-6.

(65) Ogg RJ, Langston JW, Haacke EM, Steen RG, Taylor JS. The correlation between phase shifts in gradient-echo MR images and regional brain iron concentration. Magnetic Resonance Imaging 1999 Oct;17(8):1141-8.

(66) Chadzynski GL, Bender B, Groeger A, Erb M, Klose U. Tissue specific resonance frequencies of water and metabolites within the human brain. Journal of magnetic resonance, 2011 Jul;1-9.

(67) Nixon TW, McIntyre S, Rothman DL, de Graaf RA. Compensation of gradient-induced magnetic field perturbations. Journal of Magnetic Resonance 2008;192(2):209-17.

(68) Clayton DB, Elliott MA, Leigh JS, Lenkinski RE. 1H spectroscopy without solvent suppression: characterization of signal modulations at short echo times. Journal of Magnetic Resonance 2001;153(2):203-9.

(69) Dong Z, Dreher W, Leibfritz D. Experimental method to eliminate frequency modulation sidebands in localized in vivo 1H MR spectra acquired without water suppression. Magn Reson Med 2004 Mar;51(3):602-6.

(70) Serrai HN, Clayton DB, Senhadji L, Zuo C, Lenkinski RE. Localized proton spectroscopy without water suppression: removal of gradient induced frequency modulations by modulus signal selection. Journal of magnetic resonance, 2002 Jan;154(1):53-9.

(71) Ebel A, Maudsley AA. Detection and correction of frequency instabilities for volumetric 1H echo-planar spectroscopic imaging. Magn Reson Med 2005 Feb 1;53(2):465-9.

(72) Collins CM, Liu W, Wang J, Gruetter R, Vaughan JT, Ugurbil K, et al. Temperature and SAR calculations for a human head within volume and surface coils at 64 and 300 MHz. Journal of Magnetic Resonance Imaging 2004;19(5):650-6.

(73) Corbett RJT, Laptook AR, Tollefsbol G, Kim B. Validation of a noninvasive method to measure brain temperature in vivo using 1H NMR spectroscopy. Journal of neurochemistry 1995;64(3):1224-30.

(74) Clare S, Evans J, Jezzard P. Requirements for room temperature shimming of the human brain. Magnetic resonance in medicine 2006;55(1):210-4.

(75) Koch KM, Rothman DL, de Graaf RA. Optimization of static magnetic field homogeneity in the human and animal brain in vivo. Progress in Nuclear Magnetic Resonance Spectroscopy 2009;54(2):69.

(76) Zidi ZS. Solvation of sodium-chloride ion pair in water cluster at atmospheric conditions: Grand canonical ensemble Monte Carlo simulation. The Journal of Chemical Physics 2005;123:064309.

(77) Gu B, Zhang FS, Wang ZP, Zhou HY. The solvation of NaCl in model water with different hydrogen bond strength. The Journal of Chemical Physics 2008;129:184505.

(78) Schuff N, Ezekiel F, Gamst AC, Amend DL, Capizzano AA, Maudsley AA, et al. Region and tissue differences of metabolites in normally aged brain using multislice 1H magnetic resonance spectroscopic imaging. Magn Reson Med 2001 May 1;45(5):899-907.

(79) Marshall I, Wardlaw J, Cannon J, Slattery J, Sellar RJ. Reproducibility of metabolite peak areas in 1H MRS of brain. Magnetic Resonance Imaging 1996;14(3):281-92.

(80) Haga KK, Khor YP, Farrall A, Wardlaw JM. A systematic review of brain metabolite changes, measured with 1H magnetic resonance spectroscopy, in healthy aging. Neurobiology of Aging 2009 Mar;30(3):353-63.

(81) Kantarci K, Weigand SD, Petersen RC, Boeve BF, Knopman DS, Gunter J, et al. Longitudinal 1H MRS changes in mild cognitive impairment and Alzheimer's disease. Neurobiology of Aging 2007;28(9):1330-9.

(82) Ferguson KJ, MacLullich AMJ, Marshall I, Deary IJ, Starr JM, Seckl JR, et al. Magnetic resonance spectroscopy and cognitive function in healthy elderly men. Brain 2002;125(12):2743-9.

(83) Deary I, Gow A, Taylor M, Corley J, Brett C, Wilson V, et al. The Lothian Birth Cohort 1936: a study to examine influences on cognitive ageing from age 11 to age 70 and beyond. BMC geriatrics 2007;7(1):28.

(84) Wardlaw JM, Bastin ME, Valdes Hernandez MC, Maniega SM, Royle NA, Morris Z, et al. Brain aging, cognition in youth and old age and vascular disease in the Lothian Birth Cohort 1936: rationale, design and methodology of the imaging protocol*. International Journal of Stroke 2011;6(6):547-59.

(85) Schmidt R, Ropele S, Enzinger C, Petrovic K, Smith S, Schmidt H, et al. White matter lesion progression, brain atrophy, and cognitive decline: The Austrian stroke prevention study. Ann Neurol 2005;58(4):610-6.

(86) van Straaten ECW, Fazekas F, Rostrup E, Scheltens P, Schmidt R, Pantoni L, et al. Impact of white matter hyperintensities scoring method on correlations with clinical data. Stroke 2006;37(3):836-40.

(87) Penke L, Valdes Hernandez MC, Maniega SMo, Gow AJ, Murray C, Starr JM, et al. Brain iron deposits are associated with general cognitive ability and cognitive aging. Neurobiology of Aging 2012 Mar;33(3):510-7.

(88) Juchem C, Muller-Bierl B, Schick F, Logothetis NK, Pfeuffer J. Combined passive and active shimming for in vivo MR spectroscopy at high magnetic fields. Journal of magnetic resonance 2006 Dec;183(2):278-89.

(89) Ebel A, Maudsley AA. Improved spectral quality for 3D MR spectroscopic imaging using a high spatial resolution acquisition strategy. Magnetic Resonance Imaging 2003 Feb 1;21(2):113-20.

(90) Maudsley AA, Domenig C, Govind V, Darkazanli A, Studholme C, Arheart K, et al. Mapping of brain metabolite distributions by volumetric proton MR spectroscopic imaging (MRSI). Magnetic resonance in medicine 2009;61(3):548.

(91) Ebel A, Soher BJ, Maudsley AA. Assessment of 3D proton MR echo-planar spectroscopic imaging using automated spectral analysis. Magn Reson Med 2001 Dec 1;46(6):1072-8.

(92) Mansfield P. Multi-planar image formation using NMR spin echoes. Journal of Physics C: Solid State Physics 1977;10:L55.

(93) Poustchi-Amin M, Mirowitz SA, Brown JJ, McKinstry RC, Li T. Principles and Applications of Echo-planar Imaging: A Review for the General Radiologist1. Radiographics 2001;21(3):767-79.

(94) Mansfield P. Spatial mapping of the chemical shift in NMR. Magnetic resonance in medicine 1984;1(3):370-86.

(95) Posse S, Tedeschi G, Risinger R, Ogg R, Bihan DL. High Speed 1H Spectroscopic Imaging in Human Brain by Echo Planar Spatial-Spectral Encoding. Magnetic resonance in medicine 1995;33(1):34-40.

(96) Maudsley AA, Darkazanli A, Alger JR, Hall LO, Schuff N, Studholme C, et al. Comprehensive processing, display and analysis for in vivo MR spectroscopic imaging. NMR Biomed 2006 Jun 1;19(4):492-503.

(97) Di Costanzo A, Trojsi F, Tosetti M, Giannatempo GM, Nemore F, Piccirillo M, et al. High-field proton MRS of human brain. European Journal of Radiology 2003 Nov;48(2):146-53.

(98) Posse S, Otazo R, Tsai SY, Yoshimoto AE, Lin FH. Single-shot magnetic resonance spectroscopic imaging with partial parallel imaging. Magnetic resonance in medicine 2009;61(3):541-7.

APPENDIX: LIST OF ABSTRACTS

Parikh J, Thrippleton M and Marshall I, Reduction of systematic error in MRSI based brain temperature mapping, In-preparation, for Magnetic Resonance in Medicine.

Parikh J and Marshall I, A simple and effective method for QA of MRS data Proceeding of SINAPSE and IPEM Multicentre MRI day, (Edinburgh, 2010).

Parikh J and Marshall I, MR spectroscopic imaging and brain temperature mapping, Proceedings of SINAPSE Annual Scientific Meeting, (Edinburgh, 2010) and Proceedings of British Chapter of International Society of Magnetic Resonance in Medicine, (Nottingham, 2010).

Parikh J, Marshall I, Murray C, Allerhand M, Harris B, Thrippleton M, Wardlaw J, Deary I, Andrews J and Starr J. Regional metabolites and brain temperature measured using ^{1}H MRSI: A pilot study on healthy elderly volunteers from Lothian Birth Cohort 1936 (LBC1936). Proceedings of ESMRMB (Leipzig, 2011), P285.

Parikh J, Michael T and Marshall I, Systematic error in MRSI based brain temperature mapping, Proceedings of British Chapter of International Society of Magnetic Resonance in Medicine, (Manchester, 2011), P66.

Parikh J, Thrippleton M and Marshall I, Reduction of systematic error in MRSI based brain temperature mapping, Proceedings of 20th International Society of Magnetic Resonance in Medicine, (Melbourne, 2012).

Thrippleton M, **Parikh J,** Hammer S**,** Harris B, Andrews PJ, Wardlaw JM and Marshall I, A Temperature controlled phantom for MR spectroscopic imaging. Proceedings of British Chapter of International Society of Magnetic Resonance in Medicine, (Cambridge, 2012).

Wardlaw JM, Brindle W, Casado AM, Shuler K, Henderson M, Thomas B, Macfarlane J, Muñoz Maniega S, Lymer K, Morris Z, Pernet C, Nailon W, Ahearn T, Mumuni AN, Mugruza C, McLean J, Chakirova G, Tao YT, Simpson J, Stanfield AC, Johnston H, **Parikh J**, Royle NA, De Wilde J, Bastin ME, Weir N, Farrall A, Valdes Hernandez MC; The SINAPSE Collaborative Group. A systematic review of the utility of 1.5 versus 3 Tesla magnetic resonance brain imaging in clinical practice and research, European Radiology 2012.